

AN ABSTRACT OF THE DISSERTATION OF

Jie Zhang for the degree of Doctor of Philosophy in Chemistry presented on June 2, 2010.

Title: Zero Kinetic Energy Photoelectron Spectroscopy of Polycyclic Aromatic Hydrocarbons.

Abstract approved: \_\_\_\_\_

Wei Kong

In this dissertation, I present electronic spectra of a few polycyclic aromatic hydrocarbons (PAHs): tetracene, pentacene, pyrene, benzo[g,h,i]perylene and benzo[a]pyrene using resonantly enhanced multiphoton ionization (REMPI) and zero kinetic energy (ZEKE) photoelectron spectroscopy. The work of tetracene and pentacene also combine a laser desorption source with a ZEKE spectrometer, demonstrating our capability for studies of thermally labile species. The experiment involves two tunable ultraviolet laser sources, one to excite the vaporized PAH molecules to the first excited electronic state with different levels of vibrational energy, and the other to further reach the Rydberg states just below the ionization threshold of a vibrational level of the cation. Ultimate ionization and detection of ZEKE electrons are achieved using a delayed pulsed electric field. With this approach, the adiabatic ionization potential of each molecule is obtained. Several skeletal vibrational modes of the first electronically excited state of the neutral

species and those of the cation are assigned, with the aid of *ab initio* and density functional theory calculations. In addition to giving a fundamental understanding of the photophysics of this type of compounds, another major motivation of this study is to offer a database for astrophysical modeling, in terms of both direct line identification and modeling of the chemical and radiation balance of the interstellar medium. The distinctive set of infrared (IR) emission bands at 3.3, 6.2, 7.7, 8.6, and 11.3  $\mu\text{m}$  are ubiquitously seen in a wide variety of astrophysical environments. They are generally attributed to polycyclic aromatic hydrocarbons. However, not a single PAH species has yet been identified. Zero kinetic energy photoelectron spectroscopy presents information on the vibrational modes of a cation in the far-infrared (FIR) region, and the FIR modes are sensitive to the skeletal characteristics of a molecule and hence are critical for chemical identification. Although ZEKE is governed by the Franck-Condon principle, some IR active bands can be probed through vibronic coupling between the two lowest intermediate electronic states in highly symmetric PAHs. In low symmetry PAHs such as benzo[a]pyrene, the Franck-Condon allowed total symmetric modes are already IR active. Both IR active and forbidden modes are necessary for astrophysical modeling. With the frequencies from ZEKE, calibration of theoretical calculations with experiments becomes possible, particularly for the FIR region of cations where other types of experiments suffer from lack of light sources, insensitive detectors, and low particle concentrations.

©Copyright by Jie Zhang

June 2, 2010

All Rights Reserved

Zero Kinetic Energy Photoelectron Spectroscopy of Polycyclic Aromatic  
Hydrocarbons

by  
Jie Zhang

A DISSERTATION

submitted to

Oregon State University

in partial fulfillment of  
the requirements for the  
degree of

Doctor of Philosophy

Presented June 2, 2010  
Commencement June 2011

Doctor of Philosophy dissertation of Jie Zhang presented on June 2, 2010.

APPROVED:

---

Major Professor, representing Chemistry

---

Chair of the Department of Chemistry

---

Dean of the Graduate School

I understand that my dissertation will become part of the permanent collection of Oregon State University Libraries. My signature below authorizes release of my dissertation to any reader upon request.

---

Jie Zhang, Author

## ACKNOWLEDGEMENTS

I am heartily thankful to my advisor, Dr. Wei Kong, whose encouragement, guidance and support through all these years enabled me to develop an understanding of the subject.

I would also like to thank the rest of my thesis committee: Dr. Chang, Dr. Evans, Dr. Keszler, and Dr. Nibler for their insightful comments, and questions.

I would like to show my gratitude to Ted Hinke, for his support of designing and building the experimental instrument.

I am indebted to my fellow labmates and former group members: Yonggang He, Linsen Pei who taught me the details of running experiment and Fangyuan Han, Colin Harthcock the for the stimulating discussions and for all the funs we had together.

I would like to thank my parents Zhenhua Zhang and Yuying Shi for supporting me spiritually throughout my life.

I owe my loving thanks to my husband Changqing Pan. Without his support and understanding it would have been impossible for me to finish this work.

## CONTRIBUTION OF AUTHORS

Dr. Linsen Pei assisted with data collection in Chapter 3 and 4. Fangyuan Han assisted with data collection in Chapter 4, 5, 6 and 7. Dr. Angen Li assisted interpretation of the data in Chapter 4.

## TABLE OF CONTENTS

	<u>Page</u>
1. Introduction.....	1
1.1. Zero kinetic energy photoelectron spectroscopy.....	1
1.2. Background of polycyclic aromatic hydrocarbons.....	6
1.3. Summery.....	11
1.4. Reference.....	12
2. Experimental setup.....	14
2.1. General description.....	14
2.2. Sample source.....	20
2.2.1. Supersonic molecular beam.....	20
2.2.2. Laser desorption source.....	20
2.2.3. Heating source.....	22
2.3. PFI – ZEKE spectrometer.....	23
2.3.1. Spectrometer construction.....	23
2.3.2. TOF-MS mode.....	25
2.3.3. PFI-ZEKE mode.....	28
2.4. System timing.....	29
3. Zero kinetic energy photoelectron spectroscopy of tetracene using laser desorption for vaporization.....	35
3.1. Abstract.....	36
3.2. Introduction.....	37
3.3. Experimental setup.....	39
3.4. Results.....	43
3.4.1. Two-color 1+1' REMPI spectroscopy.....	43
3.4.2. ZEKE spectroscopy.....	47

## TABLE OF CONTENTS (Continued)

	<u>Page</u>
3.5. Discussion.....	51
3.6. Conclusion.....	58
3.7. Acknowledgements.....	59
3.8. Reference.....	60
4. Far-Infrared spectroscopy of cationic polycyclic aromatic hydrocarbons: zero kinetic energy photoelectron spectroscopy of pentacene vaporized from laser desorption.....	62
4.1. Abstract.....	63
4.2. Introduction.....	64
4.3. The ZEKE technique.....	67
4.4. Experimental setup.....	69
4.5. Results.....	71
4.5.1. Two-color 1+1' REMPI spectrum.....	71
4.5.2. ZEKE spectra.....	76
4.6. Discussion.....	80
4.6.1. Vibrational modes of the S <sub>1</sub> state.....	80
4.6.2. Vibrational modes of the cation.....	85
4.6.3. Remarks on the comparison between experimental and theoretical vibrational frequencies.....	86
4.6.4. Astrophysical implications.....	87
4.7. Conclusion.....	92
4.8. Acknowledgements.....	93
4.9. Reference.....	94
5. Zero kinetic energy photoelectron spectroscopy of pyrene...	97
5.1. Abstract.....	98

## TABLE OF CONTENTS (Continued)

	<u>Page</u>
5.2. Introduction.....	99
5.3. Experimental setup.....	102
5.4. Results.....	104
5.4.1. Two-color 1+1' REMPI spectrum.....	104
5.4.2. ZEKE spectra.....	107
5.5. Discussion.....	114
5.5.1. The nature of the S <sub>1</sub> state.....	114
5.5.2. Geometry and vibrational modes of the S <sub>1</sub> state....	118
5.5.3. Geometry and vibrational modes of the D <sub>0</sub> state...	121
5.5.4. Comparisons with cata-condensed PAHs.....	124
5.6. Conclusion.....	126
5.7. Acknowledgements.....	128
5.8. References.....	129
6. ZEKE spectroscopy of benzo[g,h,i]perylene.....	132
6.1. Abstract.....	133
6.2. Introduction.....	134
6.3. Experimental setup.....	136
6.4. Result.....	138
6.4.1. Two-color 1+1' REMPI spectrum.....	138
6.4.2. ZEKE spectra.....	143
6.5. Discussion.....	147
6.5.1. Geometry and vibrational modes of the S <sub>1</sub> state...	148
6.5.2. Geometry and vibrational modes of the D <sub>0</sub> state..	149
6.6. Conclusion.....	151
6.7. Acknowledgements.....	152
6.8. References.....	153

## TABLE OF CONTENTS (Continued)

	<u>Page</u>
7. ZEKE spectroscopy of benzo[a]pyrene.....	155
7.1. Abstract.....	156
7.2. Introduction.....	157
7.3. Experimental setup.....	159
7.4. Result.....	162
7.4.1. Two-color 1+1' REMPI spectrum.....	162
7.4.2. ZEKE spectra.....	168
7.5. Discussion.....	175
7.6. Conclusion.....	182
7.7. Acknowledgements.....	183
7.8. References.....	184
8 Conclusion.....	186
8.1 Summery.....	186
8.2 Future work.....	188
8.3 References.....	189

## LIST OF FIGURES

<u>Figure</u>	<u>Page</u>
1.1. Illustrations of PES, TPES and ZEKE. The dashed lines represent tunable light sources .....	3
1.2. Molecular structures of a few PAHs, including both compact peri-condensed molecules and thermodynamically less favored cata-condensed species.....	8
2.1. Experimental layout and signal processing.....	15
2.2. Schematic of the vacuum system.....	17
2.3. Schematic of the differentially pumped molecular beam system..	18
2.4. Details of the laser desorption source.....	21
2.5. ZEKE spectrometer with the laser desorption source.....	24
2.6. Timing diagram of the PFI-ZEKE experiment.....	30
2.7. Timing profiles of the pulsed valve and of the desorbed sample in the molecular beam. (a) Intensity of laser desorbed coronene ions vs. the delay time between the pulsed valve and the excitation laser. (b) Intensity of pyrimidine enclosed in the pulsed valve vs the delay time between pulsed valve and the excitation laser.....	34
3.1. Experimental setup showing details of the laser desorption source.	41
3.2. 1+1' REMPI spectrum of jet-cooled tetracene. The spectrum is shifted by $22\,396\text{ cm}^{-1}$ (the origin of the $S_1 \leftarrow S_0$ transition) to emphasize the frequencies of the different vibrational modes of the $S_1$ state.....	44
3.3. Four observed normal modes in the $S_1$ state of tetracene.....	45
3.4. Two-color ZEKE spectra of tetracene recorded via the following vibrational levels of the $S_1$ state as intermediate states: (a) $0_0^0$ , (b) $15^1$ , (c) $22^2 15^1$ , (d) $15^2$ , (e) $14^1$ , and (f) $13^1$ . The energy in the abscissa is relative to the ionization threshold at $55918\text{ cm}^{-1}$ . The assignment in the figure refers to the vibrational levels of the cation, and the corresponding vibrational level of the intermediate	

## LIST OF FIGURES (Continued)

<u>Figure</u>	<u>Page</u>
state is labeled by a black dot in each panel.....	48
3.5. The HOMO and LUMO of tetracene. The dashed lines mark the nodal planes.....	52
3.6. Charge distributions on rings of three states of tetracene.....	55
4.1. 1+1' REMPI spectrum of pentacene. The spectrum is shifted by 18657 cm <sup>-1</sup> (the origin of the S <sub>1</sub> ←S <sub>0</sub> transition) to emphasize the frequencies of the different vibrational modes of the S <sub>1</sub> state.	72
4.2. Displacement vectors for five normal modes of pentacene. Mode 102 is not observed in the REMPI spectrum of Figure 4.1 but observed in the ZEKE spectrum of Figure 4.3.....	74
4.3. Two-color ZEKE spectra of pentacene recorded via the following vibrational levels of the S <sub>1</sub> state as intermediate states: (a) 0 <sub>0</sub> <sup>0</sup> , (b) 33 <sup>1</sup> , (c) 101 <sup>1</sup> , (d) 18 <sup>1</sup> . The energy in the abscissa is relative to the ionization threshold at 53266 cm <sup>-1</sup> . The assignment in the figure refers to the vibrational levels of the cation.....	78
4.4. (a) HOMO and (b) LUMO of pentacene with the numbering scheme of the carbon atoms. The dashed lines mark the nodal planes based on a simple Hückel calculation.....	83
4.5. The calculated IR spectroscopy of naphthalene, anthracene, tetracene, and pentacene. Also shown are the wavelength coverages of some key astronomical instruments which are relevant for detecting individual PAHs in space	90
5.1. (1+1') REMPI spectrum of jet-cooled Pyrene. The spectrum is shifted by 27211 cm <sup>-1</sup> (the origin of the S <sub>1</sub> ←S <sub>0</sub> transition) to emphasize the frequencies of the different vibrational levels of the S <sub>1</sub> state.....	105
5.2. Two-color ZEKE spectra of pyrene recorded via seven vibrational levels of the S <sub>1</sub> state as intermediate states: (a) 0 <sup>0</sup> , (b) 13 <sup>1</sup> , (c) 65 <sup>1</sup> , (d) 64 <sup>1</sup> , (e) 12 <sup>1</sup> , (f) 41 <sup>1</sup> 40 <sup>1</sup> , (g) 63 <sup>1</sup> . The energy in the x-axis is relative to the ionization threshold at 59888 cm <sup>-1</sup> . The assignment	

## LIST OF FIGURES (Continued)

<u>Figure</u>	<u>Page</u>
<p>in the figure refers to the vibrational levels of the cation, and the corresponding vibrational level of the intermediate state is labeled by a black dot in each panel.....</p>	109
5.3. Displacement vectors for a few normal modes of pyrene.....	113
5.4. The HOMO-1, HOMO, LUMO and LUMO+1 of pyrene. The dashed lines mark the nodal planes based on a simple Hückel calculation.....	116
5.5. Frequencies of the longitudinal stretching mode vs. the inverse of the length of a PAH molecule including benzene, naphthalene, anthracene, tetracene, pentacene and pyrene. The error bars are reported experimental uncertainties.....	125
6.1. Structure of Benzo [g,h,i] perylene and the axis orientation.....	137
6.2. (1+1') REMPI spectrum of jet-cooled Benzo [g,h,i] perylene. The spectrum is shifted by 25207 cm <sup>-1</sup> (the origin of the S <sub>1</sub> ←S <sub>0</sub> transition) to emphasize the frequencies of the different vibrational levels of the S <sub>1</sub> state.....	140
6.3. Two-color ZEKE spectra of BghiP recorded via seven vibrational levels of the S <sub>1</sub> state as intermediate states: (a) 0 <sup>0</sup> , (b) 79 <sup>1</sup> , (c) 78 <sup>1</sup> , (d) 75 <sup>1</sup> , (e) 73 <sup>1</sup> , (f) 78 <sup>1</sup> 31 <sup>1</sup> . The energy in the x-axis is relative to the ionization threshold at 57623 cm <sup>-1</sup> . The assignment in the figure refers to the vibrational levels of the cation, and the corresponding vibrational level of the intermediate state is labeled by a black dot in each panel.	145
7.1. Structure of Benzo [a] pyrene and the axis orientation.....	160
7.2. REMPI spectrum of benzo [a] pyrene.(a) experiment result. (b) Franck-Condon simulation.....	163
7.3. Two-color ZEKE spectra of BaP recorded via the following vibrational levels of the S <sub>1</sub> state as intermediate states: (a) 0 <sup>0</sup> , (b) 59 <sup>1</sup> , (c) 58 <sup>1</sup> , (d) 56 <sup>1</sup> , (e) 55 <sup>1</sup> , (f) 54 <sup>1</sup> . The energy in the figure is relative to the ionization threshold at 57271 cm <sup>-1</sup> . The assignment in the figure refers to the vibrational levels of the cation, and the corresponding vibrational level of the intermediate state is labeled by a black dot in each panel.....	169

LIST OF FIGURES (Continued)

<u>Figure</u>	<u>Page</u>
7.4. Two-color ZEKE spectra of BaP recorded via the following vibrational levels of the S <sub>1</sub> state as intermediate states: : (a) 53 <sup>1</sup> , (b) 52 <sup>1</sup> , (c) 51 <sup>1</sup> , (d) 50 <sup>1</sup> , (e) 49 <sup>1</sup> , (f) 48 <sup>1</sup> . The energy in the figure is relative to the ionization threshold at 57271 cm <sup>-1</sup> . The assignment in the figure refers to the vibrational levels of the cation, and the corresponding vibrational level of the intermediate state is labeled by a black dot in each panel.....	170
7.5. Comparison between experimental ZEKE spectra with Franck-Condon simulation. (a) experimental ZEKE. (b) Franck-Condon simulation.....	178

## LIST OF TABLES

<u>Table</u>	<u>Page</u>
2.1. Summary of laser dyes involved in the experiment.....	19
2.2. Voltage settings of TOF-MS and ZEKE spectrometer.....	27
2.3. Typical settings of the Delay generators.....	32
3.1. Observed and calculated vibrational frequencies of the $S_1$ state of tetracene.....	46
3.2. Observed and calculated vibrational frequencies and assignments in the ZEKE spectra of tetracene.....	49
3.3. Molecular geometry parameters of tetracene in the $S_0$ , $S_1$ and $D_0$ state.....	53
4.1 Observed and calculated vibrational frequencies of the $S_1$ state of pentacene.....	73
4.2. Observed and calculated vibrational frequencies of pentacene cation.....	79
4.3. Molecular geometry parameters of pentacene in the $S_0$ , $S_1$ , and $D_0$ states.....	82
4.4. IR active FIR modes of cationic pentacene from DFT calculation.....	89
5.1. Observed and calculated vibrational frequencies of the $S_1$ state of pyrene.....	106
5.2. Observed and calculated vibrational frequencies of pyrene cation.....	110
5.3. Molecular geometry parameters of pyrene in the $S_0$ , $S_1$ , and $D_0$ states.....	119
6.1. Observed and calculated vibrational frequencies of the $S_1$ state of benzo [g,h,i] perylene.....	141
6.2. Observed and calculated vibrational frequencies of	

LIST OF TABLES (Continued)

<u>Table</u>	<u>Page</u>
benzo [g,h,i] perylene cation.....	146
7.1. Observed and calculated vibrational frequencies of the S <sub>1</sub> state of benzo [a] pyrene.....	164
7.2. Observed and calculated vibrational frequencies of BaP cation.....	171
7.3. Molecular geometry parameters of BaP in the S <sub>0</sub> , S <sub>1</sub> , and D <sub>0</sub> states.....	181

# **Zero Kinetic Energy Photoelectron Spectroscopy of Polycyclic Aromatic Hydrocarbons**

## **Chapter 1 Introduction**

### **1.1 Zero kinetic energy photoelectron spectroscopy**

Zero kinetic energy photoelectron (ZEKE) spectroscopy, a special type of photoelectron spectroscopy (PES), was initially invented by Müller-Dethlefs and Schlag in 1984.<sup>1</sup> In traditional PES,<sup>2</sup> a light source with a fixed wavelength is used for photoionization of the interested species, and the resultant electrons with different kinetic energies are dispersed, either in space or time, for detection. The information of cation eigenstates comes from the kinetic energies of the electrons based on energy conservation. Although photoelectron spectroscopy has been used in both the condensed phase and the gas phase extensively, its energy resolution, on the order of 10 meV ( $80\text{ cm}^{-1}$ ), is limited because of the efficiency of the energy dispersion device.

Threshold photoelectron spectroscopy (TPES)<sup>3</sup> is a higher resolution variation of PES. Instead of analyzing the kinetic energy of photoelectrons from a light source with a fixed wavelength, TPES collects threshold photoelectrons from a tunable light source. These electrons have nearly zero kinetic energies and can be collected with a high efficiency. By scanning the energy of the ionization laser,

similar information of the cation as that of PES can be obtained. The resolution of TPES is limited by the bandwidth of the radiation and more importantly, by the discrimination capability of the spectrometer against energetic electrons. Typical resolutions of TPES are on the order of 5-10 meV, and a higher resolution of 1 meV has also been achieved.<sup>4</sup>

The initial concept of ZEKE shares the same idea as that of threshold photoelectron spectroscopy<sup>5,6</sup>. Figure 1.1 illustrates the processes of PES, TPES and ZEKE spectroscopy. The solid line represents the fixed wavelength of the light source in PES while the dash lines represent the tunable light source in TPES and ZEKE. The difference between TPES and ZEKE is the discrimination method against energetic electrons. Instead of using a steradiancy analyzer, ZEKE adopts a strategy of using a time delay to remove energetic electrons, leaving only zero kinetic energy electrons in the detection area. When a delayed electrical pulse is applied, these ZEKE electrons are then collected. However, earlier experiments showed that the true zero kinetic energy photoelectrons were extremely difficult to observe. This was because these electrons were extremely sensitive to stray fields, which were essentially inevitable in any practical setup. It was soon realized that in a ZEKE experiment<sup>7,8</sup>, it was field ionization of high Rydberg state electrons just below the ionization threshold that contributed to the detected ZEKE signal. These Rydberg state electrons can orbit around a cationic core for a long time (micro to milliseconds)<sup>7,8</sup>, allowing prompt electrons directly ionized from the laser,

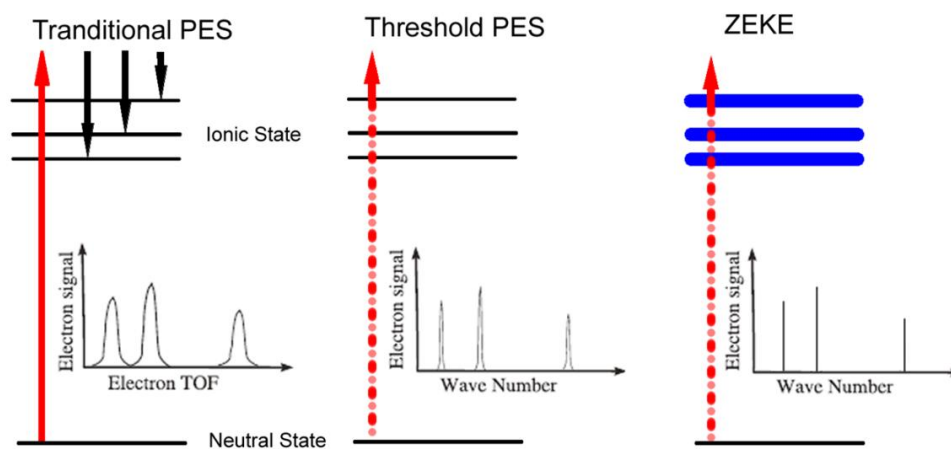


Figure 1.1. Illustrations of PES, TPES and ZEKE. The dashed lines represent tunable light sources.

including the true zero kinetic energy electrons, to escape the detection region. The lifetime of these electrons was further increased because of the stray fields due to Stark effects! Based on continuation of the oscillator strength through the ionization threshold, these Rydberg electrons should reveal the same information as the real ZEKE electrons. Thereafter, these Rydberg electrons have been referred to as “ZEKE electrons” and the associated high Rydberg states are now called “ZEKE states”.

The spectral resolution of ZEKE is determined by the delayed pulsed electric field and the excitation laser, not affected by the discrimination capability of energetic electrons as in typical TPES experiments.<sup>9</sup> Usually in the wavenumber range, resolutions of ZEKE experiments on the order of  $\sim 100$  kHz ( $3 \times 10^{-6}$  cm<sup>-1</sup>) are achievable with careful controls of experimental conditions and narrow linewidth lasers.<sup>10,11</sup>

The high resolution of ZEKE spectroscopy makes it extremely appealing for studies of cation spectroscopy of a variety of species, from small molecules to polyatomics, radicals, van der Waal's complexes, and metal ion containing complexes.<sup>9,12-14</sup> In our own group, we have studied ZEKE spectroscopy of sodium ammonia clusters  $\text{Na} \cdot (\text{NH}_3)_n$  ( $n = 1, 2, \text{ and } 4$ ),<sup>15</sup> a series of heterocyclic and phenyl derivatives, and a few biologically relevant species and their complexes with solvent molecules.<sup>16-21</sup> In many cases, the ionization threshold from our experiment achieves an increase in accuracy of one or two orders of magnitude

over previous reports. The intensity distribution of the vibrational transitions of the cation further reveals the change in molecular structure upon ionization and the distribution of charges. From a fundamental scientific point of view, our work on ZEKE spectroscopy offers the first glimpse into the vibration of a vast variety of ions. For most systems, this type of information has never been attainable prior to our work. More recently, we have successfully combined a laser desorption (LD) source with our ZEKE spectrometer, hence further extending ZEKE to thermally labile species. As reported in a few earlier studies,<sup>7,8,22</sup> a necessary condition of ZEKE is the lifetime extension of ZEKE Rydberg states due to Stark effects of the stray field generated by the prompt ions from direct photoionization to low ionic states. Without sufficient ion density in the detection region, the Rydberg states with principal quantum numbers above 100 cannot survive for more than ~10 ns. Hence to guarantee a sufficient ion density, we have arranged a “chamber within a chamber” in our LD experiment. The detection chamber is enclosed in the source chamber to shorten the distance between the sample source and the detection region, so to guarantee the sample concentration and hence the concentration of prompt ions.

In fact, the lifetime issue of ZEKE Rydberg states further determines that ZEKE is more suitable for studies of low frequency vibrational modes of cations. This is because when associated with lower vibronic states of the cation, the Rydberg states are generally longer lived because of limited number of channels for

autoionization.<sup>23</sup> Although non-Franck-Condon behavior and negligible electronic relaxation of some Rydberg states associated with highly vibrationally and electronically excited cationic states have been reported,<sup>24-26</sup> these reports are considered outliers. This realization has led us into the field of astrophysics on the study of far-infrared vibrational modes of polycyclic aromatic hydrocarbons.

The vibrational information from ZEKE is largely governed by the Franck-Condon principle, and only total symmetric modes or even number harmonics of non-total symmetric modes can be detected. If there were large conformational changes in the molecular frame upon ionization, the Franck-Condon factor would spread into many high vibrational states in many different modes, resulting in weak if any ZEKE signals at the ionization threshold.<sup>27</sup> For highly symmetric species, the Franck-Condon selection rule also dictates that only IR inactive modes should be observable in ZEKE. On the other hand, the energy gap between the first two excited states of some PAHs can be quite small due to extensive configuration interactions in the electronic wavefunction<sup>28,29</sup>, which could cause strong vibronic coupling and activate IR active bands in the intermediate electronic state and the cation ground state.<sup>27</sup>

## **1.2 Background of polycyclic aromatic hydrocarbons**

Polycyclic aromatic hydrocarbons (PAHs) are a group of over 100 compounds, with chemical structures containing more than two fused aromatic

rings and no heteroatoms or substituents. Examples of some common PAHs are shown in Figure 1.2. PAHs can be divided into two groups: cata-condensed and peri-condensed. In cata-condensed PAHs, no carbon is shared by more than two rings, and in peri-condensed PAHs, at least one carbon is shared within three rings. Typically peri-condensed PAHs are considered more stable than their cata-condensed counter parts because of more extensive conjugation. The longest stable cata-condensed PAH is pentacene with five fused rings, while hexacene can only exist in a dimer form and is unstable under ambient conditions.<sup>30</sup>

Atmospheric PAHs can be formed during incomplete combustion of fossil fuels including coal, oil and gas, garbage, or other organic substances like tobacco or charbroiled meat. They can also be found in exhausts from automobile and airplane engines. Many of these PAHs are considered carcinogenic because of their ability to bind with DNA, causing mutation and ultimately resulting in tumors.<sup>31,32</sup> A few PAHs are used as ingredients of industrial compounds like mothballs, glue for plastics, special-purpose skin creams, and anti-dandruff shampoos that contain coal tars.

Outside our planet, PAHs are also believed to exist in the interstellar medium (ISM) of the Milky Way and external galaxies.<sup>33,34</sup> A set of emission bands at 3.3  $\mu\text{m}$ , 6.2  $\mu\text{m}$ , 7.7  $\mu\text{m}$ , 8.6  $\mu\text{m}$  and 11.3  $\mu\text{m}$ , also known as the unidentified infrared emission bands (UIBs), is considered to originate from PAHs.

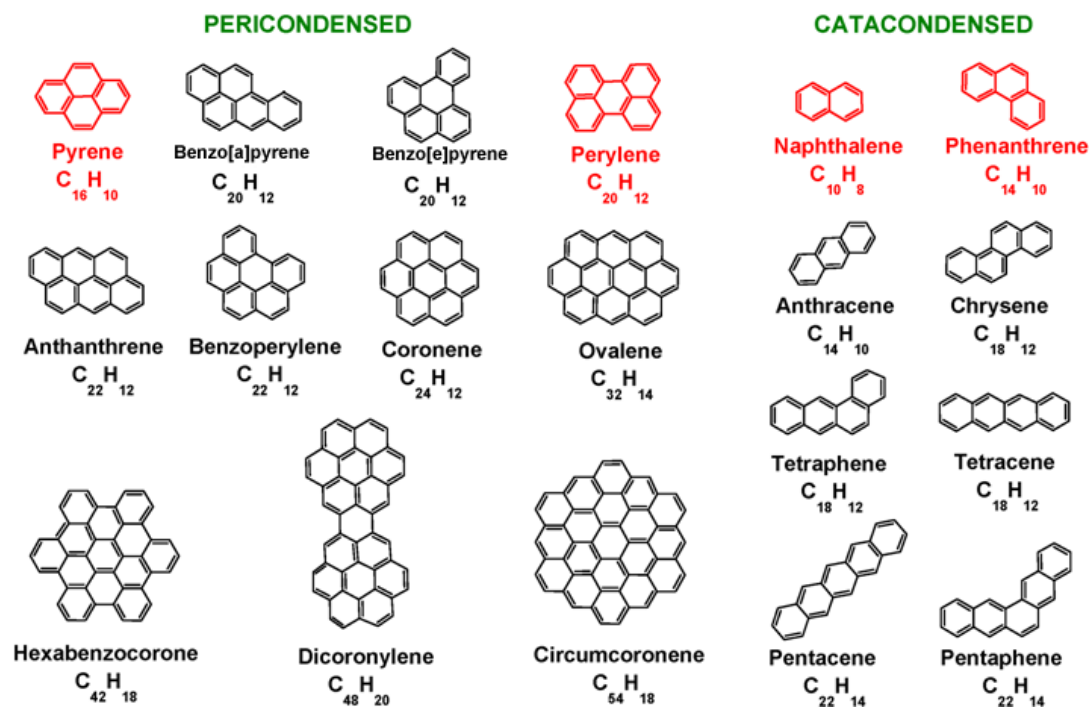


Figure 1.2. Molecular structures of a few PAHs, including both compact peri-condensed molecules and thermodynamically less favored cata-condensed species.

These “UIB” features are generally identified as: C--H stretching mode (3.3  $\mu\text{m}$ ), C--C stretching modes (6.2, 7.7  $\mu\text{m}$ ), C--H in-plane bending mode (8.6  $\mu\text{m}$ ), and C--H out-of-plane bending mode (11.3  $\mu\text{m}$ ).<sup>35,36</sup> Other C--H out-of-plane bending modes at 11.9, 12.7 and 13.6  $\mu\text{m}$  have also been detected. The wavelengths of the C--H out-of-plane bending modes depend on the number of neighboring H atoms: 11.3  $\mu\text{m}$  for solo-CH (no adjacent H atom), 11.9  $\mu\text{m}$  for duet-CH (two adjacent H atoms), 12.7  $\mu\text{m}$  for trio-CH (three adjacent H atoms), and 13.6  $\mu\text{m}$  for quartet-CH (four adjacent H atoms). Other prominent features are the C-C-C bending modes at 16.4  $\mu\text{m}$ <sup>37</sup> and 17.4  $\mu\text{m}$ <sup>38-40</sup>. Given the abundant radiation sources and the low particle density in the outer space, both cations and anions of PAHs may also have significant concentration in the ISM.<sup>41,42</sup>

Extensive efforts have been devoted to the construction of a laboratory database in assisting with identification of the exact molecular formulae of the PAHs in the outer space.<sup>43</sup> A variety of techniques have been explored, such as laser induced fluorescence<sup>44</sup>, photoionization spectroscopy<sup>45</sup>, cavity ringdown<sup>46</sup> and infrared absorption or emission spectroscopy<sup>47</sup>. However, since the 3.3-17.4 $\mu\text{m}$  mid-infrared (MIR) bands are mostly representative of functional groups, or local vibrational modes of the molecule, identification of individual PAHs species has proven ineffective so far. On the other hand, the far-infrared (FIR) bands are considered sensitive to the skeletal characteristics of a molecule. Hence they contain specific fingerprint information on the identity of a PAH molecule.<sup>42,48,49</sup>

Unfortunately, the FIR region was once considered “no man’s land” because of the low sensitivity of most detectors on board of space observatories and in laboratories. Moreover, laboratory experiments in the FIR are further challenged by the lack of adequate light sources and the achievable low ion densities.

With the above realization, NASA and the German Space Agency have commissioned the *Stratospheric Observatory for Infrared Astronomy* (SOFIA) and the *Herschel Space Observatory* to target the FIR and submillimeter (submm) wavelength region of the ISM. The goal is to answer the questions: “*What is the molecular makeup of the ISM and how does that relate to the origin of life?*” In the meantime, the laboratory astrophysics program from NASA has called for proposals on FIR spectroscopy of PAHs and their ions.

The technique of zero kinetic energy photoelectron (ZEKE) spectroscopy offers an indirect solution to the challenges in FIR spectroscopy of PAH cations. As mentioned in Section 1.1, ZEKE is particularly suitable for measurements of low frequency vibrational modes of a cation, because the high Rydberg states in ZEKE are longer lived when they are associated with lower vibronic states of the cation. By detecting electrons from pulsed field ionization in ZEKE spectroscopy, the detector problem in typical FIR and sub-millimeter wave experiments can be avoided. Starting with neutral species and using high energy photons for ionization, ZEKE also eliminates the light source problem in the FIR. The vibrational information from ZEKE is largely governed by the Franck-Condon principle, hence

the information from ZEKE might not be directly applicable for line identification in astronomy. However, by vibronic coupling some IR active modes can be probed. In addition, by offering measurements of several IR forbidden modes, ZEKE can serve as an experimental calibration method for the active bands in the FIR. Moreover, IR forbidden modes are relevant to the modeling of the energy balance in the interstellar medium and to the modeling of PAH emissions with high internal temperatures.<sup>50-54</sup> Hence ZEKE offers complementary information to and fills the gap in techniques of single photon absorption or emission.

### **1.3 Summary**

The central theme of this thesis is to use ZEKE to study cation vibrational spectroscopy of PAHs. Compared with traditional PES, ZEKE offers a much higher energy resolution by two or more orders of magnitude. The ability to study non-volatile species and thermally labile species using our sample sources opens up the size limit of our gas phase experiments. We will not only obtain frequency information, but also analyze the structural stability and the charge distribution of the cation. Our study includes both cata-condensed and peri-condensed species. Together with our collaborator from astrophysics, we hope to offer the necessary laboratory data for PAH identification in the ISM and for astrophysical modeling.

## 1.4 References

- (1) Müller-Dethlefs, K.; Sander, M.; Schlag, E. W. *Chem. Phys. Lett.*, **1984**, *112*, 291.
- (2) Turner, D. W. *Annu. Rev. Phys. Chem.*, **1970**, *21*, 107.
- (3) Villarejo, D. *J. Chem. Phys.*, **1968**, *48*, 4014.
- (4) King, G. C.; Yench, A. J.; Lopes, M. C. A. *J. Electron. Spectrosc. Relat. Phenom.*, **2001**, *114-116*, 33.
- (5) Peatman, W. B.; Borne, T. B.; Schlag, E. W. *Chem. Phys. Lett.*, **1969**, *3*, 492.
- (6) Chupka, W. A. *J. Chem. Phys.*, **1993**, *99*, 5800.
- (8) Chupka, W. A. *J. Chem. Phys.*, **1993**, *98*, 4520.
- (9) Schlag, E. W. *ZEKE Spectroscopy*; Cambridge University Press: London, 1998.
- (10) Merkt, F.; Schmutz, H. *J. Chem. Phys.*, **1998**, *108*, 10033.
- (11) Osterwalder, A.; Merkt, F. *Phys. Rev. Lett.*, **1999**, *82*, 1831.
- (12) Cockett, M. C. R.; Kimura, K. *J. Chem. Phys.*, **1994**, *100*, 3429.
- (13) Yang, D.-S.; Zgierski, M. Z.; Rayner, D. M.; Hackett, P. A.; Martinez, A.; Salahub, D. R.; Roy, P.-N.; Carrington, T. *J. Chem. Phys.*, **1995**, *103*, 5335
- (14) Cockett, M. C. R.; Goode, J. G.; Lawley, K. P.; Donovan, R. J. *J. Chem. Phys.*, **1995**, *102*, 5226.
- (15) Peng, X.; Kong, W. *J. Chem. Phys.*, **2002**, *117*, 9306.
- (16) He, Y.; Wu, C.; Kong, W. *Chem. Phys. Lett.*, **2004**, *391*, 38.
- (17) He, Y.; Wu, C.; Kong, W. *J. Chem. Phys.*, **2005**, *109*, 2809.
- (18) He, Y.; Kong, W. *The J. Chem. Phys.*, **2006**, *124*, 2043061.
- (19) He, Y.; Wu, C.; Kong, W. *J. Chem. Phys.*, **2004**, *121*, 8321.
- (20) He, Y.; Wu, C.; Kong, W. *J. Chem. Phys.*, **2004**, *121*, 3533.
- (21) Wu, C.; He, Y.; Kong, W. *Chem. Phys. Lett.*, **2004**, *398*, 351.
- (22) Merkt, F.; et al. *J. Phys. B: At. Mol. Opt. Phys.*, **1998**, *31*, 1705.
- (23) Matsui, H.; Behm, J. M.; Grant, E. R. *J. Phys. Chem. A*, **1997**, *101*, 6717.
- (24) Kong, W.; Rodgers, D.; Hepburn, J. W. *Proc. SPIE*, **1993**, *1858*, 201.
- (25) Kong, W.; Rodgers, D.; Hepburn, J. W. *Chem. Phys. Lett.*, **1994**, *221*, 301.
- (26) Kong, W.; Hepburn, J. W. *Can. J. Phys.*, **1994**, *72*, 1284.
- (27) Dessent, C. E. H.; Geppert, W. D.; Ullrich, S.; Müller-Dethlefs, K. *Chem. Phys. Lett.*, **2000**, *319*, 375.
- (28) Dierksen, M.; Grimme, S. *J. Chem. Phys.*, **2004**, *120*, 3544.
- (29) Small, G. *J. Chem. Phys.*, **1971**, *54*, 3300.
- (30) Mondal, R.; Adhikari, R. M.; Shah, B. K.; Neckers, D. C. *Org. Lett.*, **2007**, *9*, 2505.
- (31) Kriek, E.; Rojas, M.; Alexandrov, K.; Bartsch, H. *Mutat. Res. Fundam. Mol. Mech. Mugag.*, **1998**, *400*, 215.

- (32) Smith, L. E.; Denissenko, M. F.; Bennett, W. P.; Li, H.; Amin, S.; Tang, M.-s.; Pfeifer, G. P. *J. Natl. Cancer Inst.*, **2000**, *92*, 803.
- (33) Li, A. PAHs in Comets: An Overview. In *Deep Impact as a World Observatory Event: Synergies in Space, Time, and Wavelength*; Kaufl, H. U., Siebenmorgen, R., Moorwood, A. F. M., Eds.; Springer: Berlin, 2009; pp 161.
- (34) Gillett, F. C.; Forrest, W. J.; Merrill, K. M. *Astrophys. J.*, **1973**, *183*, 87.
- (35) Allamandola, L. J.; Tielens, A. G. G. M.; Barker, J. R. *Astrophys. J.*, **1985**, *290*, L25.
- (36) L  ger, A.; Puget, J., L. *Astron. Astrophys.*, **1984**, *137*, L5.
- (37) Moutou, C.; Leger, A.; D'Hendecourt, L. *Astron. Astrophys.*, **1996**, *310*, 297.
- (38) Beintema, D. A.; van den Ancker, M. E.; Molster, F. J.; Waters, L. B. F. M.; Tielens, A. G. G. M.; Waelkens, C.; de Jong, T.; de Graauw, T.; Justtanont, K.; Yamamura, I.; Heras, A.; Lahuis, F.; Salama, A. *Astron. Astrophys.*, **1996**, *315*, L369.
- (39) Smith, J. D. T.; Dale, D. A.; Armus, L.; Draine, B. T.; Hollenbach, D. J.; Roussel, H.; Helou, G.; Kennicutt, R. C.; Li, A.; Bendo, G. J.; Calzetti, D.; Engelbracht, C. W.; Gordon, K. D.; Jarrett, T. H.; Kewley, L.; Leitherer, C.; Malhotra, S.; Meyer, M. J.; Murphy, E. J.; Regan, M. W.; Rieke, G. H.; Rieke, M. J.; Thornley, M. D.; Walter, F.; Wolfire, M. G. *Astrophys. J. Suppl. Ser.*, **2004**, *154*, 199.
- (40) Smith, J. D. T.; Draine, B. T.; Dale, D. A.; Moustakas, J.; Kennicutt, J. R. C.; Helou, G.; Armus, L.; Roussel, H.; Sheth, K.; Bendo, G. J.; Buckalew, B. A.; Calzetti, D.; Engelbracht, C. W.; Gordon, K. D.; Hollenbach, D. J.; Li, A.; Malhotra, S.; Murphy, E. J.; Walter, F. *Astrophys. J.*, **2007**, *656*, 770.
- (41) Sloan, G. C.; Hayward, T. L.; Allamandola, L. J.; Bregman, J. D.; DeVito, B.; Hudgins, D. M. *Astrophys. J.*, **1999**, *513*, L65.
- (42) Langhoff, S. R. *J. Chem. Phys.*, **1996**, *100*, 2819.
- (43) Tielens, A. G. G. M. *Annu. Rev. Astron. Astrophys.*, **2008**, *46*, 289.
- (44) Borisevich, N. A.; Vodovatov, L. B.; D'yachenko, G. G.; Petukhov, V. A.; Semyonov, M. A. *J. Appl. Spectrosc.*, **1995**, *62*, 482.
- (45) Qi, F.; Yang, R.; Yang, B.; Huang, C.; Wei, L.; Wang, J.; Sheng, L.; Zhang, Y. *Rev. Sci. Instrum.*, **2006**, *77*, 084101.
- (46) Biennier, L.; Salama, F.; Gupta, M.; O'keefe, A. *Chem. Phys. Lett.*, **2004**, *387*, 287.
- (47) Ruiterkamp, R.; Halasinski, T.; Salama, F.; Foing, B. H.; Allamandola, L. J.; Schmidt, W.; Ehrenfreund, P. *Astron. Astrophys.*, **2002**, *390*, 18 pages.
- (48) Joblin, C.; Bern   O.; Simon, A.; Mulas, G. *arXiv:0904.3185*, **2009**.
- (49) Zhang, K.; Guo, B.; Colarusso, P.; Bernath, P. F. *Science*, **1996**, *274*, 582.
- (50) Draine, B. T.; Li, A. *Astrophys. J.*, **2001**, *551*, 807.
- (51) Draine, B. T.; Li, A. *Astrophys. J.*, **2007**, *657*, 810.
- (52) Li, A.; Draine, B. T. *Astrophys. J.*, **2001**, *554*, 778.
- (53) Li, A.; Draine, B. T. *Astrophys. J.*, **2002**, *576*, 762.
- (54) Li, A.; Luning, J. I. *Astrophys. J.*, **2003**, *594*, 987.

## Chapter 2 Experimental Setup

### 2.1 General Description

The experimental apparatus consists of three major components: sample source, spectrometer and laser system. The overall setup is illustrated in Figure 2.1. The sample source can be either a laser desorption source or a heating source. The vaporized sample is supersonically cooled and entrained by a pulsed jet of inert gases such as helium or argon. The supersonic molecular beam enters through a collimation skimmer into the detection chamber where the Resonance Enhanced Multi-Photon Ionization (REMPI) and ZEKE spectrometer is housed. In the detection chamber, the molecular beam perpendicularly encounters the counter propagating coherent excitation and ionization lasers between the first two electrodes of the spectrometer. The resulting ions or electrons are detected by a set of multichannel plates (MCP) after passing through a flight tube.

The vacuum system consists of two chambers: source chamber and detection chamber. The detection chamber is enclosed in the source chamber to shorten the distance between the sample source and the detection region. Three tubes extended from the inner chamber to the window areas of the exterior chamber separate the two chambers. The detection chamber is pumped by a turbomolecular pump (Varian, Turbo V-550) mounted upside down on top of the chamber, and the

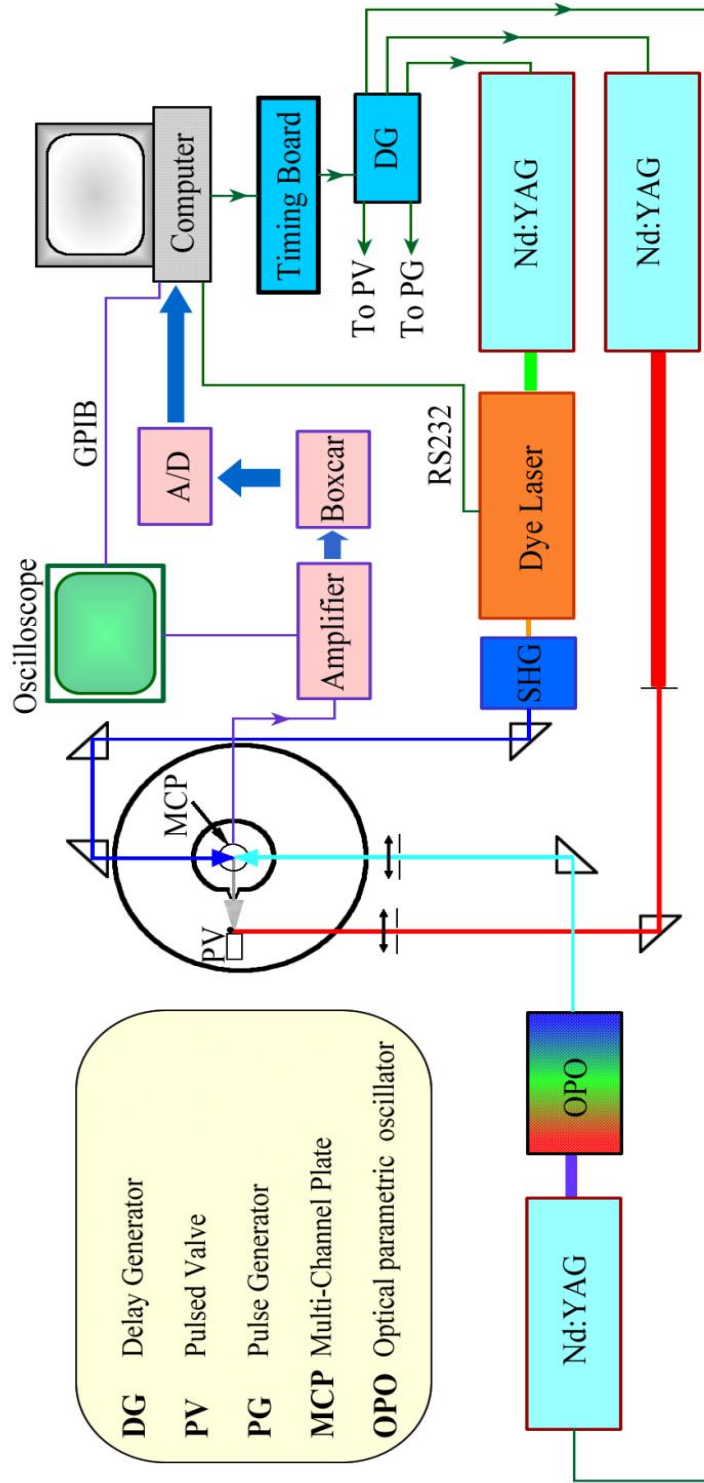


Figure 2.1 Experimental layout and signal processing.

source chamber is pumped by a diffusion pump (Varian, VHS 6) mounted underneath. The two chambers are connected by a homemade skimmer with a diameter of 1 mm. The schematic of the vacuum system is shown in Figure 2.2 and the chamber layout is shown in Figure 2.3. The pressure in the source chamber is slightly higher than that of the detection chamber. Typical values of the pressure are  $1.0 \times 10^{-6}$  torr in the source chamber and  $4.0 \times 10^{-7}$  torr in the detection chamber when the pulsed valve is closed, and  $\sim 10^{-6}$  torr when the pulsed valve is in operation.

The ionization threshold of most PAH molecules fall in the vacuum ultraviolet region. In our experiments, this high energy is achieved via two UV photons, one of which is typically resonant with an intermediate vibronic state. The coherent tunable light sources in the UV region are often obtained by frequency doubling of the output of dye lasers or the optical parametric oscillator using BBO or KDP crystals. We use three Nd:YAG lasers (Spectra Physics GCR 190, GCR 230 and Precision I 8000, Continuum) with frequency doubling or tripling units to pump two dye lasers (Laser Analytical Systems; LDL 20505 and LDL 2051) and an optical parametric oscillator (OPO, Panther, Continuum). The laser dyes involved in this study are summarized in Table 2.1. The solvent is methanol for those in the visible including coumarin, rhodamin and pyridine, and dioxane for those in the UV such as exalite (Exciton). In cases of wavelength discontinuity covered by two different dyes, mixtures of different dyes are adopted.

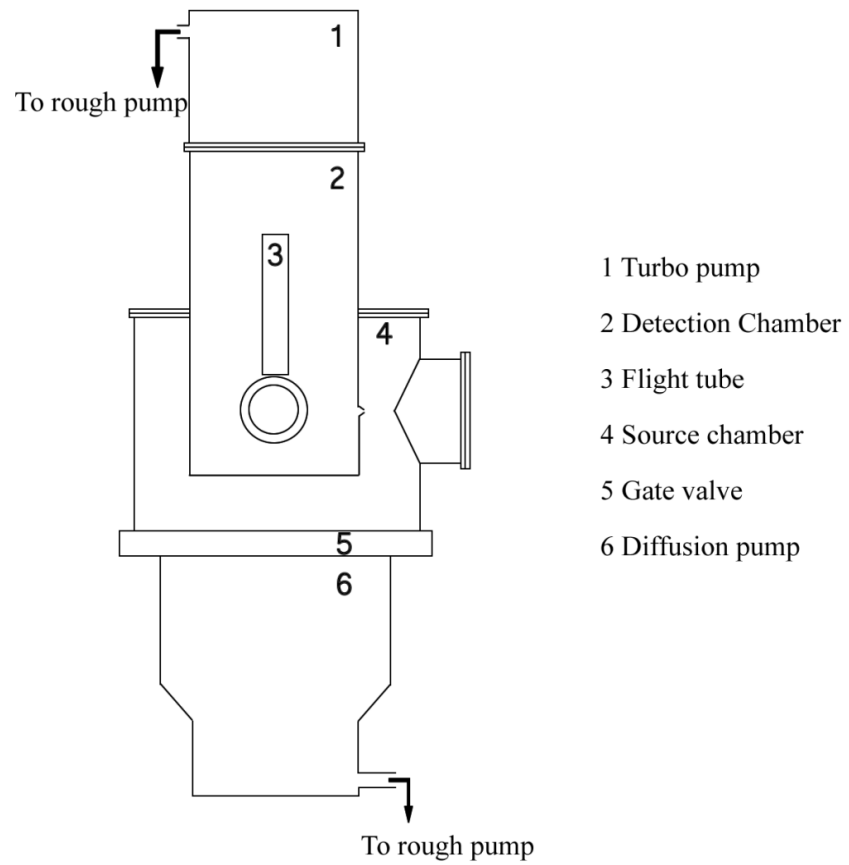


Figure 2.2 Schematic of the vacuum system.

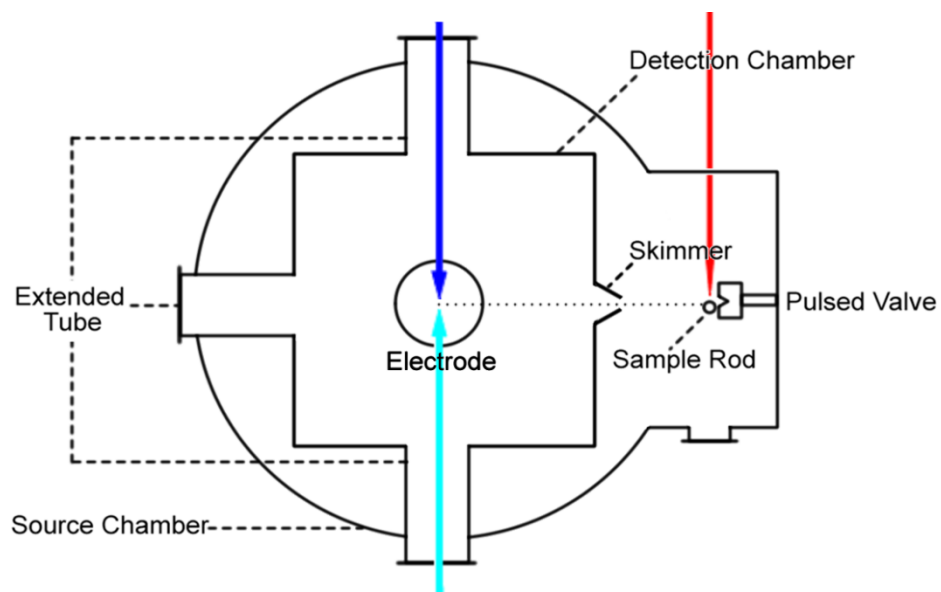


Figure 2.3 Schematic of the differentially pumped molecular beam system.

Table 2.1. Summary of laser dyes involved in the experiment

Laser Dye	Pumping Wavelength (nm)	Peak Wavelength (nm)	Tuning Range (nm)
Exalite 376	355	376	369-381
Exalite 389	355	389	378-395
Exalite 398	355	398	393-403
Exalite 404	355	404	399-410
Exalite 416	355	416	404-426
Coumarin 2	355	450	435-467
Coumarin 47	355	454	440-475
Coumarin 102	355	480	462-497
Coumarin 307	355	508	485-546
Coumarin 540A	355	543	523-586
Rhodamine 6G	532	560	553-577
Rhodamine 610	532	582	576-600
Sulforhodamine	532	609	603-630
DCM	532	642	604-672
Pyridine 1	532	698	664-724
Pyridine 2	532	750	725-776

The mixture is prepared with a proper proportion so that a nearly constant laser power throughout the whole scanning range is obtained. The efficiency of the dye lasers is 10 ~ 20% of the pumping lasers (normally ~150 mJ/pulse), and the efficiency of the frequency doubling units from the dye lasers is usually 10% of the dye laser fundamental energy. A typical linewidth of the frequency doubled output of a dye laser is  $0.5 \text{ cm}^{-1}$  and the linewidth of the OPO is  $3 \text{ cm}^{-1}$ .

## **2.2 Sample Source**

### **2.2.1 Supersonic Molecular Beam**

We used a pulsed valve (General valve, series 9) for supersonic cooling and entrainment of the non-volatile sample. A homemade driver is used to provide the necessary pulse with a high current, up to 10 A, to the valve. A typical pressure of the carrier gas is 1 ~ 3 atm for helium and argon, and up to 8 atm in some cases for better cooling results. The opening time of the nozzle is about 400  $\mu\text{s}$  in full-width-at half-max, and the nozzle diameter is either 1 mm or 2 mm.

### **2.2.2 Laser Desorption Source**

A laser desorption source, as illustrated in Figure 2.4, was used in the studies of tetracene and pentacene. The source consists of a 1/8" graphite rod coated with a thin layer of sample and two counter-rotating wheels mounted on a

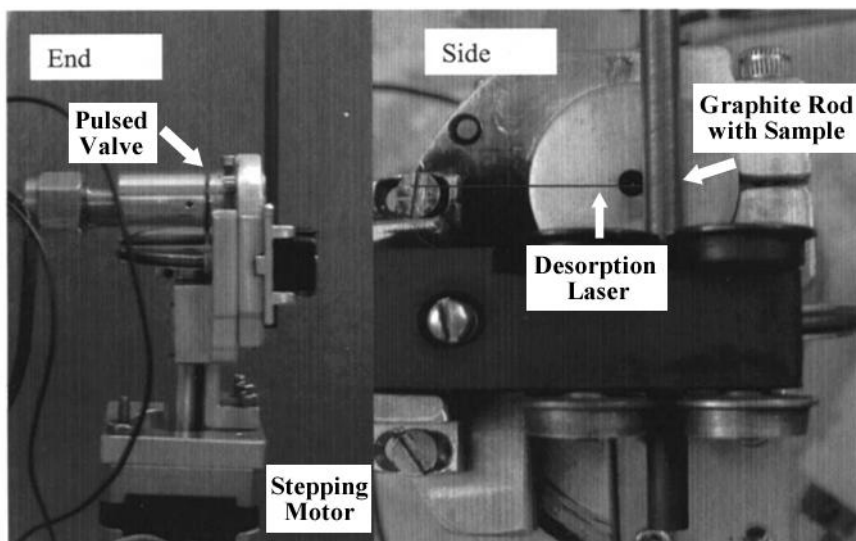


Figure 2.4 Details of the laser desorption source.

stepping motor. The wheels press the rod against the surface of the pulsed valve and the rod is positioned 0.5 mm to one side of the nozzle. The pitch of translation of the rod is adjustable by the angle of the two wheels, and the direction of translation is controlled by the sense of rotation. The overall operating time of each rod is determined by the length of the rod, which is limited by the diameter of the chamber to be 5.5". Typically, each complete round trip of the sample rod takes about 6 – 8 hours. The sample is smudged onto the rod by hand, and before each usage, the graphite rod is cleaned with sand paper to rid of the grooves generated during previous experiments. The desorption laser (Spectra Physics GCR 230) at 1064 nm with a pulse energy of ~0.06 mJ/pulse is focused onto the rod with a lens of 6" in focal length. The internal temperature of the desorbed molecules is very sensitive to the power and position of the desorption laser. Typically, the closer the desorption position to the nozzle, the cooler the resulting species. On the other hand if the desorption position is too close to the nozzle, the desorbed molecules would be blocked by the rod itself and hence reducing the efficiency of desorption. Normally we focus the desorption laser on the rod 1.5 mm from the surface of the pulsed valve downstream the supersonic expansion.

### **2.2.3 Heating Source**

A heating source is used in the experiments of benzo[*g,h,i*]perylene, pyrene and benzo[*a*]pyrene. The original nozzle flange of the pulsed valve is replaced by a

homemade double walled stainless steel cylinder with a 1 mm diameter nozzle. The PAH samples are placed between the two walls of the stainless steel cylinder and heated by a coiled heater with a resistance of 50 ohms. A variac set at 20 – 40 V provides AC power to the heater, and the temperature is monitored by a controller (Omega, CN370). The highest operational temperature of the heated sample source is 220 °C, above which, the mechanism of the pulsed valve becomes unstable. Typically, 10 ~ 20 mg of sample is sufficient for the whole experiment under proper operational temperatures.

## **2.3 PFI – ZEKE Spectrometer**

### **2.3.1 Spectrometer Construction**

The schematic of the PFI – ZEKE spectrometer is illustrated in Figure 2.5. The spectrometer consists of three electrodes, a 2-inch flight tube and a set of multichannel plate detector. The axis of the spectrometer is perpendicular to the molecular beam and the laser beams. The pulsed supersonic molecular beam passes through a 1 mm skimmer and enters the region between the first two electrodes. The excitation and ionization lasers intersect the molecular beam in the same region.

The spectrometer can be operated as a time-of-flight mass spectrometer (TOF-MS), or a PFI-ZEKE spectrometer. The MCP detector is designed for both

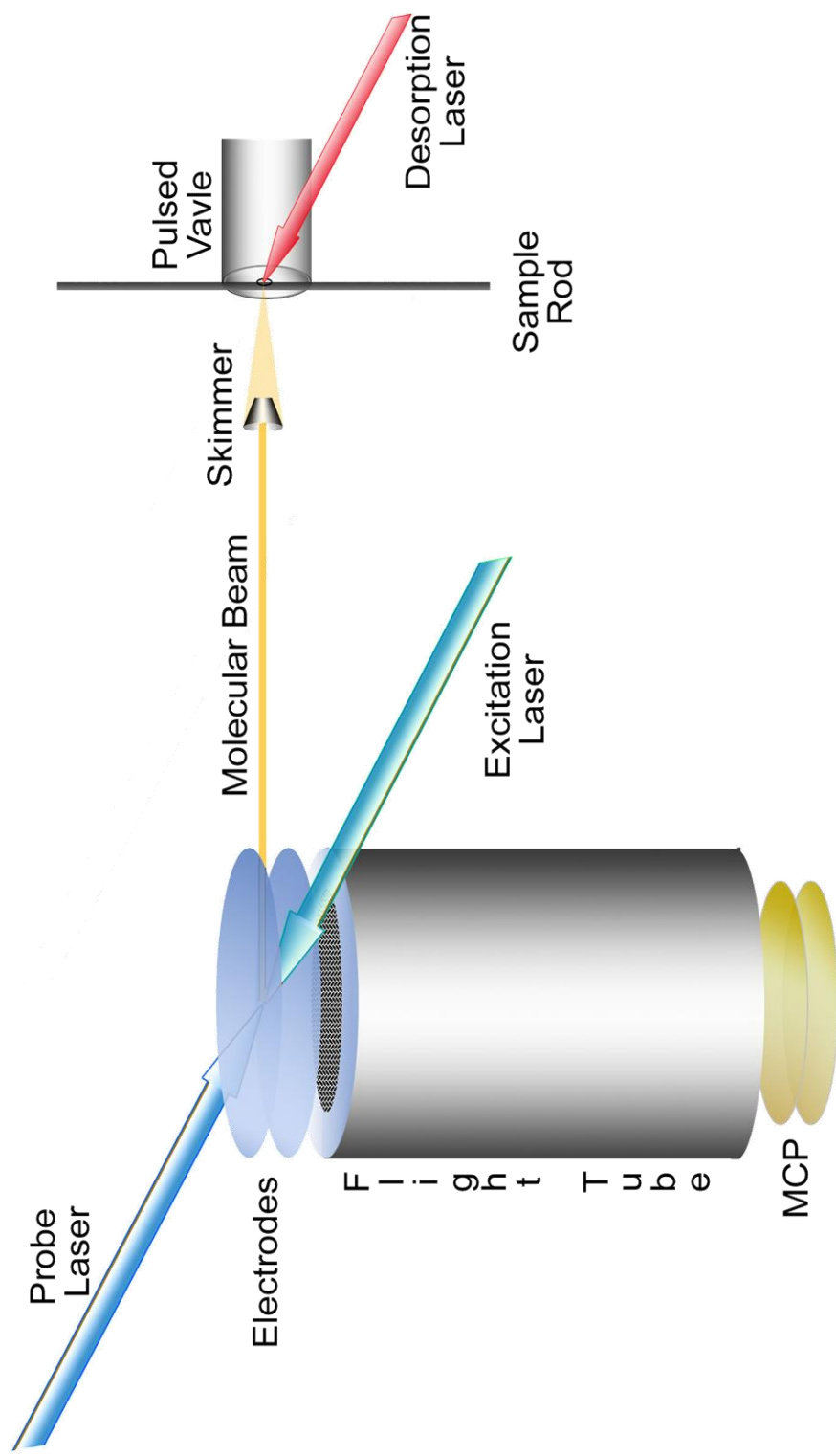


Figure 2.5 ZEKE spectrometer with a laser desorption source

ion and electron detection. Time zero in the TOF spectrum is defined by the laser pulse. In a REMPI experiment, a scanning laser excites the molecules to an intermediate resonant state, and another laser set at a short wavelength to ionize the excited molecules. By scanning the excitation laser, the resonant vibrational levels of the excited electronic state can be mapped out. In a ZEKE experiment, the excitation laser is set at one of the specific intermediate vibronic levels determined from the REMPI experiment, and the ionization laser is then tuned through the different vibrational levels of the cation.

### **2.3.2 TOF-MS Mode**

The first step of all experiments is to find out the right condition for the sample source. This is achieved by varying the conditions of the sample source such as the heating temperature/strength of the desorption laser, the pressure of carries gas and the timing between the pulsed valve and detection lasers, while searching for the parent ion in the TOF-MS. Ionization of the neutral sample is achieved by one or two lasers. Prior to the experiment, some information on the ionization threshold is necessary, and an electric dipole allowed stable intermediate electronic state needs to be chosen for resonant enhancement. If the energy of this intermediate state is above half of the ionization threshold, two photons from the same laser are sufficient to ionize the molecules, hence only one focused laser beam is needed. Otherwise, a second laser with a fixed higher energy is

synchronized with the resonant excitation laser for ionization. Under this mode, the first electrode is grounded and the other two electrodes are negatively biased. The sample and background oil molecules are ionized between the first two electrodes by the UV laser(s). The background oil ion signal is hard to remove from the system. The oil ion signal can cause some problems when the molecules interested has a similar molecular mass as oil, but it can also serve as an internal standard of mass for the interested species. Masses of the species can be calculated based on their time-of-flight. The operating voltages on the electrodes and MCP are listed in Table 2.2.

Once the sample condition is optimized for the best parent ion signal, a two laser REMPI experiment is performed by scanning one laser for resonant excitation, setting the second laser at a fixed wavelength short enough for further ionization, and monitoring the parent ion. The resulting spectrum of the intermediate state can then be analyzed. There are two possible failure mechanisms at this step: one is insufficient cooling due to poor alignment of the molecular beam component, inadequate stagnation pressure in the pulsed valve, incorrect heating temperature, wrong timing between the desorption laser and the molecular beam. The other is ultrashort lifetimes of the excited state, where lifetime broadening obliterates all vibronic features.

Table 2.2 Voltage settings of TOF-MS and ZEKE spectrometer.

	First electrode	Second electrode	Flight Tube	MCP
TOF-MS	0	-80 V	-255 V	-2.1 kV
ZEKE	Pulsed*	~200 mV-0 V	+18 V	+2.1 kV

\*Pulse delay: 300 ns ~700 ns;

Amplitude: -2 V~-5 V;

Width: 200 ns ~ 800 ns;

DC offset: 0 V

### 2.3.2 PFI-ZEKE Mode

Once a vibrationally resolved REMPI spectrum is obtained, a search for the ionization threshold will ensue. For this purpose, we set the excitation laser at the origin of the excited state, scan the ionization laser from short wavelength to long wavelength, and monitor the intensity of parent ion signal. Once the ion signal shows a sharp drop with wavelength, we believe that the ionization threshold should be close in energy. Based on our experience, if the ion signal shows a clear drop within 2 nm of the scanning ionization laser, ZEKE via the origin of the intermediate electronic state should be possible. If the ion signal drop has a flat slope and lasts for more than 5 nm as the ionization laser scans, ZEKE is disfavored because of low Franck-Condon factors.

If the threshold of ionization is deemed “sharp” enough and ZEKE is considered favorable, the spectrometer is reset for PFI-ZEKE. In this mode, the voltage on the first electrode is zero and a very low negative voltage is applied to the second electrode to generate a spoiling field. Once the lasers fire, the spoiling field accelerates the prompt electrons toward the first electrode and hence eliminates them from the detection area, while only the long-lived Rydberg state neutral molecules remain in the excitation region. After a delay of 300 ns ~ 700 ns, a negative pulse is applied to the first electrode, ionizing the Rydberg electrons (the ZEKE electrons) and accelerating them toward the flight tube. It takes about 30 ns for the ZEKE electrons to pass through the flight tube and reach the MCP detector.

A pulse generator (Systron Donner 114A) is used to supply the delayed negative pulse to the first electrode. To reduce the interference of the pulse to other electrodes and the detector, a coaxial cable is used inside the chamber to deliver the pulse. Though the cable is terminated by a 50 ohm resistor on the electrode, a ringing effect is still observable. The operational voltage setting in PFI-ZEKE mode for the electrodes and MCP is listed in Table 2.2.

## 2.4 System Timing

The whole system operates in a pulsed mode with a 10 Hz repetition rate. The timing sequence is illustrated in Figure 2.6. The master clock is provided by a timing board (CIO-CTR 10) installed in the computer, and the rest of the synchronization pulses are provided by delay generators (SRS DG535). Each laser requires two trigger pulses, a trigger to the flash lamp and a trigger to the Q-switch. The delay between the two trigger pulses is typically 200  $\mu$ s. Channels A and B of delay generator 2 are used to trigger the desorption laser. Channel A sends a pulse to trigger the flash lamp of the desorption Nd:YAG, and B is set 207  $\mu$ s after channel A and triggers the Q-switch of the laser. The “C $\square$ L D” channel of delay generator 1 supplies the trigger to the pulsed valve. The delay of the trigger is determined by Channel C and the width of the trigger is determined by the setting of channel D relative to channel C. Channels A and B of delay generators 1 and 3 are used to trigger the lamp and Q-switch of the Nd:YAG lasers for excitation and

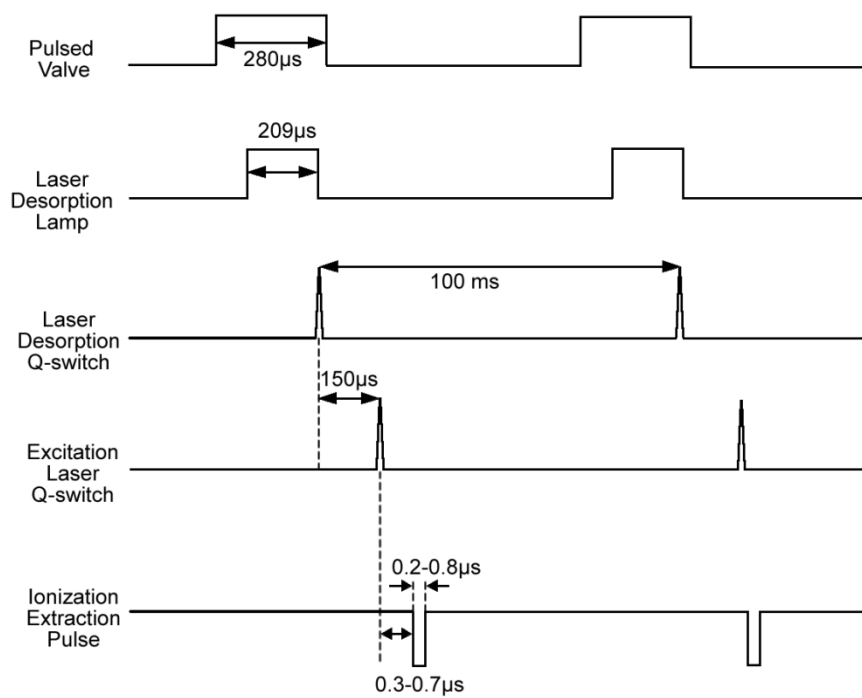


Figure 2.6 Timing diagram of the PFI-ZEKE experiment

Table 2.3 Typical settings of the delay generators.

	Channel	Laser Desorption Source	Heating Source
DG 535 No 1	T	Triggered by timing board	Triggered by timing board
	A	= T + 2104 $\mu$ s	= T + 2100 $\mu$ s
	B	= A + 209 $\mu$ s	= A + 209 $\mu$ s
	C	= T + 1870 $\mu$ s	= T + 1773 $\mu$ s
	D	= C + 280 $\mu$ s	= C + 300 $\mu$ s
DG 535 No 2	T	Triggered by timing board	Triggered by timing board
	A	= T + 1938 $\mu$ s	
	B	= A + 209 $\mu$ s	
DG 535 No 3	T	Triggered by timing board	Triggered by timing board
	A	= T + 2014 $\mu$ s	= T + 2010 $\mu$ s
	B	= A + 209 $\mu$ s	= A + 209 $\mu$ s

ionization. Typical settings of the delay generators are listed in Table 2.3.

The pulsed valve receives the earliest trigger because of the mechanical delay of the valve's solenoid and the travel time of the sample from the source chamber to the excitation region. The flash lamp of the desorption laser is then triggered  $\sim 70 \mu\text{s}$  later. The flash lamps of the excitation laser and the ionization laser are triggered  $\sim 150 \mu\text{s}$  after the desorption laser. Both laser beams encounter the molecular beam in the middle of the ionization chamber between the first two electrodes.

Figure 2.7 shows the timing profiles of the pulsed valve and of the desorbed sample entrained in the molecular beam. The x axis displays the setting on the delay generator. Trace (a) was recorded when the sample coronene was smudged on a graphite rod, and the opening timing of pulsed valve was varied with the timing of desorption laser and detection laser fixed. The resulting ion intensity thus reflects the effectiveness of the supersonic molecular beam for sample entrainment. The desorption event needs to happen right after the pulsed valve opens, so that the desorbed sample are cooled and entrained by the front edge of the molecular beam. Trace (b) was recorded with the same setup but with pyrimidine in the pulsed valve. The intensity of the pyrimidine ion as a function of the delay time between the pulsed valve and the excitation laser is thus a reflection of the timing and hence spatial profile of the molecular beam. From this comparison, we

conclude that only the leading edge of the molecular beam contains the sample, while the tail of the beam has no effect.

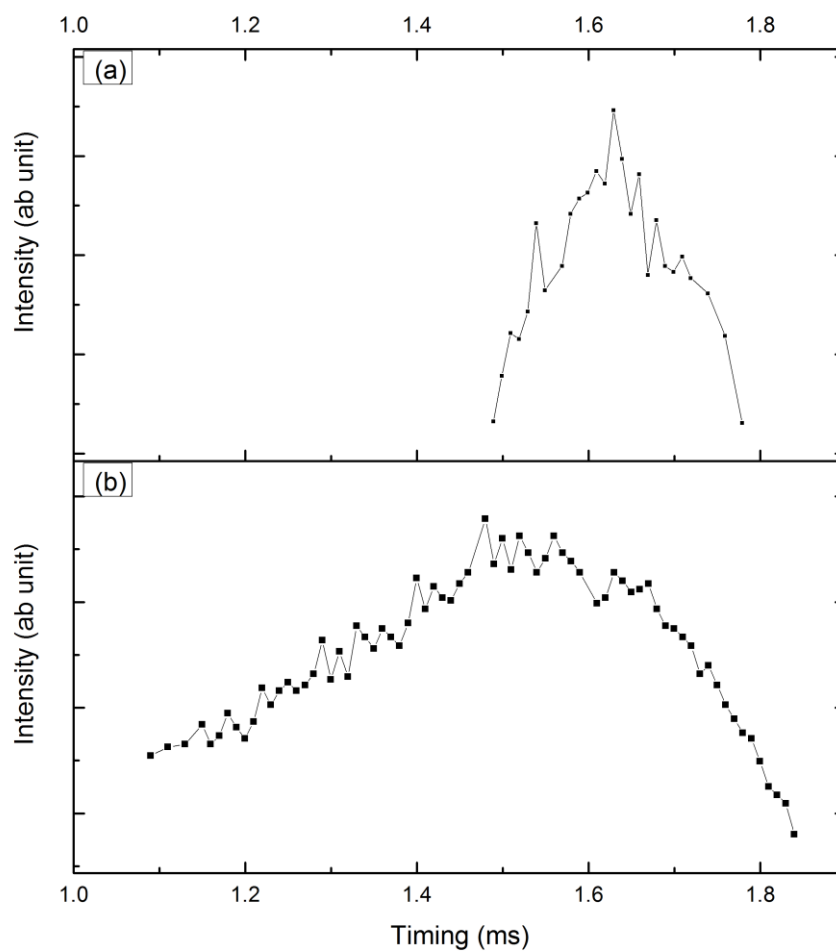


Figure 2.7. Timing profiles of the pulsed valve and of the desorbed sample in the molecular beam. (a) Intensity of laser desorbed coronene ions vs. the delay time between the pulsed valve and the excitation laser. (b) Intensity of pyrimidine enclosed in the pulsed valve vs the delay time between pulsed valve and the excitation laser.

**Zero kinetic energy photoelectron spectroscopy of tetracene using laser  
desorption for vaporization**

Jie Zhang, Linsen Pei, and Wei Kong\*

Department of Chemistry, Oregon State University, Corvallis, Oregon 97331-4003

Journal of Chemical Physics  
American Institute of Physics, Suite 1NO1, 2 Huntington Quadrangle  
Melville, NY 11474-4502, USA  
**2008**, *128*, 104301

---

\* To whom correspondence should be addressed.  
Fax: 541-737-2062. Electronic mail: [wei.kong@oregonstate.edu](mailto:wei.kong@oregonstate.edu).

## Chapter 3 Zero kinetic energy photoelectron spectroscopy of tetracene using laser desorption for vaporization

### 3.1 Abstract

Far infrared (FIR) spectroscopy of polycyclic aromatic hydrocarbons is of particular interest to astrophysics since vibrational modes in this range are representative of the molecular size and shape. This information is hence important for identification of chemical compositions and for modeling of the IR spectrum observed in the outer space. In this work, we report neutral and cation FIR spectroscopy of tetracene vaporized from a laser desorption source. Results from two-color resonantly enhanced multiphoton ionization and two-color zero kinetic energy photoelectron spectroscopy will be presented. Several skeletal vibrational modes of the first electronically excited state of the neutral species and those of the cation are assigned, with the aid of *ab initio* and density functional calculations. The adiabatic ionization potential is determined to be  $55918 \pm 7 \text{ cm}^{-1}$ . Interestingly, all observed vibrational modes can be rationalized based on a simple Hückle calculation, i.e., by observing the addition or elimination of nodal planes due to electronic excitation and/or ionization. Limited by the Franck-Condon principle and the rigidity of the molecular frame of tetracene, only IR forbidden modes are observed in this work.

### 3.2 Introduction

Polycyclic aromatic hydrocarbons (PAHs) consist of fused aromatic rings without heteroatoms or substituents. They are an important category of compounds that are prevalent in combustion environments, interstellar medium, and cometary dusts.<sup>1</sup> They have strong impacts on human health and, interestingly, they are also suspected to be related to the origin of life in the universe.<sup>2,3</sup> PAH molecules and their cations are proposed to be carriers of the ubiquitous unidentified infrared bands and the diffuse interstellar bands.<sup>4-6</sup> However, for a definitive identification of a particular PAH or cation in the interstellar medium, precise frequency and line strength information are needed, particularly in the far infrared (FIR) region (less than  $1000\text{ cm}^{-1}$ ).<sup>7</sup> This is because vibrational modes in the FIR are specific to the skeletal characteristics of the molecule,<sup>8,9</sup> and hence are considered fingerprints of specific PAH molecules. In contrast, higher frequency modes are related to functional groups and are not sensitive to the overall molecular frame. Moreover, to model the infrared emission from different astrophysical environments,<sup>10-13</sup> in particular, to support the imminent Herschel Space Observatory, FIR spectroscopy is in urgent demand.

Most PAH compounds are nonvolatile and have high ionization thresholds, in the vacuum ultraviolet region. Gas phase studies of PAH cations are therefore hindered by challenges in both vaporization and ionization. In the past, extensive efforts have been devoted to vibrational spectroscopy of neutral compounds using

the matrix isolation spectroscopy (MIS) method.<sup>14-17</sup> Although these efforts have been extremely successful, for ionic species, sample preparation is difficult and matrix effects are somewhat unpredictable. To date, only a limited number of PAH cations have been investigated experimentally in the near and mid IR regions.<sup>18-24</sup>

Vibrational information in the FIR region, either for neutral or ionic compounds, is further hindered by the ready availability of light sources and detectors. This spectral region is considered “no man’s land,” because neither typical infrared nor microwave techniques are applicable. Although in recent years, terahertz spectroscopy, mostly in the time domain, has emerged to fill this void, the technique has not become a major contributing force.<sup>25</sup> FIR transitions of PAH cations are essentially unreported experimentally. In the meantime, the importance of this spectral region for astrophysical research has prompted many theoretical efforts.<sup>26,27</sup> Experimental calibrations of vibrational frequencies, particularly for charged species, are therefore imperative.

We have recently adopted a laser desorption (LD) source to vaporize nonvolatile compounds,<sup>28-31</sup> and used the zero kinetic energy photoelectron (ZEKE) spectroscopy technique to obtain vibrational information of cations,<sup>32</sup> particularly in the FIR region. In our experiment, we use a low power pulsed infrared laser for desorption so that neutral gas phase species, not plasma ions, can be ejected from a graphite substrate. The fast efficient heating from the pulsed laser minimizes fragmentation and subsequent entrainment by a supersonic jet of argon results in a low internal temperature. LD has been proven highly effective in vaporization of

nonvolatile organic and biological molecules.<sup>28-31</sup> The ZEKE technique is known as a high resolution method of photoionization spectroscopy.<sup>32</sup> It is ideal for the study of vibrational spectroscopy of cations, particularly for low frequency modes, since these vibrational levels are close to the ionization threshold and are likely to have long lived Rydberg states.

In this paper, we report studies of two-color two photon resonantly enhanced multiphoton ionization (REMPI) and ZEKE spectroscopy of tetracene. Detailed spectroscopic analysis for the vibrational levels of the  $S_1$  state and the ground cationic state  $D_0$  will be discussed, with the assistance of *ab initio* and density functional calculations. Structural changes due to electronic excitation and ionization will be elucidated from the observed active vibrational modes and from comparisons between the REMPI and ZEKE spectra.

### 3.3 Experimental Setup

The experimental apparatus is a differentially pumped system containing a laser desorption source and a time of flight mass spectrometer, as shown in Figure 3.1. The detection chamber is enclosed in the source chamber to shorten the distance between the sample source and the detection region. Three tubes extended from the inner chamber to the window areas of the exterior chamber separate the two chambers. The detection chamber is pumped by a turbomolecular pump mounted upside down on top of the chamber, and the source chamber is pumped by

a diffusion pump (Varian, VHS 6) mounted underneath. The two chambers are connected by a homemade skimmer with a diameter of 1 mm.

Details of the LD source are shown in the lower portion of Figure 3.1. The sample tetracene (Aldrich) was smudged onto a graphite rod by hand, and the rod was mounted tangent to the surface of the pulsed valve. The rod was 5.5 in. in length and 1/8 in. in diameter. It was pressed against the surface of the pulsed valve by two counter-rotating wheels. The pitch of translation of the rod was adjustable by the angle of the two wheels, and the direction of translation was controlled by the sense of rotation. The overall operating time of each rod was imposed by the small diameter of the chamber, and the typical duration for each rod, after a complete round trip, was on the order of 6–8 h. The desorption laser (Spectra Physics GCR 230) at 1064 nm with a pulse energy of ~0.06 mJ/ pulse was focused onto the rod with a lens of 6 in. in focal length. The vapor was seeded in 3 atm of argon and expanded into vacuum through a pulsed valve with an orifice of 1 mm in diameter. With this setup, the internal temperature of the desorbed species was below 30 K, based on the intensity ratio of a hot band and the origin band of *para*-aminobenzoic acid.<sup>33</sup>

The laser systems for the REMPI experiment include a Nd:YAG (yttrium aluminum garnet) (Precision I 8000, Continuum) pumped optical parametric oscillator (OPO) (Panther, Continuum) and a Nd:YAG (Spectra Physics GCR 190) pumped dye laser system (Laser Analytical Systems. LDL 20505). The OPO laser in the 430-450 nm range had a pulse energy of 2 mJ/ pulse. The ionization laser in

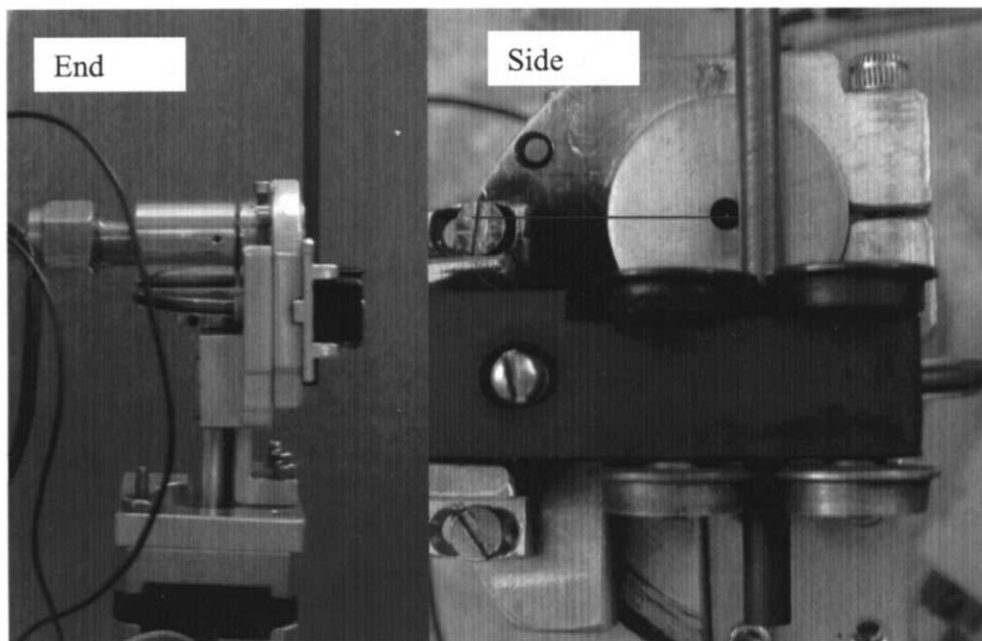
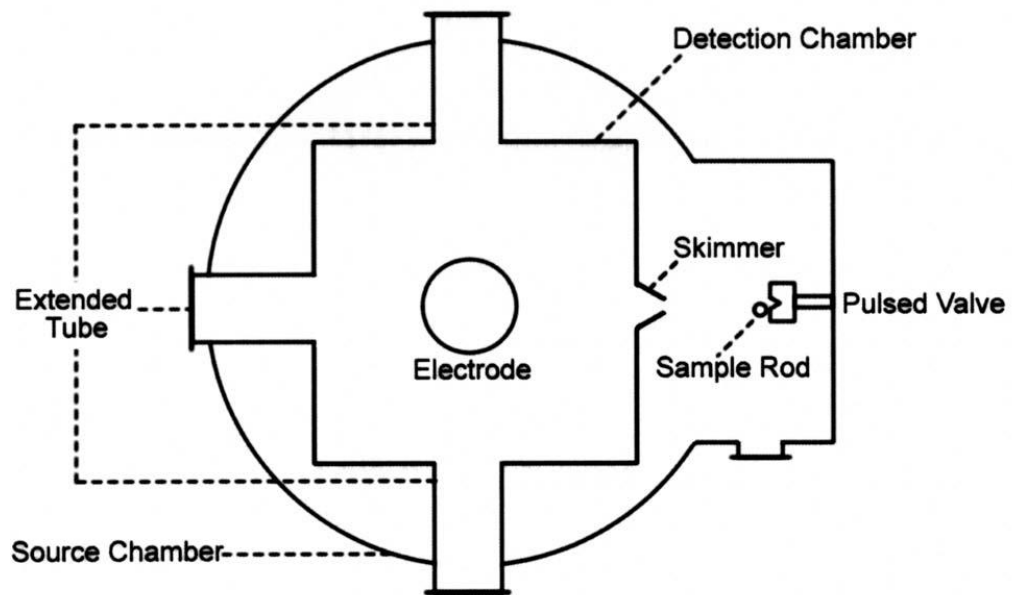


Figure 3.1 Experimental setup showing details of the laser desorption source.

the 293-302 nm range, obtained from the frequency doubled dye laser system, had a pulsed energy of 0.6 mJ.

The absolute wavelength of each laser was calibrated using an iron hollow-cathode lamp filled with neon. The pump laser and ionization laser were set to counterpropagate, and the light path, the flight tube, and the molecular beam were mutually perpendicular. The relative timing among the three laser pulses was controlled by a delay generator (Stanford Research, DG535), and the optimal signal was obtained under temporal overlap between the pump and ionization lasers. In the ZEKE experiment, molecules excited to high Rydberg states were allowed to stay for 1-2  $\mu\text{s}$  in the presence of a spoiling field of  $\sim 2$  V/cm, and ionization and extraction were achieved by a pulsed electric field of  $\sim 18$  V/cm.

In order to assign the observed vibronic structures in both the REMPI and ZEKE spectra, we used the GAUSSIAN 03 suite<sup>34</sup> to optimize the molecular structure and to obtain vibrational frequencies. For the ground state of the neutral ( $S_0$ ) and the cation ( $D_0$ ), density functional theory calculations using the B3LYP functional were performed with the 6-31G+( $d,p$ ) basis set. The excited state ( $S_1$ ) was calculated at the configuration interaction singles (CIS) level using the 6-31G+( $d,p$ ) basis set, and the resulting vibrational frequencies were scaled by a factor of 0.94. No scaling factor for the  $D_0$  state was used.

### 3.4 Result

#### 3.4.1 Two-color 1+1' REMPI spectroscopy

The two-color 1+1' REMPI spectrum of tetracene near the origin of the  $S_1 \leftarrow S_0$  electronic transition is displayed in Figure 3.2. The ionization laser was set at 290 nm and was temporally overlapped with the scanning resonant laser. The spectrum is similar to that reported by Amirav *et al.*<sup>35,36</sup> and the assignment is also in general agreement with that of the report. The intense peak at  $22396 \text{ cm}^{-1}$  is assigned as the origin band, and the other observed vibronic transitions are listed in Table 3.1. Our *ab initio* calculation on the CIS/6-31G+(*d,p*) level, after scaling by a factor of 0.94, agrees with the experimental values reasonably well.

In designating the observed vibrational modes, we have followed the spectroscopic convention by using consecutive numbers in reference to the symmetry species and the frequency in decreasing order. The displacement vectors of the four observed modes are shown in Figure 3.3. Modes 15, 14, and 13 are the longitudinal stretching, transverse waving, and transverse symmetric stretching modes, respectively. They all have  $A_g$  symmetry, and are all IR forbidden but vibronic allowed. Different from the assignment by Amirav *et al.*<sup>35,36</sup> we have another explanation of the third peak at  $464 \text{ cm}^{-1}$ . According to the vibrational selection rule in electronic transitions, only total symmetric modes ( $A_g$ ) and even numbered other modes are allowed. In our calculation, there was only one total

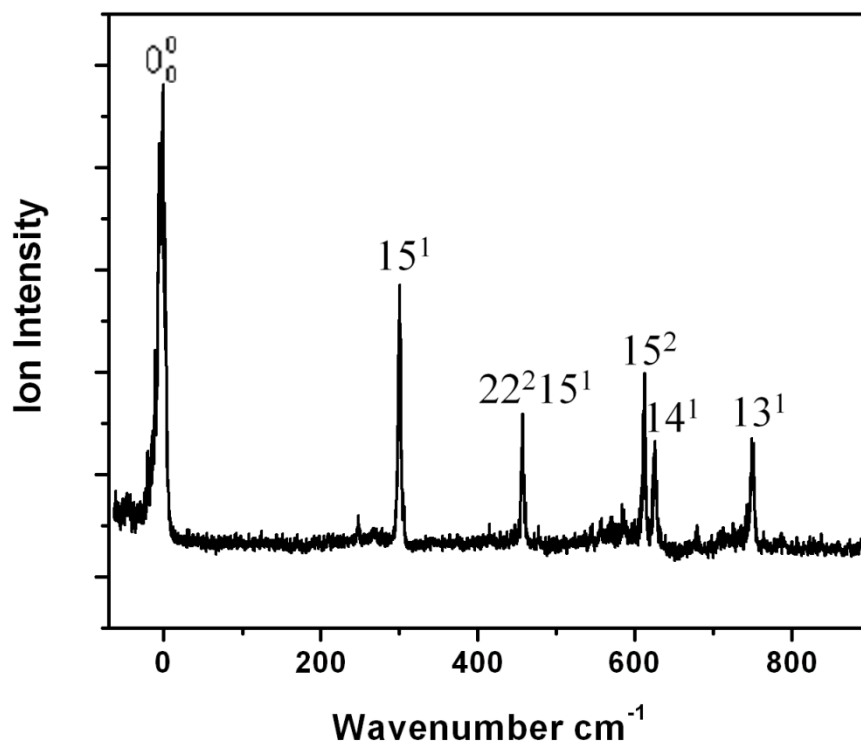


Figure 3.2  $1+1'$  REMPI spectrum of jet-cooled tetracene. The spectrum is shifted by  $22\,396\text{ cm}^{-1}$  (the origin of the  $S_1 \leftarrow S_0$  transition) to emphasize the frequencies of the different vibrational modes of the  $S_1$  state.

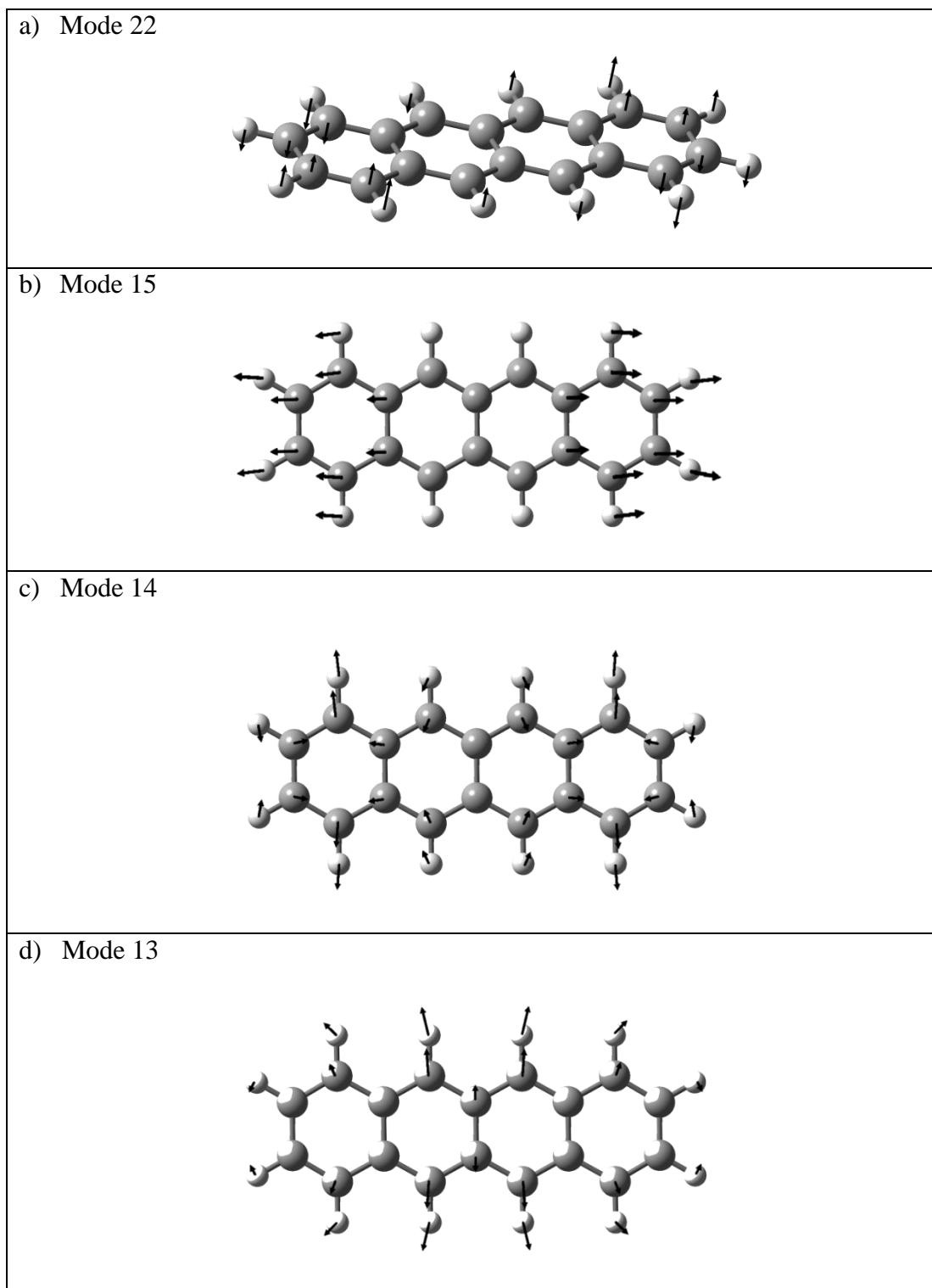


Figure 3.3 Four observed normal modes in the  $S_1$  state of tetracene.

Table 3.1 Observed and calculated vibrational frequencies of the S<sub>1</sub> state of tetracene

Exp	Calc *	Assignment Mode, symmetry
307	312	15 <sup>1</sup> , A <sub>g</sub>
464	480	22 <sup>2</sup> 15 <sup>1</sup> , A <sub>u</sub> <sup>2</sup> A <sub>g</sub>
624	624	15 <sup>2</sup> , A <sub>g</sub>
636	627	14 <sup>1</sup> , A <sub>g</sub>
765	750	13 <sup>1</sup> , A <sub>g</sub>

\* the values include a scaling factor of 0.94

symmetric mode at  $312\text{ cm}^{-1}$  (mode 15) below  $500\text{ cm}^{-1}$ , and among the second harmonics of other low frequency modes, the closest one to  $464\text{ cm}^{-1}$  was at  $537\text{ cm}^{-1}$ . On the other hand, a combination of mode 15 and the second harmonic of mode 22 at  $84\text{ cm}^{-1}$ ,  $A_u$  in symmetry, agrees with the experimental result within  $16\text{ cm}^{-1}$ . This  $A_u$  mode corresponds to an out-of-plane twisting motion. Although not a perfect match, we believe that this assignment of  $22^2 15^1$  is more reasonable than that of mode 76 at  $494\text{ cm}^{-1}$ ,  $B_{3g}$  in symmetry, as proposed by Amirav *et al.*<sup>35,36</sup> Further evidence of this assignment will be discussed in the ZEKE experiment.

### 3.4.2 ZEKE spectroscopy

By scanning the ionization laser while setting the resonant laser at one of the intermediate states identified in the above REMPI experiment, we have obtained pulsed field ionization ZEKE spectra as shown in Figure 3.4. The identity of the intermediate vibrational level for each ZEKE spectrum is marked on the figure by a black dot, while the vibrational assignment of the cation is noted by a superscript “+” for clarity. Table 3.2 summarizes these observations and lists the theoretical values obtained on the B3LYP/6-31G+(*d,p*) level. No scaling factor for the vibrational frequencies of the cation is used in Table 3.2. Limited by the linewidth of the resonant transitions, the uncertainty of the experimental values of the ZEKE spectra is  $7\text{ cm}^{-1}$ .

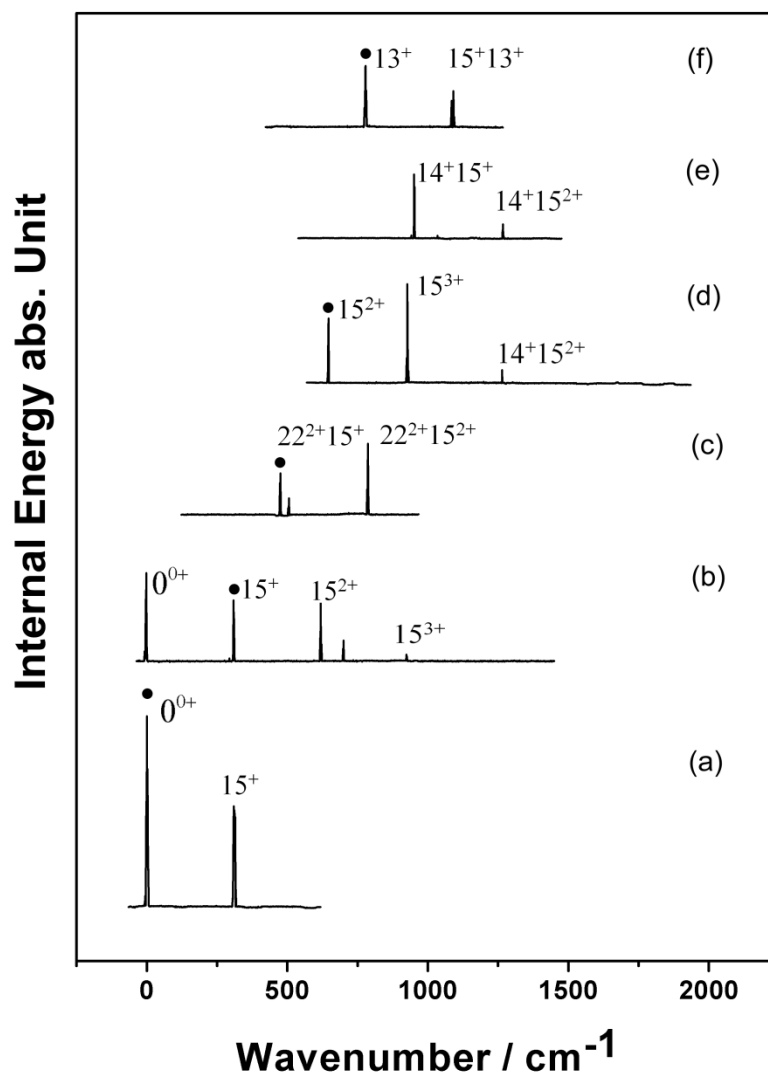


Figure 3.4. Two-color ZEKE spectra of tetracene recorded via the following vibrational levels of the  $S_1$  state as intermediate states: (a)  $0_0^0$ , (b)  $15^1$ , (c)  $22^2 15^1$ , (d)  $15^2$ , (e)  $14^1$ , and (f)  $13^1$ . The energy in the abscissa is relative to the ionization threshold at  $55918 \text{ cm}^{-1}$ . The assignment in the figure refers to the vibrational levels of the cation, and the corresponding vibrational level of the intermediate state is labeled by a black dot in each panel.

Table 3.2. Observed and calculated vibrational frequencies and assignments in the ZEKE spectra of tetracene.

$0_0^0$	$15_0^1$	$22_0^2 15_0^1$	$15_0^2$	$14_0^1$	$13_0^1$	Cal	assignment
0							$0^{0+}$
311	310					316	$15^+$
		476				495	$22^{2+} 15^+$
	620		634			628	$15^{2+}$
					777	764	$13^+$
		786					$22^{2+} 15^{2+}$
	924		922				$15^{3+}$
				951			$14^+ 15^+$
					1091		$13^+ 15^+$
			1264	1267			$14^+ 15^{2+}$

In general, the observed vibrational modes of the cation are in-plane deformations of the ribbon, and the displacement vectors of the observed modes of the cation are similar to those of the  $S_1$  state (Figure 3.3). From trace 4a recorded via the origin of the  $S_1$  state, the adiabatic ionization potential is determined to be  $55918 \pm 7 \text{ cm}^{-1}$ , taking into account the shift induced by the delayed electric field. This value is very close to the reported ionization threshold of 6.94 eV but it has a much higher precision.<sup>37</sup> The ZEKE spectra are sparse, but they are not always dominated by the vibrational level of the intermediate state. In particular, mode 15 seems to show up in all spectra, regardless of the vibrational excitation of the intermediate state.

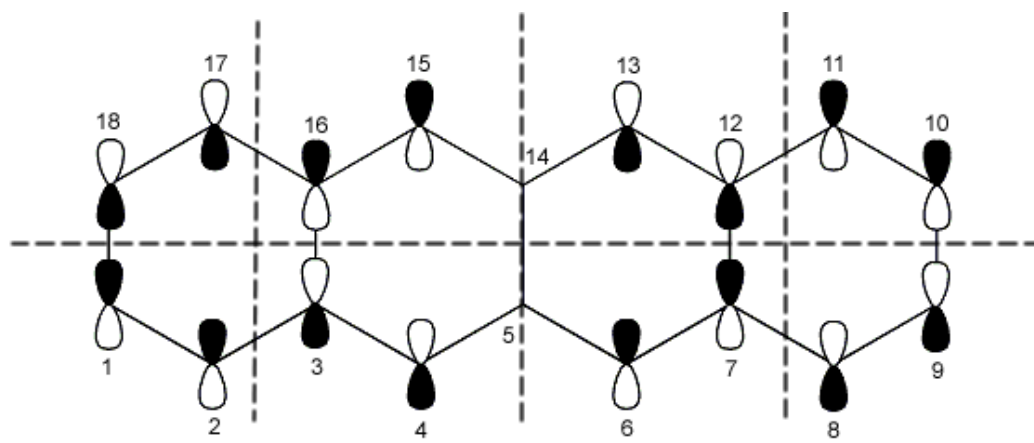
Although most of the observed vibrational transitions are easily assigned in comparison with the theoretical values, the near degeneracy of mode 14 and the second harmonic of mode 15 presents a problem (traces d and e of Figure 3.4). The current assignment agrees with the intensity pattern of trace b, where ionization via a level  $n$  of mode 15 in the  $S_1$  state produces vibrational excitations in the  $D_0$  state of both the  $n$  and  $n+1$  levels. In trace e, however, ionization via mode 14 only results in combination bands with mode 15. We interpret this result by referencing the REMPI spectrum of Figure 3.2. The close proximity of  $15^2$  and 14 in the REMPI spectrum could be an indication of intensity borrowing of mode 14 from  $15^2$ . Consequently, only combination bands with mode 15 can have sufficient intensity in the ZEKE spectrum.

The corresponding ZEKE spectrum from the  $22^215^1$  level of the  $S_I$  state, trace c, contains two major features separated by  $310\text{ cm}^{-1}$ . It is therefore definitive that there is an additional vibrational quanta in mode 15 for the second feature. The theoretical value for the combination band of  $22^215^1$  of the cation is at  $495\text{ cm}^{-1}$ , corresponding to a deviation of  $19\text{ cm}^{-1}$  from the experimental value. This deviation is about the same as that in the  $S_I$  state. Similar to the  $S_I$  state, the cationic state has no total symmetric mode  $A_g$  nor second harmonics of any mode near  $476\text{ cm}^{-1}$ , although three vibrational modes with  $B_{3u}$ ,  $B_{1g}$ , and  $B_{3g}$  symmetry species are all within  $20\text{ cm}^{-1}$  of the experimental value. Given the intensity of these bands and the general trend in vibrational propensity of ZEKE, we hence believe that the best assignment for both the initial ( $S_I$ ) and final ( $D_0$ ) vibrational states is a combination band of  $22^215^1$ .

### 3.5 Discussion

To understand the vibrational modes activated upon electronic excitation and ionization, in Table 3.3, we list the geometric parameters from our calculation for all three electronic states, and the numbering scheme can be found in Figure 3.5. These parameters are similar to those reported by Pathak and Rastogi<sup>38</sup> for the ground ( $S_0$ ) and the first excited electronic state ( $S_I$ ). In general, the length of the ribbon does not exhibit any substantial change upon electronic excitation or ionization, but the width of the ribbon first contracts upon excitation but later

HOMO:



LUMO:

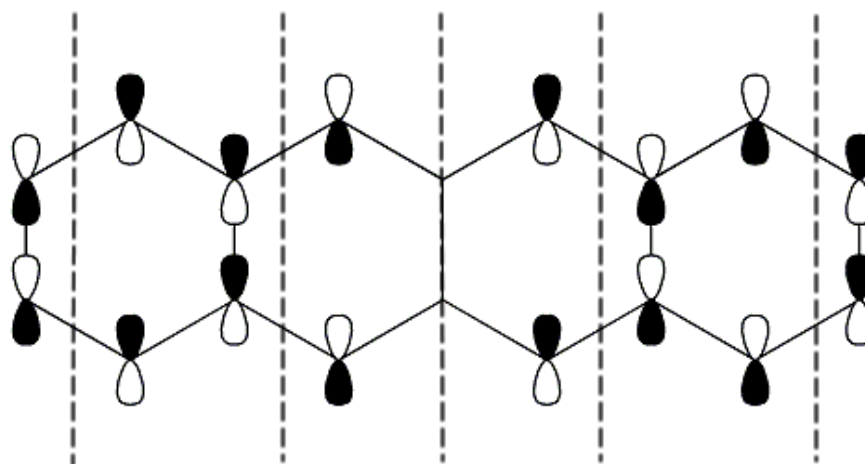


Figure 3.5 The HOMO and LUMO of tetracene. The dashed lines mark the nodal planes.

Table 3.3. Molecular geometry parameters of tetracene in the  $S_0$ ,  $S_1$  and  $D_0$  state

	$S_0$	$S_1$	$D_0$
Bond length (Å)			
C1 – C2	1.369	1.383	1.384
C2 – C3	1.435	1.407	1.420
C3 – C4	1.394	1.415	1.407
C4 – C5	1.412	1.397	1.410
C1 – C18	1.432	1.401	1.415
C3 – C16	1.453	1.432	1.446
C5 – C14	1.453	1.454	1.452
Distance (Å)			
C1 – C9	9.787	9.793	9.786
C2 – C17	2.821	2.788	2.821
(C4 – C15)	(2.815)	(2.793)	(2.819)

extends back to its original value. Internal reorganization of the molecular frame seems more dramatic; while the transverse bonds of C1–C2 and C3–C4 expand, the bonds C2–C3 and C4–C5 shrink upon both excitation and ionization. Those changes are in accord with the activation of mode 15, mode 14, and mode 13 in the spectrum.

Interestingly, these changes in bond length and the resulting vibrational activity can be qualitatively explained from a simple Hückle calculation. Figure 3.5 shows the lowest unoccupied molecular orbital (LUMO) and the highest occupied molecular orbital (HOMO) from our simple Hückle calculation. A major difference between the two orbitals is the disappearance of the horizontal nodal plane in the LUMO. In the  $S_I \leftarrow S_0$  transition, one electron is excited from the HOMO to the LUMO. We thus expect that the width of the ribbon should decrease due to increased bonding along this short axis. This change agrees well with the high level calculation result listed in Table 3.3, where the bond lengths of C1–C18, C3–C16, and C5–C14 decrease from  $S_0$  to  $S_I$ . In addition, the nodal plane between C2 and C3 in the HOMO bifurcates to the C1–C2 and C3–C4 regions, hence the bond length of C2–C3 decreases and those of C1–C2 and C3–C4 increase in the  $S_I$  state. In total, there are three vertical nodal planes in the HOMO and five vertical nodal planes in the LUMO, and this result alludes to an elongation effect of the molecular long axis.

These changes in the molecular frame induce corresponding vibrational activities in the REMPI spectrum. The three in-plane vibrational modes observed

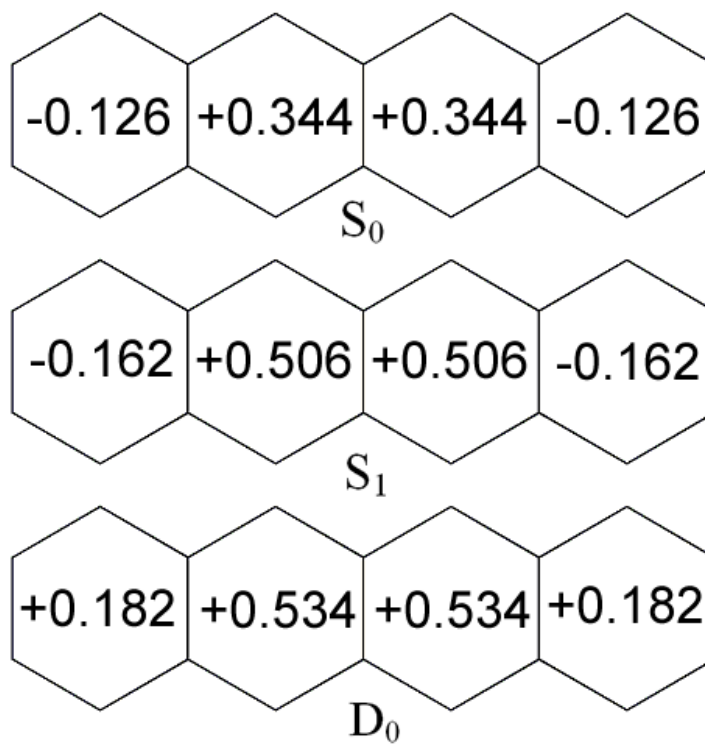


Figure 3.6 Charge distributions on rings of three states of tetracene spectra.

in the 1+1' REMPI spectrum of Figure 3.2 are directly reflective of the changes in nodal planes. In particular, mode 15 is activated due to the increase in the number of vertical nodal planes in the LUMO, while mode 14 and mode 13 are activated due to the loss of the horizontal nodal plane. Mode 22 is out-of-plane twisting, and the stationary carbon atoms C5 and C14 are located on the preserved nodal plane between the HOMO and the LUMO.

Interestingly, further ionization does not exaggerate this change in the molecular frame; rather, the cation is more similar to the neutral ground state than to the electronically excited state. Ionization from  $S_1$  involves removal of the LUMO electron, and hence the antibonding effect along the ribbon and the bonding effect across the ribbon from the LUMO are both eliminated. It is therefore reasonable for the geometry of the cation to relax back to that of the  $S_0$  state. The differences in the molecular frame between  $S_1$  and  $D_0$  contribute to the loss in propensity in the ZEKE different from the results of substituted benzene derivatives reported in our previous work,<sup>39-42</sup> the spectra in Figure 3.4 are not dominated by a single vibrational band of the cation.

To elucidate the location of the positive charge upon ionization, Figure 3.6 shows the charge distributions on the two sets of unique rings from *ab initio* and density functional calculations. For all three electronic states, the internal carbon atoms that are not attached to any hydrogen atoms have partial positive charges, while the rest of the carbon atoms have partial negative charges. If we consider the complete ring structure, the positive charge of the cation is mostly located on the

two center rings. This result indicates that the two sets of unique rings are not equivalent in aromaticity, as discussed by Bultinck *et al.*<sup>43</sup> The authors have pointed out that aromaticity in linear polyacenes decreases from the outer to the inner rings. This decrease in aromaticity follows Clar's rule, and the inner rings are hence more reactive than the outer rings.

Among the observed modes, with a scaling factor of 0.94 for  $S_I$  (Table 3.1) and no scaling for  $D_0$  (Table 3.2), the theoretical values are too big for the low frequency modes ( $500\text{ cm}^{-1}$ ), and too small for the high frequency modes ( $500\text{ cm}^{-1}$ ). The amount of deviation, however, is not predictable *a priori*. This conclusion exemplifies the need for both theoretical and experimental efforts in modeling vibrational spectroscopy and in astrophysical fingerprint matching. The resolution of modern day space missions, for example, the Herschel Space Observatory, can be much higher than  $1\text{ cm}^{-1}$  in the FIR region. Assignment of the observed features from these space missions will require high resolution laboratory data and high precision theoretical predictions.

Dictated by the vibrational selection rule, only even numbered harmonics of IR active modes and total symmetric modes ( $A_g$ , IR inactive) are observable in ZEKE. The resulting sparse spectrum greatly simplifies vibrational assignment for large sized molecules. This is because even for tetracene, the number of FIR modes is  $\sim 40$ ,<sup>27</sup> and information on frequency alone is insufficient for a definitive assignment. From Table 3.2 and Figure 3.4, all observed modes in tetracene from this work are IR inactive. Although these results are not directly beneficial to

spectroscopic assignments of astrophysical observations, ZEKE experiments provide a calibration standard for theoretical calculation and refinement, and they provide necessary information for modeling of the energy dissipation and distribution in astrophysical objects. On the other hand, there should be eight IR active modes in the FIR region that have non-negligible intensities based on our calculation. Activation of these modes from ZEKE requires preparation of initial vibrational states. However, direct FIR excitation requires intense terahertz light sources, which is yet to be commercially available.<sup>25</sup> Other approaches, for example, complexation with small molecules such as H<sub>2</sub>O and NH<sub>3</sub>, might help us to circumvent this problem.

### 3.6 Conclusion

Spectroscopic properties of the electronically excited and ionic states of tetracene have been studied using 1+1' two-color REMPI and two-color ZEKE spectroscopy. This is the first time that ZEKE spectroscopy has been performed in combination with a laser desorption source. With the "chamber in a chamber" design, the density of molecules and hence the density of prompt ions in the ionization region are proven sufficiently high for stabilization of high Rydberg states. This condition is critical to the success of ZEKE spectroscopy. This work thus expands the application of ZEKE to studies of any nonvolatile species. In addition, ZEKE spectroscopy is governed by a different set of selection rules from vibrational single photon processes, and it is particularly sensitive to low frequency

modes of the molecular frame. Since vibrational spectroscopy in the far IR and submillimeter region is considered fingerprint regions for species identification in the outer space, ZEKE spectroscopy has the potential of becoming an important tool in astrophysics. However, fine-tuning of the experimental technique to access a large number of IR active modes is still needed.

Tetracene is a rigid molecule, and upon electronic excitation and ionization, the small change in the molecular frame only activates a limited number of vibrational modes. Interestingly, these modes can be directly related to the addition or elimination of nodal planes in the LUMO and HOMO based on a simple Hückle calculation. Most of the observed modes are in-plane stretching along the longitudinal or transverse axes of the molecule. From the comparison with theoretical values, the deviation between experiment and theory is on the order of  $20 \text{ cm}^{-1}$ .

### **3.7 Acknowledgments**

We are deeply indebted to Dr. Farid Salama for his unwavering support of this project. Our talented machinist, Ted Hinke, has made this work possible, with his many ingenious designs and modifications of the experimental apparatus. This work is supported by the National Science Foundation, Division of Chemistry. Acknowledgment is made to the Donors of The Petroleum Research Fund, administered by the American Chemical Society, for partial support of this research.

### 3.8 References

- (1) A. Li, "PAHs in comets: An overview," ESO Astrophys. Symp. (in press).
- (2) S. G. Wakeham, C. Schaffner, and W. Giger. *Geochim. Cosmochim. Acta.*, **44**, 415 (1980).
- (3) E. L. Shock and M. D. Schulte, *Nature* (London) **343**, 728 (1990).
- (4) E. Peeters, L. J. Allamandola, D. M. Hudgins, S. Hony, and A. G. G. M. Tielens, *Astron. Soc. Pac. Conf. Ser.*, **309**, 141 (2004).
- (5) G. Mallocci, G. Mulas, and P. Benvenuti, *Astron. Astrophys.*, **410**, 623 (2003).
- (6) G. Mulas, G. Mallocci, and P. Benvenuti, *Astron. Astrophys.*, **410**, 639 (2003).
- (7) G. Mulas, G. Mallocci, C. Joblin, and D. Toubanc, *Astron. Astrophys.*, **456**, 161 (2006).
- (8) K. Zhang, B. Guo, P. Colarusso, and P. F. Bernath, *Science* **274**, 582 (1996).
- (9) S. R. Langhoff, *J. Phys. Chem.*, **100**, 2819 (1996).
- (10) B. T. Draine and A. Li, *Astrophys. J.*, **657**, 810 (2007).
- (11) A. Li and B. T. Draine, *Astrophys. J.*, **576**, 762 (2002).
- (12) B. T. Draine and A. Li, *Astrophys. J.*, **551**, 807 (2001).
- (13) A. Li and B. T. Draine, *Astrophys. J.*, **554**, 778 (2001).
- (14) D. M. Hudgins and S. A. Sandford, *J. Phys. Chem. A*, **102**, 353 (1998).
- (15) D. M. Hudgins and S. A. Sandford, *J. Phys. Chem. A*, **102**, 344 (1998)
- (16) D. M. Hudgins and S. A. Sandford, *J. Phys. Chem. A*, **102**, 329 (1998)
- (17) R. Ruiterkamp, T. Halasinski, F. Salama, B. H. Foing, L. J. Allamandola, W. Schmidt, and P. Ehrenfreund, *Astron. Astrophys.*, **390**, 1153 (2002)
- (18) D. M. Hudgins, C. W. Bauschlicher, Jr., L. J. Allamandola, and J. C. Fetzer, *J. Phys. Chem. A*, **104**, 3655 (2000)
- (19) D. M. Hudgins, S. A. Sandford, and L. J. Allamandola, *J. Phys. Chem.*, **98**, 4243 (1994)
- (20) D. M. Hudgins and L. J. Allamandola, *J. Phys. Chem.*, **99**, 8978 (1995)
- (21) D. M. Hudgins and L. J. Allamandola, *J. Phys. Chem.*, **99**, 3033 (1995)
- (22) D. M. Hudgins and L. J. Allamandola, *J. Phys. Chem.*, A **101**, 3472 (1997)
- (23) L. Biennier and L. J. Allamandola, *J. Chem. Phys.*, **118**, 7863 (2003)
- (24) J. Oomens, A. G. G. M. Tielens, B. G. Sartakov, G. von Helden, and G. Meijer, *Astrophys. J.*, **591**, 968 (2003)
- (25) P. Chen, J. C. Pearson, H. M. Pickett, S. Matsuura, and G. A. Blake, *J. Mol. Spectrosc.*, **236**, 116 (2006)
- (26) O. Pirali, N. T. Van-Oanh, P. Parneix, M. Vervloet, and P. Brechignac, *Phys. Chem. Chem. Phys.*, **8**, 3707 (2006)
- (27) G. Mallocci, C. Joblin, G. Mulas, D. Toubanc, and I. Porceddu, *Chem. Phys.*, **332**, 353 (2007)
- (28) E. Nir, K. Kleinermanns, and M. S. de Vries, *Nature* (London) **408**, 949 (2000)

- (29) M. Dey, J. Grotemeyer, and E. W. Schlag, *Z. Naturforsch., A: Phys. Sci.* **49**, 776 (1994)
- (30) K. Muller-dethlefs and E. W. Schlag, *Annu. Rev. Phys. Chem.*, **42**, 109 (1991)
- (31) M. Mons, I. Dimicoli, F. Piuzzi, B. Tardivel, and M. Elhanine, *J. Phys. Chem. A*, **106**, 5088 (2002)
- (32) E. W. Schlag, *ZEKE Spectroscopy* Cambridge University Press, Cambridge, (1998)
- (33) G. Meijer, M. S. de Vries, H. E. Hunziker, and H. R. Wendt, *J. Chem. Phys.*, **92**, 7625 (1990)
- (34) M. J. Frisch, G. W. Trucks, H. B. Schlegel *et al.*, GAUSSIAN 03, Revision B.05, Gaussian, Inc., Pittsburgh, PA, 2003.
- (35) A. Amirav, U. Even, and J. Jortner, *J. Chem. Phys.*, **71**, 2319 (1979).
- (36) A. Amirav, U. Even, and J. Jortner, *J. Chem. Phys.*, **75**, 3770 (1981).
- (37) H. Kuroda, *Nature* (London) **201**, 1214 (1964).
- (38) A. Pathak and S. Rastogi, *Chem. Phys.*, **313**, 133 (2005).
- (39) Y. G. He, C. Y. Wu, and W. Kong, *J. Chem. Phys.*, **121**, 8321 (2004).
- (40) Y. G. He, C. Y. Wu, and W. Kong, *Chem. Phys. Lett.*, **391**, 38 (2004).
- (41) Y. G. He, C. Y. Wu, and W. Kong, *J. Chem. Phys.*, **121**, 3533 (2004).
- (42) C. Y. Wu, Y. G. He, and W. Kong, *Chem. Phys. Lett.*, **398**, 351 (2004).
- (43) P. Bultinck, R. Ponec, and R. Carbo-Dorca, *J. Comput. Chem.*, **28**, 152 (2006).

**Far-Infrared Spectroscopy of Cationic Polycyclic Aromatic Hydrocarbons:  
Zero Kinetic Energy Photoelectron Spectroscopy of Pentacene Vaporized  
from Laser Desorption**

Jie Zhang<sup>1</sup>, Fangyuan Han<sup>1</sup>, Linsen Pei<sup>1</sup>, Wei Kong<sup>1\*</sup>, and Aigen Li<sup>2</sup>

1 Department of Chemistry, Oregon State University, Corvallis, OR 97331, USA

2 Department of Physics and Astronomy, University of Missouri, Columbia, MO

65211, USA

The Astrophysical Journal  
Department of Physics and Astronomy  
McMaster University  
1280 Main Street West, GSB-118C  
Hamilton, Ontario L8S 4K1, Canada

**2010** 715 485 – 492

---

\* To whom correspondence should be addressed.  
Fax: 541-737-2062. E-mail: wei.kong@oregonstate.edu

## **Chapter 4 Far-Infrared Spectroscopy of Cationic Polycyclic Aromatic Hydrocarbons: Zero Kinetic Energy Photoelectron Spectroscopy of Pentacene Vaporized from Laser Desorption**

### **4.1 Abstract**

The distinctive set of infrared (IR) emission bands at 3.3, 6.2, 7.7, 8.6, and 11.3  $\mu\text{m}$  are ubiquitously seen in a wide variety of astrophysical environments. They are generally attributed to polycyclic aromatic hydrocarbon (PAH) molecules. However, not a single PAH species has yet been identified in space as the mid-IR vibrational bands are mostly representative of functional groups and thus do not allow one to fingerprint individual PAH molecules. In contrast, the far-IR (FIR) bands are sensitive to the skeletal characteristics of a molecule, hence they are important for chemical identification of unknown species. With an aim to offer laboratory astrophysical data for the Herschel Space Observatory, Stratospheric Observatory for Infrared Astronomy, and similar future space missions, in this work we report neutral and cation FIR spectroscopy of pentacene ( $\text{C}_{22}\text{H}_{14}$ ), a five-ring PAH molecule. We report three IR active modes of cationic pentacene at 53.3, 84.8 and 266  $\mu\text{m}$  that may be detectable by space missions such as the SAFARI instrument on board SPICA.

In the experiment, pentacene is vaporized from a laser desorption source and cooled by a supersonic argon beam. We have obtained results from two-color resonantly enhanced multiphoton ionization and two-color zero kinetic energy

photoelectron spectroscopy (ZEKE). Several skeletal vibrational modes of the first electronically excited state of the neutral species and those of the cation are assigned, with the aid of *ab initio* and density functional calculations. Although ZEKE is governed by the Franck-Condon principle different from direct IR absorption or emission, vibronic coupling in the long ribbon-like molecule results in the observation of a few IR active modes. Within the experimental resolution of  $\sim 7 \text{ cm}^{-1}$ , the frequency values from our calculation agree with the experiment for the cation, but differ for the electronically excited intermediate state. Consequently, modeling of the intensity distribution is difficult and may require explicit inclusion of vibronic interactions.

## 4.2 Introduction

Polycyclic aromatic hydrocarbons (PAH) reveal their presence in the interstellar medium (ISM) by a distinctive set of emission features at 3.3, 6.2, 7.7, 8.6, and 11.3  $\mu\text{m}$  (which are also collectively known as the “Unidentified Infrared” [UIR] emission bands).<sup>i</sup> Since their first detection in the planetary nebulae NGC

---

<sup>i</sup> These “UIR” emission features are now generally identified as vibrational modes of PAHs<sup>12,13</sup>: C-H stretching mode (3.3  $\mu\text{m}$ ), C-C stretching modes (6.2, 7.7  $\mu\text{m}$ ), C-H in-plane bending mode (8.6  $\mu\text{m}$ ), and C-H out-of-plane bending mode (11.3  $\mu\text{m}$ ). Other C-H out-of-plane bending modes at 11.9, 12.7 and 13.6  $\mu\text{m}$  have also been detected. The wavelengths of the C-H out-of-plane bending modes depend on the number of neighboring H atoms: 11.3  $\mu\text{m}$  for solo-CH (no adjacent H atom), 11.9  $\mu\text{m}$  for duet-CH (two adjacent H atoms), 12.7  $\mu\text{m}$  for trio-CH (three adjacent H atoms), and 13.6  $\mu\text{m}$  for

7027 and BD+30 3639,<sup>1</sup> PAHs have been observed in a wide range of Galactic and extragalactic regions.<sup>2</sup> Neutral and ionic PAHs have long been suggested to be possible carriers of the 2175Å interstellar extinction bump<sup>3-5</sup> and the mysterious diffuse interstellar bands (DIBs)<sup>6</sup>. PAHs are the dominant energy source for the interstellar gas as they provide photoelectrons which heat the gas.<sup>7</sup> They are also potentially related to the origin of life via the formation of primitive organic molecules including amino acids in the pre-DNA.<sup>8-11</sup>

Identification of the exact molecular formulas of astronomical PAHs unfortunately has been ineffective so far,<sup>ii</sup> largely because of the spectral range issue: the 3.3-17.4µm mid-infrared (MIR) bands are mostly representative of functional groups, not the molecular frame.<sup>iii</sup> In contrast, the far infrared (FIR) bands are considered sensitive to the skeletal characteristics of a molecule. Hence

---

quartet-CH (four adjacent H atoms). Other prominent features are the C-C-C bending modes at 16.4 µm<sup>14</sup> and 17.4 µm<sup>15-17</sup>.

<sup>ii</sup> Several small PAHs [naphthalene (C<sub>10</sub>H<sub>8</sub>), phenanthrene (C<sub>14</sub>H<sub>10</sub>), pyrene (C<sub>20</sub>H<sub>12</sub>), perylene (C<sub>16</sub>H<sub>10</sub>)] have been found in the *Stardust* samples collected from comet Wild,<sup>21</sup> and in interplanetary dust particles possibly of cometary origin.<sup>22</sup> Although Spencer & Zare<sup>23</sup> argued that some of the low-mass PAHs seen diffusely on the surfaces along the impact track may be due to impact conversion of aerogel carbon, the majority of the PAHs in the *Stardust* samples should be of cometary origin.<sup>24</sup>

<sup>iii</sup> In astronomical modeling, astronomers usually take an empirical approach by constructing “astro-PAH” absorption properties that are consistent with spectroscopic observations of PAH emission in various astrophysical environments<sup>4,25-28</sup>. The resulting “astro-PAH” absorption cross sections, although generally consistent with laboratory data (e.g. see Fig. 2 of ref 27), do not represent any specific material, but approximate the actual absorption properties of the PAH mixture in astrophysical regions.

they contain specific fingerprint information on the identity of a PAH molecule and could lead to the identification of individual PAHs.<sup>18-20</sup>

One mission of the *Stratospheric Observatory for Infrared Astronomy* (SOFIA) and the *Herschel Space Observatory* is thus to target the FIR and submillimeter (submm) wavelength region of the ISM. The goal is to answer the questions: “*What is the molecular makeup of the ISM and how does that relate to the origin of life?*” To assist with data interpretations of these missions, laboratory experimental data of PAHs in the same spectral region are in urgent need.

Experiments in the FIR are typically challenging due to the lack of adequate light sources and sensitive detectors. Moreover, spectroscopy of ions and more so of ions of non-volatile species, is further hindered by the low achievable particle density. We have recently succeeded in combining the laser desorption (LD) technique with the zero kinetic energy photoelectron (ZEKE) spectroscopy technique (see §4.2 for a brief description; for more details see Zhang et al.<sup>29</sup>). With this combination, albeit still challenging, we offer an alternative approach in solving the issues of FIR spectroscopy of non-volatile cations.

There have been several reports of the ZEKE spectroscopy of small PAHs including naphthalene ( $C_{10}H_8$ ), anthracene ( $C_{14}H_{10}$ ), and tetracene ( $C_{18}H_{12}$ )<sup>29-31</sup>. In this paper, we report in §4.4 the ZEKE spectroscopy in the FIR of pentacene ( $C_{22}H_{14}$ ), a five-ring PAH molecule. Detailed spectroscopic analysis for the vibrational levels of the first electronically excited state ( $S_1$ ) and the ground

cationic state ( $D_0$ ) will be discussed, with the assistance of *ab initio* and density functional calculations (§4.6). Structural changes due to electronic excitation and ionization will be elucidated from the observed active vibrational modes. In particular, we report several IR active modes that are important for astronomy (§4.6.4). Comparisons between the observed modes of pentacene and smaller catacondensed PAHs, particularly tetracene, will be discussed. Readers who are interested only in the resulting FIR spectra may wish to proceed directly to §4.6.4.

### 4.3 The ZEKE Technique

The ZEKE technique has been introduced to the gas phase spectroscopy community for more than two decades.<sup>32</sup> Typically in a ZEKE experiment, a tunable laser (or lasers in a multiphoton excitation scheme) excites valence electrons into high Rydberg states just below the ionization threshold of a selected vibronic state of the cation. These Rydberg state electrons can orbit around a cationic core for a long time (micro to milliseconds), allowing prompt electrons directly ionized from the laser to escape the detection region. With a delayed electric pulse, the Rydberg state species can then be field ionized to generate ZEKE electrons. Thus only when the excitation energy is close to a particular vibronic state of the cation can Rydberg states exist and ZEKE electrons be detected.

The spectral resolution of ZEKE is determined by the delayed pulsed electric field and the excitation laser, not affected by the discrimination ability of threshold electrons as in typical threshold photoelectron spectroscopy experiments.<sup>33</sup> Usually in the wavenumber range, resolutions of ZEKE experiments on the order of  $\sim 100$  kHz ( $3 \times 10^{-6}$  cm<sup>-1</sup>) are achievable with careful controls of experimental conditions and narrow linewidth lasers.<sup>32,34,35</sup>

The high Rydberg states have the same vibronic properties as those of the corresponding cation, therefore ZEKE is ideal for the study of vibrational spectroscopy of cations. In addition, Rydberg states are longer lived when they are associated with lower vibronic states of the cation, which makes ZEKE particularly suitable for studies of lower frequency vibrational modes. Thus by detecting pulsed field ionized electrons in ZEKE spectroscopy, we can avoid the detector problem in FIR and submm spectroscopy.

There have been several reports of ZEKE spectroscopy of small PAHs including naphthalene (C<sub>10</sub>H<sub>8</sub>), anthracene (C<sub>14</sub>H<sub>10</sub>), and tetracene (C<sub>18</sub>H<sub>12</sub>).<sup>29-31</sup> The difficulty in vaporizing large PAHs has severely limited further efforts. Fortunately, laser desorption has recently resolved the issue and offered internal cooling of the neutral species.<sup>36,37</sup>

In our LD setup, a low power pulsed IR laser is used for vaporization of the solid sample. Due to the fast efficient heating of the pulsed laser, only neutral intact molecules are ejected into the gas phase. The neutral molecules are entrained in a

supersonic jet of argon for rotational and vibrational cooling. The cold isolated neutral species enters into the detection region where they can be first pumped to an electronically excited state by an ultraviolet (UV) laser then ionized by a scanning second laser. This *resonantly enhanced multiphoton ionization* (REMPI) scheme ultimately generates cations in different vibrational levels. Thus by using tunable UV lasers in ZEKE via resonant excitation and ionization, we bypass the light source problem in typical FIR and submm experiments. The combination of ZEKE and LD has been demonstrated in our studies of tetracene.<sup>29</sup>

#### **4.4 Experimental Setup**

The experimental apparatus has been described in detail in a previous publication.<sup>29</sup> Briefly, it consists of a differentially pumped high vacuum system with a laser desorption source and a time of flight mass spectrometer (TOF-MS), which could be converted into a pulsed field ionization (PFI) zero kinetic energy photoelectron spectrometer. The pentacene sample (Aldrich) was smudged onto a graphite rod by hand. The desorption laser (Spectra Physics GCR 230) at 1064 nm with a pulse energy of ~0.1 mJ/pulse was focused onto the rod by a lens with a focal length of 6". The desorbed pentacene vapor was entrained in a supersonic expansion of argon with a stagnation pressure of 3 atm and a pulsed nozzle of 1 mm in diameter. The laser systems for the REMPI experiment included a Nd:YAG (Precision II 8000, Continuum) pumped optical parametric oscillator (OPO,

Panther, Continuum) and a Nd:YAG (Spectra Physics GCR 190) pumped dye laser (Laser Analytical Systems, LDL 20505). The OPO laser in the 523 - 538 nm range had a pulse energy of  $\sim 1.5$  mJ/pulse. The ionization laser in the 280 - 290 nm range, obtained from the frequency doubled dye laser system, had a pulse energy of  $\sim 0.8$  mJ/pulse. The absolute wavelength of each laser was calibrated using an iron hollow-cathode lamp filled with neon. The pump laser and ionization laser were set to counter propagate, and the light path, the flight tube, and the molecular beam were mutually perpendicular. The relative timing among the three laser pulses was controlled by two delay generators (Stanford Research, DG535), and the optimal signal was obtained under temporal overlap between the pump and ionization lasers. In the ZEKE experiment, molecules excited to high Rydberg states stayed in the excitation region for 1 - 2  $\mu$ s in the presence of a constant DC spoiling field of  $\sim 1$  V/cm. Further ionization and extraction was achieved by a pulsed electric field of  $\sim 8$  V/cm. The DC spoiling field in the ionization region was to remove prompt electrons generated from direct photoionization.

Gaussian 03 suite was used to optimize the molecular structure and to obtain vibrational frequencies for assignment of the observed vibronic structures from REMPI and ZEKE.<sup>38</sup> For the ground state of the neutral ( $S_0$ ) and the cationic state  $D_0$ , density functional theory (DFT) calculations using the B3LYP functional were performed with the 6-31G+ (dp) basis set. The excited state  $S_1$  was calculated at the CIS level using the 6-31G+ (dp) basis set. Due to the fact that vibrational

frequencies generated by *ab initio* calculations are usually too high, a general practice is to use a scaling factor to match the experimental results.<sup>39</sup> For the  $S_1$  state of pentacene, we used a scaling factor of 0.92, but no scaling factor was necessary for the  $D_0$  state from our DFT calculation.

## 4.5 Results

### 4.5.1 Two-color 1+1' REMPI spectrum

The two-color 1+1' REMPI spectrum of pentacene near the origin of the  $S_1 \leftarrow S_0$  electronic transition is displayed in Figure 4.1. The ionization laser was set at 280 nm and was temporally overlapped with the scanning resonant laser. Since one photon from each laser was used, and the overall process involved the concurrent excitation of both lasers, this multiphoton process is typically designated as 1+1' REMPI in laser spectroscopy. The intense peak at  $18657 \text{ cm}^{-1}$  is assigned as the origin band, and the other observed vibronic transitions are listed in Table 4.1. The labeling of each vibrational mode is based on spectroscopic conventions, i. e. by using consecutive numbers in reference to the symmetry species and the frequency in decreasing order. The calculated frequencies for the  $S_1$  state, after scaling by a factor of 0.92, agree with the observed results within  $22 \text{ cm}^{-1}$ .

Vibronic activities in REMPI are controlled by the Franck-Condon principle and affected by vibronic coupling. For linear polyacenes, all vibrational levels of

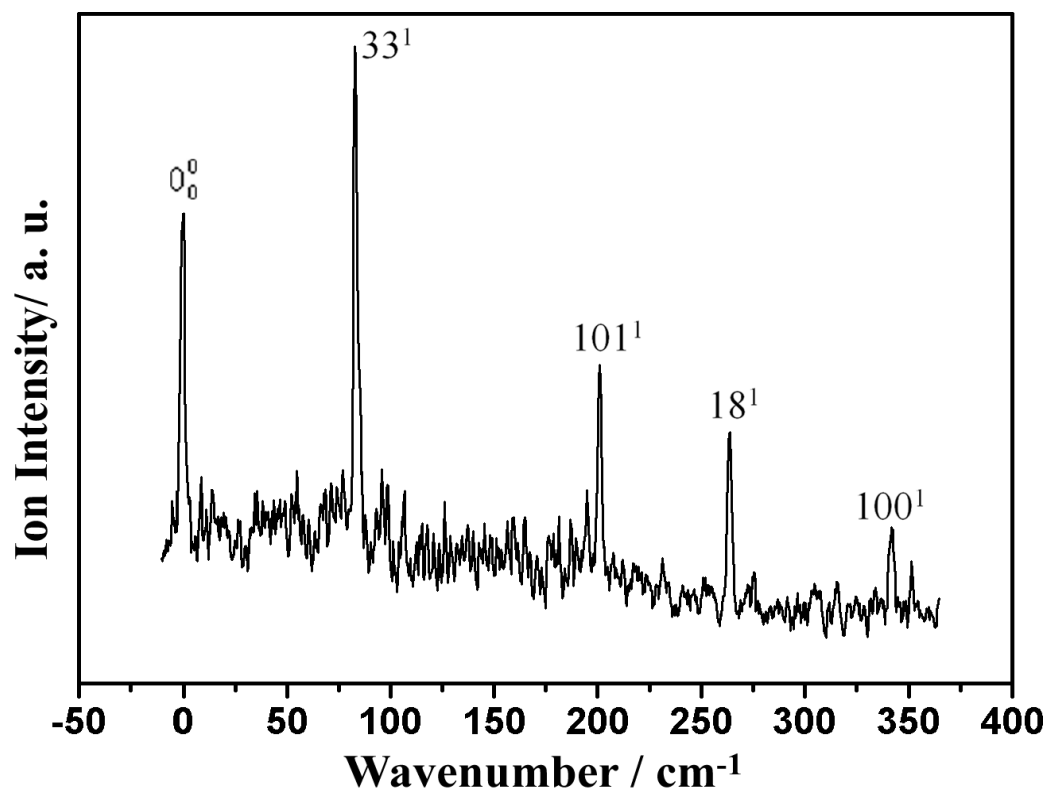


Figure 4.1  $1+1'$  REMPI spectrum of pentacene. The spectrum is shifted by  $18657 \text{ cm}^{-1}$  (the origin of the  $S_1 \leftarrow S_0$  transition) to emphasize the frequencies of the different vibrational modes of the  $S_1$  state.

Table 4.1 Observed and calculated vibrational frequencies of the  $S_1$  state of pentacene\*

Exp	Calc	Assignment (Mode, Symmetry)
83	93	$33^1$ , $B_{1g}$
199	177	$101^1$ , $B_{3u}$
263	256	$18^1$ , $A_g$
342	352	$100^1$ , $B_{3u}$

\*A scaling factor of 0.92 is included in the calculation result.

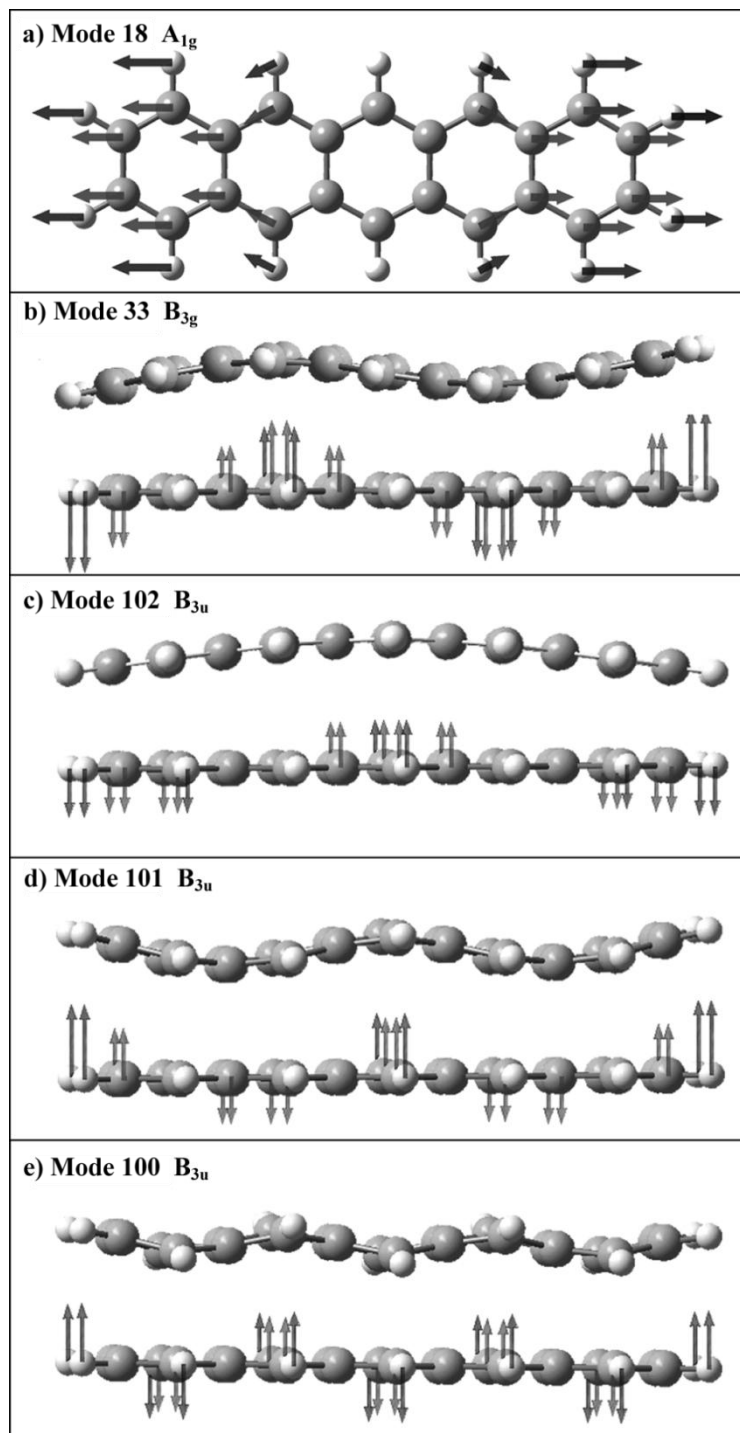


Figure 4.2 Displacement vectors for five normal modes of pentacene. Mode 102 is not observed in the REMPI spectrum of Figure 4.1 but observed in the ZEKE spectrum of Figure 4.3.

$A_g$  modes and levels with even quantum numbers of other modes are symmetry allowed, and odd levels of  $B_{3u}$  and  $B_{1g}$  modes are only allowed via vibronic coupling with higher excited states. The intensity of the symmetry allowed vibronic bands is determined by the overlap in the vibrational wavefunctions of the related electronic states. In Table 4.1, with the exception of mode 18, the rest of the observed bands are due to vibronic coupling. The intensities of these bands are comparable to or even stronger than the Franck-Condon allowed band.

The displacement vectors of the observed modes are shown in Figure 4.2. The assignment is based on symmetry analysis as well as calculation results. All current assignments agree with those proposed by Griffiths *et al.*<sup>40</sup> Our own theoretical result contains only one  $A_g$  mode below  $500\text{ cm}^{-1}$  after scaling. Hence the assignment of mode 18 corresponding to in-plane longitudinal stretching near  $260\text{ cm}^{-1}$  is unambiguous. Interestingly the same mode has also been observed in tetracene, anthracene, naphthalene and benzene.<sup>41-44</sup>

The assignment of the other three bands in Figure 4.1 is guided by the vibronic coupling principle. All three bands are fundamental transitions of Franck-Condon forbidden out-of-plane modes. For mode 33, although the experimental result differs from calculation by  $10\text{ cm}^{-1}$ , the assignment is confirmed based on two facts. First, it is the only possibility within  $25\text{ cm}^{-1}$  according to the theoretical calculation result; and second, this assignment can be confirmed from the ZEKE spectrum, as will be seen in the following section. The third peak in the REMPI

spectrum at  $199\text{ cm}^{-1}$  is  $33\text{ cm}^{-1}$  higher than the 0-2 transition of mode 33, and this difference is too large and is opposite to the trend of typical anharmonicity. Furthermore, there is no other symmetry allowed mode in this region from our calculation. Thus this peak at  $199\text{ cm}^{-1}$  has to be the fundamental transition of mode 101 with  $B_{3u}$  symmetry. The last peak at  $342\text{ cm}^{-1}$  is assigned as mode 100 with  $B_{3u}$  symmetry, consistent with the trend of the observed vibrational modes.

We attribute the violation of the Franck-Condon selection rule in pentacene to the decreased rigidity of the molecular structure. In polyacenes, the rigidity of the ribbon decreases with the increasing number of fused rings. Deformation of the molecular frame lowers the symmetry group of the molecule, relaxing the selection rule and activating forbidden modes. While tetracene was observed to strictly obey the selection rule,<sup>29</sup> pentacene is quite different. If we define the length of the ribbon as  $L$ , in Figure 4.2 among the observed waving modes, the waving cycles are changed from  $2L/3$  in mode 33 to  $L/2$  in mode 101 and to  $L/3$  in mode 100. If we further follow the  $2L/n$  pattern, where  $n$  is an integer, the mode with  $n = 5$  would correspond to  $B_{1g}$  symmetry at  $282\text{ cm}^{-1}$ . It is missing in the observed spectrum, probably due to the limited signal to noise ratio.

#### 4.5.2 ZEKE spectra

By scanning the ionization laser while setting the resonant laser at one of the intermediate states identified in the above REMPI experiment, we obtained

field ionization ZEKE spectra as shown in Figure 4.3. The assignment of the vibrational levels of the cation is noted by a superscript “+”. The experimental and theoretical values are shown in Table 4.2. The calculation was performed at the B3LYP/6-31G+ (dp) level with no scaling factor for the vibrational frequencies of the cation. Limited by the linewidth of the resonant transitions and the pulsed electric field, the uncertainty of the experimental values of the ZEKE spectra is  $7 \text{ cm}^{-1}$ . From trace 3a recorded via the origin of the  $S_1$  state, the adiabatic ionization potential is determined to be  $53266 \pm 7 \text{ cm}^{-1}$ , taking into account the shift induced by the delayed electric field. This value agrees with the result of  $6.589 \pm 0.001 \text{ eV}$  by Gruhn *et al.*<sup>45</sup>

Overall the spectra in Figure 4.3 are sparse, but they are not dominated by one vibrational band. Mode 102 is not observed in the REMPI spectrum and new to ZEKE. Its displacement vectors are shown in Figure 4.2. This mode is the lowest in frequency among the  $B_{3u}$  modes of the cation, corresponding to a complete waving cycle ( $n = 2$ ) in the out of plane vibrational motion. Mode  $101^+$  at  $187 \text{ cm}^{-1}$  and mode  $102^+$  at  $38 \text{ cm}^{-1}$  are only observable as a combination band  $101^+102^+$  at  $225 \text{ cm}^{-1}$ , and its presence is almost ubiquitous, observable in all three spectra (a – c). We did not observe any appreciable vibrational bands via the intermediate level  $100^1$ , probably due to its low intensity in the REMPI spectrum (Figure 4.1).

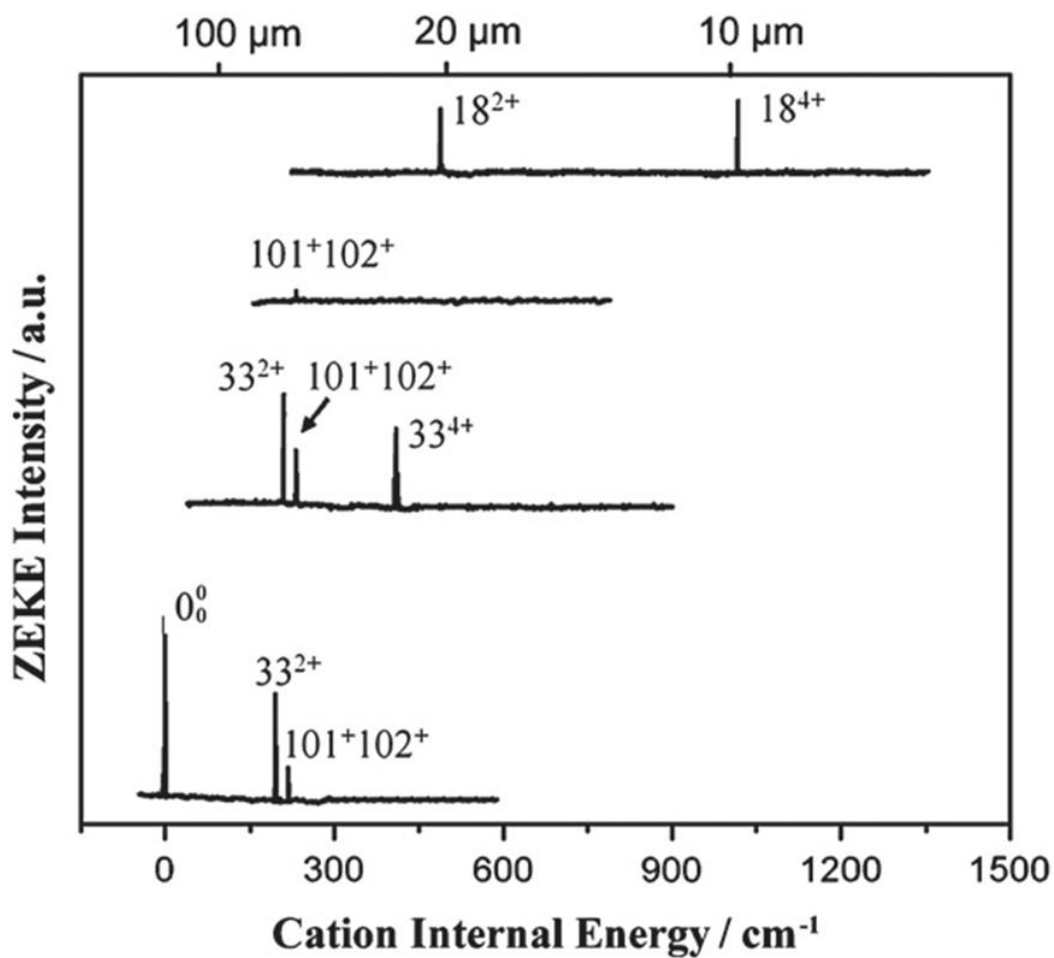


Figure 4.3 Two-color ZEKE spectra of pentacene recorded via the following vibrational levels of the  $S_1$  state as intermediate states: (a)  $0_0^0$ , (b)  $33^1$ , (c)  $101^1$ , (d)  $18^1$ . The energy in the abscissa is relative to the ionization threshold at  $53266 \text{ cm}^{-1}$ . The assignment in the figure refers to the vibrational levels of the cation.

Table 4.2 Observed and calculated vibrational frequencies of pentacene cation

$0_0^0$	$33_0^1$	$101_0^1$	$18_0^1$	Cal	assignment
0				0	$0^{0+}$
196	198			198	$33^{2+}$
219	221	221		225	$101^{+}102^{+}$
	396			396	$33^{4+}$
			520	522	$18^{2+}$
			1047	1044	$18^{4+}$

The agreement between theory and experiment in the ZEKE spectra can help to confirm the assignment of the intermediate vibrational levels of the  $S_1$  state. In our previous studies of substituted aromatic compounds,<sup>46-49</sup> we have observed a propensity rule where the vibrational excitation of the intermediate state is preserved during ionization. Although this propensity rule is not prominent in this case, some correlation is still expected. For example, the assignment of mode 33 in the ZEKE spectrum is definitive, while the assignment of the corresponding band in the REMPI spectrum has a difference of  $10\text{ cm}^{-1}$  between theory and experiment (Table 4.1). The ambiguity in the assignment of the REMPI spectrum can be removed when we consider the propensity of maintaining the same mode and level of vibrational excitation during ionization.

## 4.6 Discussion

### 4.6.1. Vibrational modes of the $S_1$ state

The observed mode structure should be reflective of the geometry changes upon electronic excitation. Table 4.3 lists the calculated geometric parameters for the three related electronic states of pentacene. The numbering scheme of the carbon atoms is shown in the top panel of Figure 4.4. The most significant changes upon electronic excitation and ionization are the length and width of the ribbon; both dimensions contract upon excitation and extend back close to their original values upon ionization. These changes are in accord with the activation of the

longitudinal stretching mode 18 in the spectrum. Interestingly, among the polyacenes we have investigated, this sequence of geometry change seems ubiquitous, and mode 18 has a universal presence in the REMPI spectrum of these polyacenes.

Some of the changes in bond length listed in Table 4.3 can be qualitatively explained by a simple Hückel calculation. Figure 4.4 shows the lowest unoccupied molecular orbital (LUMO) and the highest occupied molecular orbital (HOMO) from our simple Hückel calculation. The most dramatic change between the two orbitals is the disappearance of the horizontal nodal plane in the LUMO. Thus in the  $S_0 \rightarrow S_1$  transition when an electron is excited from the HOMO to the LUMO, the width of the ribbon should shrink due to the increasing bonding nature along the short axis. This result is in agreement with the higher level calculation listed in Table 4.3 where the bond lengths of C1 – C22, C3 – C20 and C5 – C18 all decrease from  $S_0$  to  $S_1$ . The shift of nodal planes in the longitudinal direction also incurs further changes. The disappearance of the nodal planes between C2 and C3 as well as C4 and C5 decreases the bond lengths of C2 – C3 and C4 – C5.

The rigidity of the molecule is expected to decrease with the elongation of the ribbon. In fact, the frequency of the  $A_g$  longitudinal stretching mode shifts to lower values with the increase of the number of aromatic rings: from  $923 \text{ cm}^{-1}$  for benzene<sup>41</sup>,  $501 \text{ cm}^{-1}$  for naphthalene<sup>42</sup>,  $390 \text{ cm}^{-1}$  for anthracene<sup>44</sup>,  $307 \text{ cm}^{-1}$  for tetracene<sup>43</sup>, to  $263 \text{ cm}^{-1}$  for pentacene. Moreover, the selection rule becomes

Table 4.3 Molecular geometry parameters of pentacene in the  $S_0$ ,  $S_1$ , and  $D_0$  states

Bond length (Å)	$S_0$	$S_1$	$D_0$
C1 – C2	1.367	1.369	1.378
C2 – C3	1.437	1.416	1.424
C3 – C4	1.390	1.409	1.405
C4 – C5	1.416	1.389	1.406
C5 – C6	1.404	1.404	1.407
C1 – C22	1.434	1.412	1.421
C3 – C20	1.456	1.427	1.448
C5 – C18	1.458	1.453	1.456
Distance (Å)			
C1 – C11	12.247	12.210	12.236
C2 – C21	2.823	2.790	2.824
(C4 – C19)	(2.818)	(2.792)	(2.821)
(C6 – C17)	(2.820)	(2.780)	(2.824)

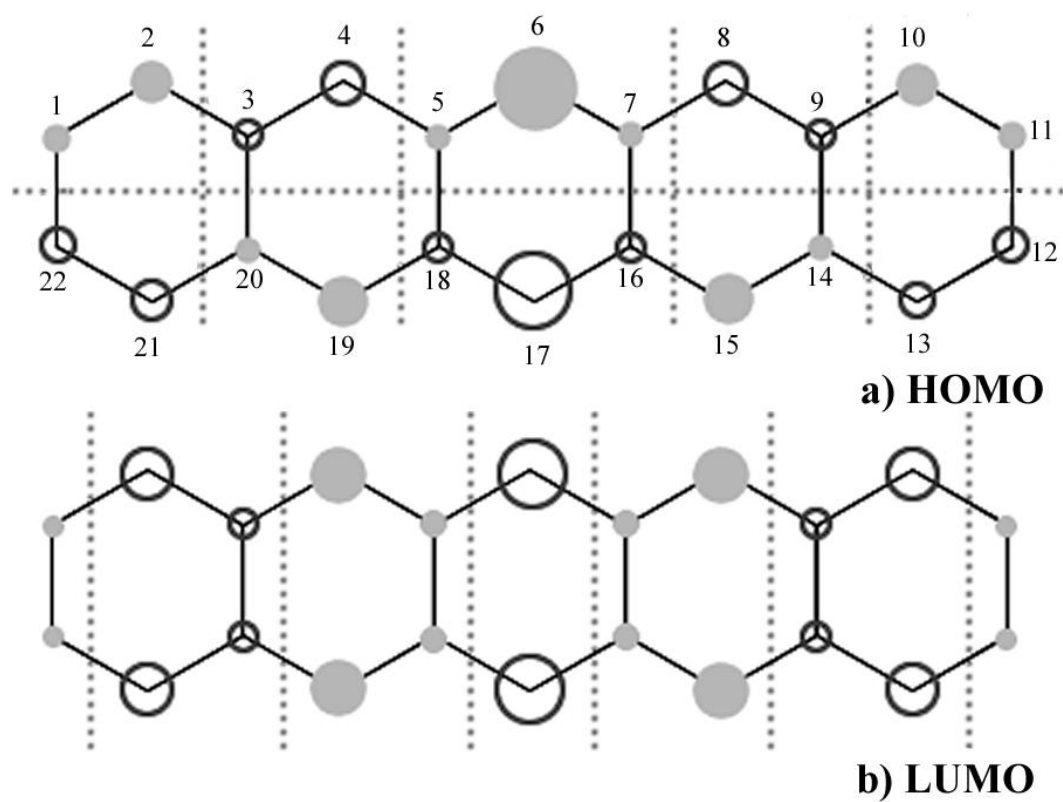


Figure 4.4 (a) HOMO and (b) LUMO of pentacene with the numbering scheme of the carbon atoms. The dashed lines mark the nodal planes based on a simple Hückel calculation.

relaxed, and the Franck-Condon forbidden but vibronic allowed bands show increasing intensities with the elongation of the molecular frame. The  $S_1$  state of anthracene exhibits weak but yet observable activities of several  $B_{1g}$  modes. For tetracene, additional weak  $A_u$  modes are also recognizable. In pentacene, the Franck-Condon forbidden modes are nearly equal in intensity or even stronger than that of the  $A_g$  mode.

The flexibility of the pentacene ribbon is a subtle effect and challenges our theoretical calculation methods. Our CIS results indicate that the first excited state of pentacene is slightly nonplanar, and the C-C bond in the central ring is likely weakened by this geometric deformation. We then conducted the Franck-Condon calculation associated with  $D_0 \leftarrow S_1$  and  $S_1 \leftarrow S_0$  transitions. However, the resulting vibronic structures are still dominated by  $A_g$  modes; the intensities of which are several orders higher than those of the Franck-Condon forbidden modes. This disagreement illustrates the inaccuracy in the geometry of the first excited state. Moreover, simple Hückel calculation resulted in four vertical nodal planes in the HOMO and six vertical nodal planes in the LUMO. Thus we would intuitively expect that during the  $S_1 \leftarrow S_0$  transition, the ribbon should elongate along the long axis, which is opposite from our higher level CIS calculation (Table 4.3). We suspect that explicit inclusion of vibronic coupling is needed to even qualitatively reproduce the experimental intensity and hence the molecular geometry.

#### 4.6.2 Vibrational modes of the cation

Although the sparse ZEKE spectra of all reported polyacenes are indicative of small changes in geometry upon ionization from the electronically excited intermediate state, the spectra in Fig. 3 do not show clear propensity in preserving the vibrational motion of the intermediate  $S_1$  state. In fact, the geometry of the cation is more similar to that of the neutral ground state than that of the first excited state. In the ionization step based on our calculation, the molecular frame changes from slightly non-planar to planar, activating the  $B_{3u}$  mode. From a simple intuitive consideration, ionization involves removal of the electron from the LUMO, which leaves a single electron in the HOMO. Some degree of recovery in the bonding nature of the  $S_0$  state is therefore expected.

The frequency of the  $A_g$  longitudinal stretching mode of the cation shares the same trend as that of the  $S_1$  state, with decreasing values from anthracene to pentacene. The flexibility of the ribbon is also the most prominently manifested in the ZEKE spectra of pentacene. For anthracene and tetracene, the modes observed in ZEKE are identical to those observed in REMPI. For pentacene, however, a new mode  $102^+$  is observed in ZEKE from the combination band  $101^+102^+$ . Calculation of the ZEKE spectra based on the geometry of the  $S_1$  state, on the other hand, cannot reproduce the relative intensities of the observed vibrational modes, due to the inaccuracy of the theoretical structure of the  $S_1$  state.

### 4.6.3 Remarks on the comparison between experimental and theoretical vibrational frequencies

The quality of agreement between experiment and theory from Tables 4.1 and 4.2 is quite different. In Table 4.2, the experimental vibrational frequencies of the cation agree with the unscaled calculation results within the experimental error, while in Table 4.1, after a scaling factor of 0.92, the disagreement is still obvious. In addition, there is no reliable trend in the disagreement; while the theoretical value is larger than the experimental value at the two extremes of the spectrum (mode 33 and 100), the opposite is true for the middle section of the spectrum (mode 101 and 18). This result highlights the limit of the prediction power of calculation: while we can rely on the DFT results for the ground state, the calculation of excited electronic states is still problematic. This situation is in accord with the analysis of §4.6.1, where violation of the Franck-Condon selection rule and inconsistency in the geometric changes upon electronic excitation and ionization were noted.

The reliability of the frequency calculation for the ground state of the cation can be used to predict the frequency of other modes unobservable from ZEKE. Cationic pentacene has 15 IR active modes with non-negligible intensities below  $1000\text{ cm}^{-1}$ , as listed in Table 4.4. Hudgins & Allamandola reported the IR spectroscopy of pentacene cation using the matrix isolation method covering the near- and mid-IR region ( $740\text{ cm}^{-1}$  to  $1550\text{ cm}^{-1}$ )<sup>50</sup>. The authors reported four

modes at 741, 749, 862, and 934  $\text{cm}^{-1}$ , none of which were observable in our experiment but were obtained from our calculation in Table 4.4. The experimental frequencies from the work of Hudgins & Allamandola agree with our calculation within 23  $\text{cm}^{-1}$ . Together with our results, the two complementary experiments span 1500  $\text{cm}^{-1}$  containing five observed experimental values (bold-phased in Table 4.4).

The structural information from calculation should be treated with caution. The REMPI and ZEKE spectra are dominated by vibronic coupling, and our CIS calculation has failed to capture the accurate structure of the molecular frame. Calculations of IR transition intensities and rotational constants therefore await further improvements in theoretical modeling, most likely with the explicit inclusion of vibronic coupling.<sup>51-54</sup>

#### 4.6.4 Astrophysical implications

In Figure 4.5 we display the calculated FIR spectra of cationic naphthalene, anthracene, tetracene, and pentacene with DFT using the 6-31G+(dp) basic set. It is apparent that their FIR spectroscopy, particularly in the range with  $\lambda > 30 \mu\text{m}$ , differs considerably from one PAH species to another. In contrast, their mid-IR modes do not distinguish themselves as much<sup>51</sup>. This is because the mid-IR bands are mostly representative of functional groups, not the molecular frame, while the FIR bands arise from bending of the whole PAH skeleton (mostly out-of-plane) and are thus intrinsically related to the molecular structure.<sup>20,56-58</sup>

One can also see from Figure 4.5 that the FIR bands are much weaker than the mid-IR vibrational bands and thus make them more difficult to detect in space. This is unfortunate since PAHs tend to release their vibrational energy mostly through mid-IR emission.<sup>20,56-59</sup> However, with the advent of space-borne and airborne FIR telescopes and the ground-based *Atacama Large Millimeter Array* (ALMA), particularly in view of the prospects of much improved sensitivity with future space instruments, it is not impossible that individual PAH molecules may be identified in.<sup>8</sup> We also plot in Figure 4.5 the wavelength coverages of some key space telescopes as well as ALMA which may allow one to explore the identification of specific PAH molecules in space through their FIR bands. Although only two IR active modes of cationic pentacene at 53.3 and 266  $\mu\text{m}$  have been observed in this work, all three IR active modes including the one at 84.8  $\mu\text{m}$  may be detectable by space missions such as the SAFARI instrument on board SPICA.

Finally, we should note that the four PAH species (naphthalene, anthracene, tetracene, and pentacene) shown in Figure 4.5 are all ribbon-like catacondensed molecules. In the Galactic and extragalactic ISM, the typical PAHs may be larger and have a compact, pericondensed structure (see Figure 1 of Ref 2), as small PAHs with an open structure may not survive under the harsh interstellar.<sup>60,iv</sup>

---

<sup>iv</sup> However, naphthalene has been detected in the Stardust cometary sample<sup>20</sup>, although some uncertainties still remain.<sup>22,23</sup>

Table 4.4. IR active FIR modes of cationic pentacene from DFT calculation

Frequency/ cm <sup>-1</sup>	Intensity	Frequency/ cm <sup>-1</sup>	Intensity	Frequency/ cm <sup>-1</sup>	Intensity
<b>38</b>	<b>0.62</b>	481	12.93	<b>766</b>	<b>100.00</b>
118	0.88	488	0.28	<b>879</b>	<b>15.99</b>
<b>187</b>	<b>1.89</b>	579	2.19	916	1.37
362	0.17	634	0.63	<b>957</b>	<b>73.92</b>
447	31.27	<b>753</b>	<b>2.44</b>	994	13.92

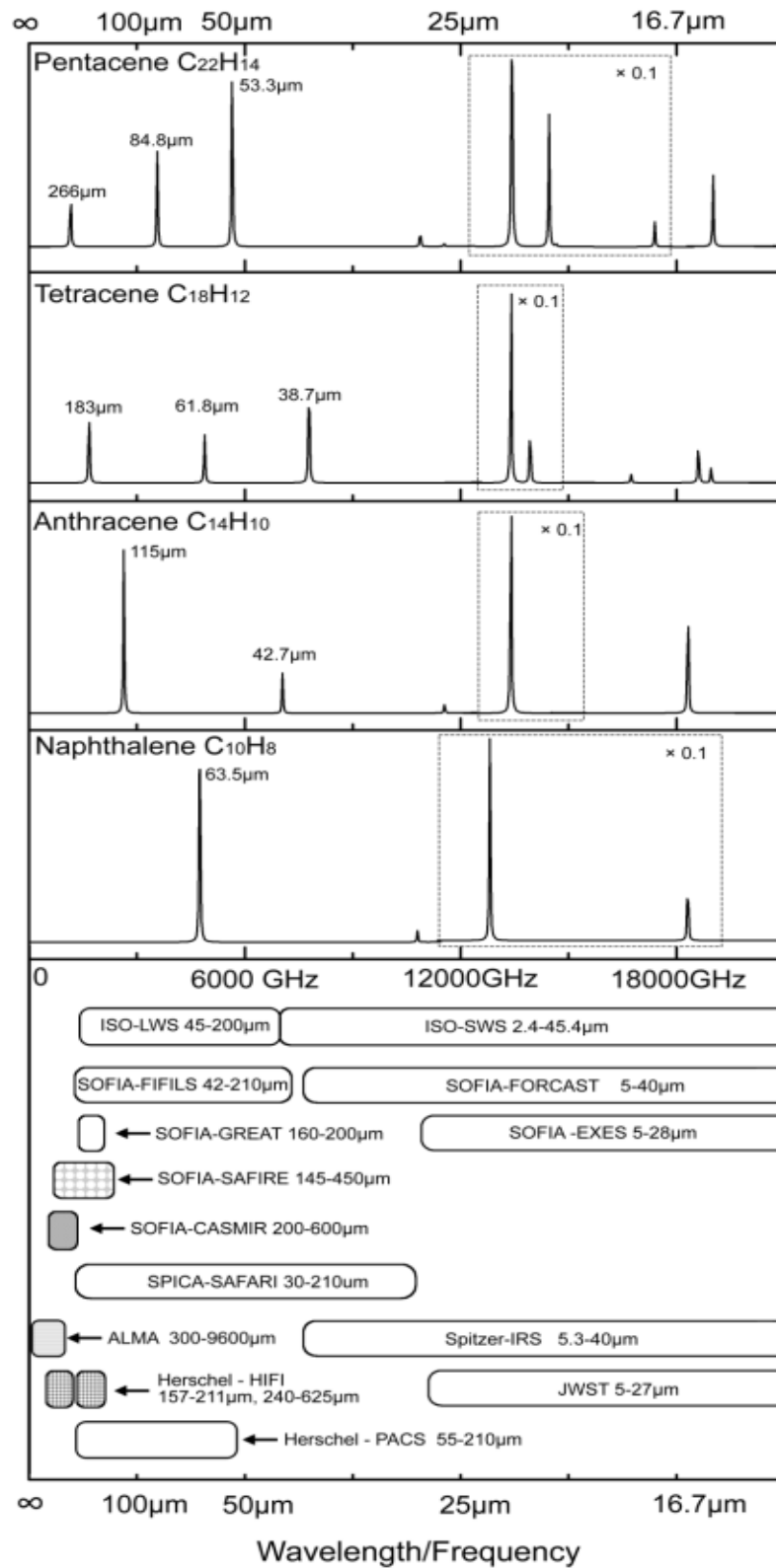


Figure 4.5 The calculated IR spectroscopy of naphthalene, anthracene, tetracene, and pentacene. Also shown are the wavelength coverages of some key astronomical instruments which are relevant for detecting individual PAHs in space: (1) the *Heterodyne Instrument for the Far-Infrared* (HIFI; 157--211  $\mu\text{m}$ , 240--625  $\mu\text{m}$ ) and the *Photodetector Array Camera and Spectrometer* (PACS; 55--210  $\mu\text{m}$ , 240--625  $\mu\text{m}$ ) on board *Herschel*, (2) the *SPICA Far-Infrared Instrument* (SAFARI; 30--210  $\mu\text{m}$ ), a FIR imaging spectrometer on board the *Space Infrared Telescope for Cosmology and Astrophysics* (SPICA); (3) *ALMA* (0.3--9.6 mm); (4) the *Long Wavelength Spectrometer* (LWS; 45--200  $\mu\text{m}$ ) and the *Shorter Wavelength Spectrometer* (SWS; 2.4--45.4  $\mu\text{m}$ ) on board the *Infrared Space Observatories* (ISO); and (5) the *Caltech Submillimeter Interstellar Medium Investigations Receiver* (CASMIR; 200--600  $\mu\text{m}$ ), the *Field Imaging Far-Infrared Line Spectrometer* (FIFILS; 42--210  $\mu\text{m}$ ), the *German Receiver for Astronomy at Terahertz Frequencies* (GREAT; 160--200  $\mu\text{m}$ ), and the *Submillimeter and Far-Infrared Experiment* (SAFIRE; 145--450  $\mu\text{m}$ ) on board *SOFIA*. Also shown are the wavelength coverages of the *Infrared Spectrograph* (IRS; 5.3--40  $\mu\text{m}$ ) on board the *Spitzer Space Telescope* and the *Mid-Infrared Instrument* (MIRI; 5--27  $\mu\text{m}$ ) on board the *James Webb Space Telescope* (JWST), the *Faint Object Infrared Camera for the SOFIA Telescope* (FORCAST; 5--40  $\mu\text{m}$ ) and the *Echelon-Cross-Echelle Spectrograph* (EXES; 5--28  $\mu\text{m}$ ) on board *SOFIA*.

Nonetheless, a careful compilation of the FIR vibrational frequencies of small PAHs would at least provide a very useful complement to the NASA/Ames mid-IR spectroscopy database of PAHs of a range of sizes.<sup>61</sup> In addition, several pericondensed PAHs are under investigation in our laboratory using the same technique.

#### **4.7 Conclusion**

Spectroscopic properties of the electronically excited and ionic states of pentacene have been studied using REMPI and ZEKE. We have identified a total symmetric  $A_g$  mode corresponding to stretching of the long axis. The decreasing vibrational frequency of this mode from naphthalene to pentacene signifies the increasing flexibility of the molecular frame. For the cation, we have also observed two IR active modes in a combination band, which related to the out-of-plane waving motion of the molecular frame and may be detectable by space missions such as the SAFARI instrument on board SPICA. Simple Hückle calculations can partially explain the changes in geometry regarding the addition or elimination of nodal planes in the LUMO and HOMO. However, it assumes planar geometry and hence fails to include any effect of out-of-plane deformation. From comparisons between theoretical and experimental results, we have concluded that frequency values from DFT using the B3LYP functional with the 6-31G+ (dp) basis set for the ground state of the cation are reasonably reliable, hence frequency information

relevant for astronomy can be retrieved with some confidence. However, vibronic coupling dominates the spectra, and the reliability of theoretical intensity and geometric parameters awaits further theoretical modeling.

ZEKE spectroscopy is particularly sensitive to low frequency modes of the molecular frame, which gives it a superior advantage in fingerprinting the skeletal motions of the molecular species. The combination of LD and ZEKE has the potential of being an important tool in astrophysics. Although ZEKE follows a different selection rule from IR spectroscopy, and in the current experiment, it only samples a limited number of vibrational modes, it can bench mark a few of the observed modes, guiding theoretical developments and refining theoretical predictions.

#### **4.8 Acknowledgement**

We are grateful to our talented machinist, Ted Hinke, for his designs and modifications of the experimental apparatus. This work is supported by the National Aeronautics and Space Administration under award No. NNX09AC03G. Aigen Li is supported in part by the NSF grant AST 07-07866, a Spitzer Theory grant and a Herschel Theory grant.

## 4.8 References

- (1) Gillett, F. C., Forrest, W. J., & Merrill, K. M. **1973**, *ApJ*, *183*, 87
- (2) Li, A. **2009**, in: *Deep Impact as a World Observatory Event – Synergies in Space, Time, and Wavelength*, Käfl, H.U., & Sterken, C. (eds.), ESO Astrophys. Symp., 161
- (3) Joblin, C., Leger, A., & Martin, P. **1992**, *ApJ*, *393*, L79
- (4) Li, A., & Draine, B. T. **2001**, *ApJ*, *554*, 778
- (5) Steglich, M., Jäger, C., Rouillé G., Huisken, F., Mutschke, H., & Henning, T. **2010**, *ApJ*, *712*, L16
- (6) Salama, F., Galazutdinov, G. A., Krelowski, J., Allamandola, L. J., & Musaev, F. A. **1999**, *ApJ*, *526*, 265
- (7) Weingartner, J. C., & Draine, B. T. **2001**, *ApJS*, *134*, 263
- (8) Mulas, G., Mallocci, G., Joblin, C., & Toubanc, D. **2006**, *A&A*, *456*, 161
- (9) Bernstein, M. P., Dworkin, J. P., Sandford, S. A., Cooper, G. W., & Allamandola, L. J. **2002**, *Nature*, *416*, 401
- (10) Shock, E. L., & Schulte, M. D. **1990**, *Nature*, *343*, 728
- (11) Wakeham, S. G., Schaffner, C., & Giger, W. **1980**, *Geochim. Cosmochim. Acta*, *44*, 415
- (12) Léger, A., & Puget, J. L. **1984**, *A&A*, *137*, L5
- (13) Allamandola, L. J., Tielens, A. G. G. M., & Barker, J. R. **1985**, *ApJ*, *290*, L25
- (14) Moutou, C., Léger, A., D’Hendecourt, L. **1996**, *A&A*, *310*, 297
- (15) Beintema, D. A., et al. **1996**, *A&A*, *315*, L369
- (16) Smith, J. D. T., et al. **2004**, *ApJS*, *154*, 199
- (17) Smith, J. D. T., et al. **2007**, *ApJ*, *656*, 770
- (18) Langhoff, S. R. **1996**, *J. Phys. Chem.*, *100*, 2819
- (19) Zhang, K., Guo, B., Colarusso, P., & Bernath, P. F. **1996**, *Science*, *274*, 582
- (20) Joblin, C., Berné O., Simon, A., & Mulas, G. **2009**, arXiv:0904.3185
- (21) Sandford, S. A., et al. **2006**, *Science*, *314*, 1720
- (22) Clemett, S. J., Maechling, C. R., Zare, R. N., Swan, P. D., & Walker, R. M. **1993**, *Science*, *262*, 721
- (23) Spencer, M. K., & Zare, R. N. **2007**, *Science*, *317*, 1680
- (24) Sandford, S. A., & Brownlee, D.E. **2007**, *Science*, *317*, 1680
- (25) Désert, F. X., Boulanger, F., & Puget, J. L. **1990**, *A&A*, *237*, 215
- (26) Draine, B. T., & Li, A. **2001**, *ApJ*, *551*, 807
- (27) Draine, B. T., & Li, A. **2007**, *ApJ*, *657*, 810
- (28) Schutte, W. A., Tielens, A. G. G. M., & Allamandola, L. J. **1993**, *ApJ*, *415*, 397
- (29) Zhang, J., Pei, L., & Kong, W. **2008**, *J. Chem. Phys.*, *128*, 104301

- (30) Cockett, M. C. R., Ozeki, H., Okuyama, K., & Kimura, K. **1993**, *J. Chem. Phys.*, *98*, 7763
- (31) Cockett, M. C. R., & Kimura, K. **1994**, *J. Chem. Phys.*, *100*, 3429
- (32) Schlag, E. W. 1998, *ZEKE Spectroscopy* (Cambridge: Cambridge University Press)
- (33) Ng, C.-Y. **1991**, *Vacuum ultraviolet photoionization and photodissociation of molecules and clusters* (Singapore: World Scientific Publishing Co. Pte. Ltd.)
- (34) Merkt, F., & Schmutz, H. **1998**, *J. Chem. Phys.*, *108*, 10033
- (35) Osterwalder, A., & Merkt, F. **1999**, *Phys. Rev. Lett.*, *82*, 1831
- (36) Mons, M., Dimicoli, I., Piuze, F., Tardivel, B., & Elhanine, M. **2002**, *J. Phys. Chem. A*, *106*, 5088
- (37) Nir, E., Kleinermanns, K., & de Vries, M. S. **2000**, *Nature*, *408*, 949
- (38) Frisch, M. J., et al. 2003, *Gaussian 03*, Revision C.02.
- (39) Casida, M. E., Jamorski, C., Casida, K. C., & Sulahub D. R. **1998**, *J. Chem. Phys.*, *108*, 4439
- (40) Griffiths, A. M., & Freedman, P. A. **1982**, *J. Chem. Soc., Faraday Trans. 2*, *78*, 391
- (41) Garforth, F. M., Ingold, C. K., & Poole, H. G. **1948**, *J. Chem. Soc.*, 491
- (42) Beck, S. M., Powers, D. E., Hopkins, J. B., & Smalley, R. E. **1980**, *J. Chem. Phys.*, *73*, 2019
- (43) Amirav, A., Even, U., & Jortner, J. **1981**, *J. Chem. Phys.*, *75*, 3770
- (44) Lambert, W. R., Felker, P. M., Syage, J. A., & Zewail, A. H. **1984**, *J. Chem. Phys.*, *81*, 2195
- (45) Gruhn, N. E., da Silva Filho, D. A., Bill, T. G., Malagoli, M., Coropceanu, V., Kahn, A., & Bredas, J. L. **2002**, *J. Am. Chem. Soc.*, *124*, 7918
- (46) He, Y., Wu, C., & Kong, W. **2004**, *J. Chem. Phys.*, *121*, 8321
- (47) He, Y., Wu, C., & Kong, W. **2004**, *Chem. Phys. Lett.*, *391*, 38
- (48) He, Y., Wu, C., & Kong, W. **2004**, *J. Chem. Phys.*, *121*, 3533
- (49) Wu, C., He, Y., & Kong, W. **2004**, *Chem. Phys. Lett.*, *398*, 351
- (50) Hudgins, D. M., & Allamandola, L. J. **1995**, *J. Phys. Chem.*, *99*, 8978
- (51) Allamandola, L. J., & Hudgins, D. M. **2003**, *Solid State Astrochem.*, 251
- (52) Burrill, A. B., Chung, Y. K., Mann, H. A., & Johnson, P. M. **2004**, *J. Chem. Phys.*, *120*, 8587
- (53) Goode, J. G., Hofstein, J. D., & Johnson, P. M. **1997**, *J. Chem. Phys.*, *107*, 1703
- (54) Johnson, P. M. **2002**, *J. Chem. Phys.*, *117*, 9991
- (55) Johnson, P. M. **2002**, *J. Chem. Phys.*, *117*, 10001
- (56) Berné O., et al. **2009**, *SPICA Joint European/Japanese Workshop*, Edited by A. M. Heras, B.M. Swinyard, K. G. Isaak, & J. R. Goicoechea, EDP Sciences, 3005
- (57) Mattioda, A. L., et al. **2009**, *ApJ*, *137*, 4054
- (58) Ricca, A., Bauschlicher, C. W., Mattioda, A. L., Boersma, C., & Allamandola, L. J. **2010**, *ApJ*, *709*, 42

- (59) Li, A. **2004**, in: *Astrophysics of Dust*, Witt, A.N., Clayton, G.C., & Draine, B.T. (eds.), ASP Conf. Ser., 309, 417
- (60) Tielens, A. G. G. M. **2008**, *A&A*, 46, 289
- (61) Bauschlicher, C. W., et al. **2010**, *ApJS*, submitted

**Zero kinetic energy photoelectron spectroscopy of pyrene**

Jie Zhang, Fangyuan Han, and Wei Kong\*

*Department of Chemistry, Oregon State University, Corvallis, Oregon 97331-4003*

Journal of Physical Chemistry A

PO Box 3337, Columbus, HO, 43210, USA

**2010**, *submitted*.

---

\* To whom correspondence should be addressed.

E-mail: [Wei.Kong@oregonstate.edu](mailto:Wei.Kong@oregonstate.edu), Phone: 541-737-6714. Fax: 541-737-2062

## Chapter 5 Zero kinetic energy photoelectron spectroscopy of pyrene

### 5.1 Abstract

We report zero kinetic energy photoelectron (ZEKE) spectroscopy of pyrene via resonantly enhanced multiphoton ionization. Our analysis centers on the symmetry of the first electronically excited state ( $S_1$ ), its vibrational modes, and the vibration of the ground cationic state ( $D_0$ ). From comparisons between the observed vibrational frequencies and those from *ab initio* calculations at the configuration interaction singles level using the 6-311G (d,p) basis set, and based on other previous experimental and theoretical reports, we confirm the  ${}^1B_{2u}$  symmetry for the  $S_1$  state. This assignment represents a reversal in the energy order of the two closely spaced electronically excited states from our theoretical calculation, and extensive configuration interactions are attributed to this result. Among the observed vibrational levels of the  $S_1$  state, three are results of vibronic coupling due to the nearby second electronically excited state. The ZEKE spectroscopy obtained via the vibronic levels of the  $S_1$  state reveals similar modes for the cation as those of the intermediate state. Although we believe that the ground ionic state can be considered a single electron configuration, the agreement between theoretical and experimental frequencies for the cation is limited. This result is somewhat surprising based on our previous work on cata-condensed polycyclic aromatic hydrocarbons and small substituted aromatic compounds.

Although a relatively small molecule, pyrene demonstrates its non-rigidity via several out-of-plane bending modes corresponding to corrugation of the molecular plane. The adiabatic ionization potential of neutral pyrene is determined to be  $59888 \pm 7 \text{ cm}^{-1}$ .

## 5.2 Introduction

Polycyclic aromatic hydrocarbons (PAHs), also known as polyarenes, are hydrocarbon compounds consisting of more than two fused aromatic rings without any heteroatoms or substituents. In the arena of fundamental chemistry and physics, PAHs are an interesting group of molecules: the hexagonal linkages of the carbon atoms in PAHs determine their high geometric symmetry, and the delocalization of  $\pi$  electrons has played an important role in the development of the Hückel theory.<sup>1</sup> From a practical point of view, atmospheric PAHs are formed during incomplete combustion of fossil fuels, garbage, or other organic substances like tobacco or charbroiled meat, hence they are also related to environmental toxicity<sup>2</sup> and carcinogenicity.<sup>3-5</sup> More recently, PAHs have gained further interests because of their connection and application in molecular engineering of electronic devices.<sup>6,7</sup> In astrophysics and particularly in studies of the interstellar medium (ISM),<sup>8,9</sup> these carbon abundant molecules have been suggested to be potentially related to the origin of life via the formation of primitive organic molecules including amino acids in the pre-DNA world.<sup>10-12</sup> In addition, neutral and ionic PAHs are considered

promising candidates for the interstellar absorption and emission bands, including the unidentified infrared (UIB) emission bands.<sup>13-19</sup>

Spectroscopic identification of individual PAH molecules requires unique fingerprints of each molecule. While all PAHs have common structural features and hence common spectroscopic signatures, particularly in the mid-infrared (MIR), the unique fingerprint of each individual molecule lies in the far-infrared (FIR). This is because MIR modes are mostly representative of local functional groups, while FIR modes are representative of the skeletal motions of the whole molecular frame.<sup>20-22</sup> Consequently, although many studies have been devoted to MIR spectroscopy of neutral and charged PAHs,<sup>23-28</sup> no specific PAH molecule has been identified yet in the ISM. Moreover, PAH cations are speculated to be even more probable candidates as carriers of UIBs than their neutral counterparts.<sup>20,29</sup> Hence FIR spectroscopy of PAH cations is instrumental in mapping out the chemical composition of the ISM.

The technique of zero kinetic energy photoelectron (ZEKE) spectroscopy offers an indirect solution to this challenge in astrophysics.<sup>30</sup> ZEKE is known for its high resolution of cation rovibrational spectroscopy. The high Rydberg states in ZEKE are longer lived when they are associated with lower vibronic states of the cation, which makes it particularly suitable for studies of lower frequency vibrational modes. Thus by detecting electrons from pulsed field ionization in ZEKE spectroscopy, we can avoid both the light source and the detector problems

in typical FIR and sub-millimeter wave experiments. The vibrational information from ZEKE is largely governed by the Franck-Condon principle, hence the information from ZEKE might not be directly applicable for line identification in astronomy. However, as we have demonstrated in pentacene,<sup>31</sup> vibronic coupling can probe some IR active modes. In addition, by offering measurements of several IR forbidden modes, ZEKE can serve as an experimental calibration method for the active bands in the FIR. Moreover, IR forbidden modes are relevant to the modeling of the energy balance in the interstellar medium and to the modeling of PAH emissions with high internal temperatures.<sup>32-36</sup> Hence ZEKE offers complementary information to and fills the gap in techniques of single photon absorption or emission.<sup>23,37-40</sup>

PAHs can be classified into two groups: acenes and phenes. Acenes are cata-condensed (cata-fused) PAHs in which no carbon atom is shared by more than two rings. Phenes are peri-condensed PAHs in which at least one carbon atom is shared by three rings.<sup>5</sup> There have been several reports of ZEKE spectroscopy of small cata-condensed PAHs including naphthalene, anthracene, tetracene and pentacene.<sup>31,41-43</sup> In our studies of tetracene and pentacene, we have observed total symmetric  $a_g$  modes allowed by the Franck-Condon principle, and IR active modes through vibronic coupling.<sup>31,43</sup> Pyrene is a peri-condensed PAH molecule. Its first two electronically excited states have been widely studied both experimentally and theoretically in the gas phase and in the condensed phase.<sup>44-49</sup> The infrared

spectroscopy of neutral pyrene is also thoroughly studied in rare gas matrices, solid state, and gas phase.<sup>50</sup> However, not much information of the cation in the FIR region has been revealed yet, although many work have been devoted to the mid-IR and near-IR region,<sup>23,37-40</sup> ranging from 500 to 3000  $\text{cm}^{-1}$ . In this paper, we report two-color two photon REMPI and ZEKE spectroscopy of pyrene. We present detailed spectroscopic analysis for the vibrational levels of the first electronically excited state ( $S_1$ ) and the ground cationic state ( $D_0$ ). Additional insights can be obtained from the results of *ab initio* and density functional calculations. Structural changes due to electronic excitation and ionization will be elucidated from the observed active vibrational modes and from comparisons between the REMPI and ZEKE spectra.

### 5.3 Experimental setup

The experimental apparatus is a standard molecular beam machine with a differentially pumped high vacuum system and a time-of-flight mass spectrometer, which can be converted into a pulsed field ionization zero kinetic energy photoelectron spectrometer.<sup>43</sup> The sample pyrene (Aldrich) was housed and heated to 160  $^{\circ}\text{C}$  in the nozzle to obtain sufficient vapor pressure. The vapor was seeded in 3 atm of argon and expanded into vacuum through a pulsed valve with a 1 mm orifice. The laser systems for the REMPI experiment included a Nd:YAG (Precision II 8000, Continuum) pumped optical parametric oscillator (OPO,

Panther, Continuum) and a Nd:YAG (Spectra Physics, GCR 230) pumped dye laser (Laser Analytical Systems, LDL 2051). The pump laser in the 354 - 370 nm range with a bandwidth of  $0.3 \text{ cm}^{-1}$  obtained from the frequency-doubled dye laser system, had a pulsed energy of 1.5 mJ/pulse. The ionization laser in the 300-315 nm range with a bandwidth of  $1.3 \text{ cm}^{-1}$  from the frequency-doubled output of the OPO system had a pulse energy of 0.5 mJ/pulse. The absolute wavelength of each laser was calibrated using an iron hollow-cathode lamp filled with neon. The pump laser and ionization laser were set to counter-propagate, and the light path, the flight tube, and the molecular beam were mutually perpendicular. The relative timing among the three laser pulses was controlled by two delay generators (Stanford Research, DG 535), and the optimal signal was obtained under temporal overlap between the pump and ionization lasers. In the ZEKE experiment, molecules excited to high Rydberg states were allowed to stay for 1 - 2  $\mu\text{s}$  in the presence of a constant DC spoiling field of  $\sim 1 \text{ V/cm}$ , after which ionization and extraction were achieved by a pulsed electric field of  $\sim 5 \text{ V/cm}$ .

Gaussian 03 suite<sup>51</sup> was used to optimize the molecular structure and to obtain vibrational frequencies for assignment of the observed vibronic structures from REMPI and ZEKE. For the ground state of the neutral and the cationic state, density functional theory (DFT) calculations using the B3LYP functional were performed with the 6-311G (d,p) basis set. For the excited electronic state, configuration interaction singles (CIS) with 6-311G (d,p) basis set was dictated by

the size of the molecule and by our computational resources. In addition, we have also used the same method for other PAHs and a few benzene derivatives with satisfactory results.<sup>31,43,52-56</sup> The vibrational frequencies from our CIS calculation were scaled by a factor of 0.9245, the choice of which will be discussed in the following section. For the  $D_0$  state, a scaling factor of 0.995 was adopted.

## 5.4 Results

### 5.4.1 Two-color 1+1' REMPI spectroscopy

The two-color 1+1' REMPI spectrum of pyrene near the origin of the  $S_1 \leftarrow S_0$  electronic transition is displayed in Figure 5.1. The ionization laser was set at 280 nm and was temporally overlapped with the scanning resonant laser. The intense peak at  $27211 \text{ cm}^{-1}$  is assigned as the origin band, and the other observed vibronic transitions are listed in Table 5.1. The labeling of each vibrational mode is based on spectroscopic conventions, i. e. by using consecutive numbers in reference to the symmetry species and the frequency in decreasing order. Due to the fact that vibrational frequencies generated by *ab initio* calculations are usually too high, we used a scaling factor and adjusted its value to match the experimental results using a least-squares linear regression method. The resulting scaling factor of 0.9245 had a value of 0.9996 for the coefficient of determination ( $R^2$ ). With this scaling factor, the maximum deviation between theory and experiment is  $6 \text{ cm}^{-1}$ .

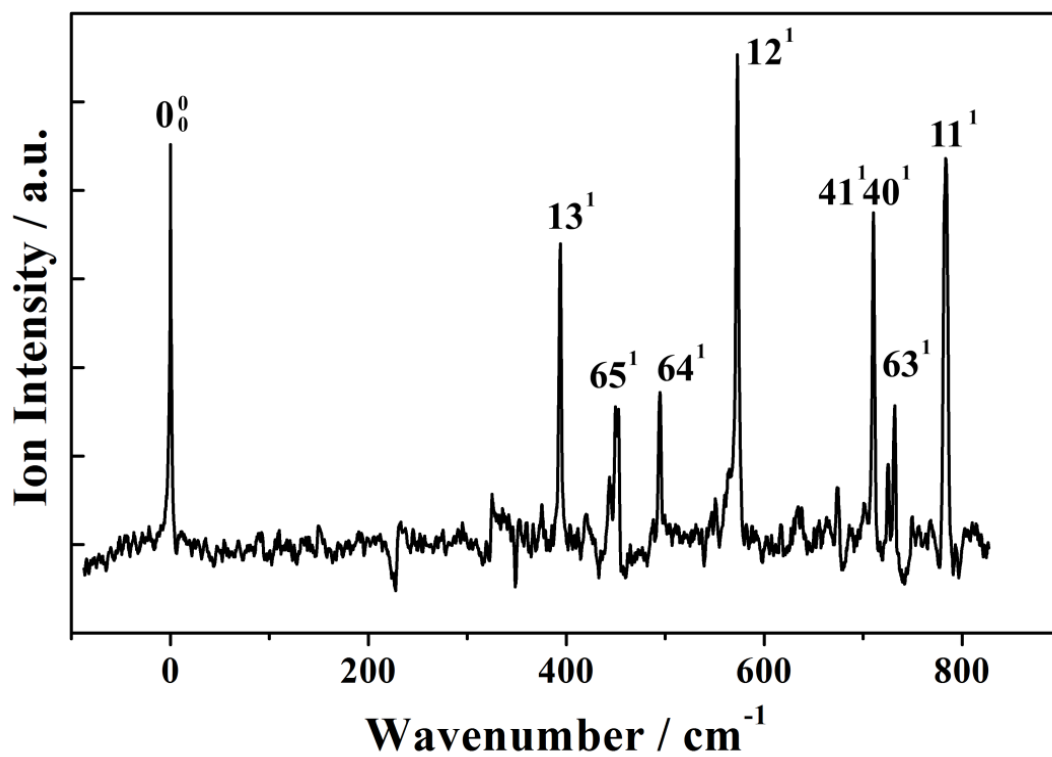


Figure 5.1 (1+1') REMPI spectrum of jet-cooled Pyrene. The spectrum is shifted by 27211 cm<sup>-1</sup> (the origin of the S<sub>1</sub>←S<sub>0</sub> transition) to emphasize the frequencies of the different vibrational levels of the S<sub>1</sub> state.

Table 5.1 Observed and calculated vibrational frequencies of the  $S_1$  state of pyrene

Experiment	Calculation*	Assignment	Symmetry
394	392	13 <sup>1</sup>	a <sub>g</sub>
450	448	65 <sup>1</sup>	b <sub>3g</sub>
495	501	64 <sup>1</sup>	b <sub>3g</sub>
573	567	12 <sup>1</sup>	a <sub>g</sub>
712	718	40 <sup>1</sup> 41 <sup>1</sup>	b <sub>1g</sub>
732	729	63 <sup>1</sup>	b <sub>3g</sub>
783	788	11 <sup>1</sup>	a <sub>g</sub>

\*A scaling factor of 0.9245 is included in the calculation result.

Pyrene is considered planar with  $D_{2h}$  symmetry (The definition of molecular axis is shown in Figure 5.4)<sup>v</sup>. Among its 72 normal modes, 13 belong to the  $a_g$  symmetry species allowed by the Franck-Condon principle in the  ${}^1B_{2u}(S_1) \leftarrow {}^1A_g(S_0)$  transition. Within the spectral range of our experiment, the three lowest  $a_g$  modes are observable and are assigned as modes 13 - 11. Since the energy of the  ${}^1B_{1u}(S_2)$  state is only  $\sim 4000 \text{ cm}^{-1}$  above that of the  $S_1$  state in gas phase and  $\sim 3000 \text{ cm}^{-1}$  in solid phase, some Franck-Condon forbidden  $b_{3g}$  modes can be activated by Herzberg-Teller vibronic coupling. The three  $b_{3g}$  modes shown in the spectrum are assigned as modes 65 - 63, in agreement with the fluorescence excitation spectra by Mangle and Topp in 1986 and Borisevich et al in 1995 and Baba et al in 2009.<sup>44,45,47</sup> However, a strong peak at  $712 \text{ cm}^{-1}$  has never been assigned before, and we think that it is most likely a combination of two  $b_{2g}$  modes 41 and 40. Based on our calculation, this combination is only  $6 \text{ cm}^{-1}$  from the experimental result. This assignment will be further confirmed from ZEKE in the following section.

#### 5.4.2 ZEKE spectroscopy

By scanning the ionization laser while setting the resonant laser at one of the intermediate states identified in the above REMPI experiment, we obtained

---

<sup>v</sup> The difference of axis result in different symmetry, species for the electronic states and the vibrational modes.

pulsed field ionization ZEKE spectra as shown in Figure 5.2. The assignment of the vibrational levels of the cation is noted by a superscript “+”. The identity of the vibrational level of the intermediate state for each ZEKE spectrum is labeled in the corresponding panel by a black dot. The experimental and theoretical values are shown in Table 5.2. The calculation was performed at the B3LYP/6-311G (d,p) level. Using a least-squares fitting procedure similar to that for the  $S_1$  state, a factor of 0.995 for the theoretical vibrational frequencies of the cation was obtained, after which the agreement between theory and experiment is reasonable. Limited by the linewidth of the resonant transitions and the pulsed electric field, the uncertainty of the experimental values of the ZEKE spectra is  $7 \text{ cm}^{-1}$ .

The ZEKE spectra are sparse, and each consists of no more than three peaks with similar intensities. Trace (a) was recorded via the origin of the  $S_1$  state, and the most intense peak corresponds to the origin of the cation. The adiabatic ionization potential is thus determined to be  $59888 \pm 7 \text{ cm}^{-1}$  ( $7.4064 \pm 0.0007 \text{ eV}$ ), taking into account the shift caused by the pulsed electric field. This value is  $155 \text{ cm}^{-1}$  higher than that determined by Hager and Wallace<sup>57</sup> using two-laser photoionization in 1988. This discrepancy might be caused by the extrapolation method in the previous paper. Although the same selection rule applies to both the REMPI and the ZEKE process, only mode 12 is observed in the ZEKE spectrum from the origin of the  $S_1$  state, while other Franck-Condon allowed and vibronic allowed bands observable in the REMPI experiment are missing in the ZEKE spectrum.

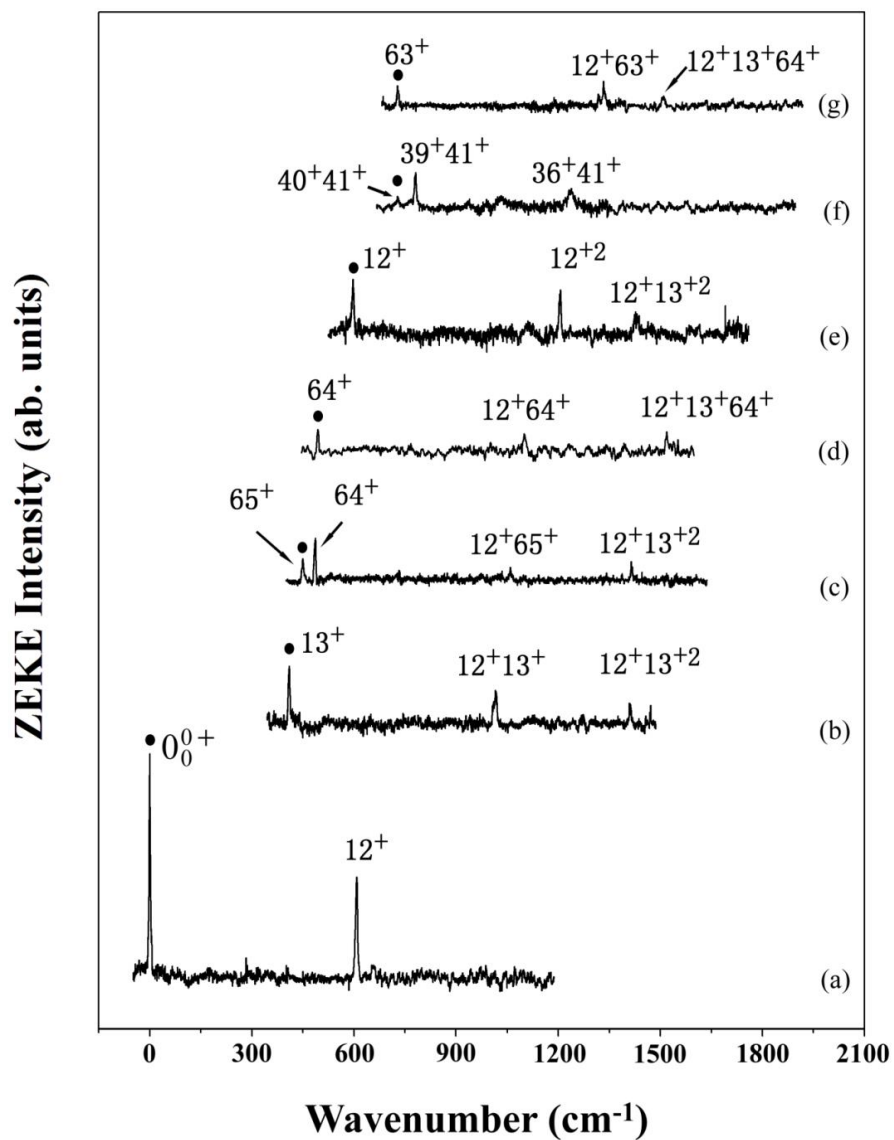


Figure 5.2 Two-color ZEKE spectra of pyrene recorded via seven vibrational levels of the  $S_1$  state as intermediate states: (a)  $0_0^0$ , (b)  $13^1$ , (c)  $65^1$ , (d)  $64^1$ , (e)  $12^1$ , (f)  $41^140^1$ , (g)  $63^1$ . The energy in the  $x$ -axis is relative to the ionization threshold at  $59888 \text{ cm}^{-1}$ . The assignment in the figure refers to the vibrational levels of the cation, and the corresponding vibrational level of the intermediate state is labeled by a black dot in each panel.

Table 5.2 Observed and calculated vibrational frequencies of pyrene cation

Intermediate level in the $S_1$ state							Cation	
$0_0^0$	$13_0^1$	$65_0^1$	$64_0^1$	$12_0^1$	$40_0^1 41_0^1$	$63_0^1$	Calculation*	Assignment
0							0	origin
	410						412	$13^+$
		451					457	$65^+$
		491	494				499	$64^+$
608				598			598	$12^+$
						728	738	$63^+$
					732		730	$40^+ 41^+$
					781		798	$39^+ 41^+$
	1014						1010	$12^+ 13^+$
		1056					1055	$12^+ 65^+$
			1099				1097	$12^+ 64^+$
				1206			1196	$12^{+2}$
					1240		1246	$36^+ 41^+$
						1333	1336	$12^+ 63^+$
	1413	1415		1427			1422	$12^+ 13^{+2}$
			1519			1510	1509	$12^+ 13^+ 64^+$

\*A scaling factor of 0.995 is included in the calculation result

Trace (e) shows the ZEKE spectrum of pyrene taken via the in-plane breathing mode 12 of the  $S_1$  state. In addition to the fundamental band, the second harmonic of the same mode is also observable, while  $12^{+3}$  is out of range of this observation window. A few other ZEKE spectra obtained via different vibrational levels of the  $S_1$  state also involve combinations with mode 12, including  $12^{+13^+}$ ,  $12^{+65^+}$ ,  $12^{+64^+}$ ,  $12^{+63^+}$ ,  $12^{+13^{+2}}$ , and  $12^{+13^+64^+}$ . In fact, the only spectrum that does not contain a combination band with mode 12 is trace (f) obtained via the combination of two  $b_{2g}$  modes. On the other hand, no combination bands are observable in trace (e), meaning that ionization via mode 12 does not activate any other mode.

Excitations in the vibronic modes 63 to 65 and out-of-plane modes 40 and 41 are largely preserved during ionization, but the resulting ZEKE spectra also contain additional combinations with mode 12. Among the three in-plane twisting modes of 63 to 65, mode 64 is the most prevalent, observable in the ZEKE spectra obtained via the other two  $b_{3g}$  intermediate vibronic levels.

The out-of-plane  $b_{2g}$  modes are only observable from their combination bands, and preservation of the vibrational excitation during ionization is inconsistent. Trace (f) consists of three combination bands with mode 41. The vibration of the intermediate level involves modes 40 and 41, but the corresponding combination band is barely observable in the ZEKE spectrum. Instead, two higher frequency modes of the same  $b_{2g}$  symmetry are observed. The facts that all modes

in the ZEKE spectrum can be assigned with confidence and that all modes are of  $b_{2g}$  symmetry further vindicate the assignment of the intermediate state.

Figure 5.3 shows the displacement vectors of the observed modes both in REMPI and ZEKE. All three  $a_g$  modes correspond to expansion/shrinkage of the molecular frame. In particular, mode 12 involves breathing in the vertical direction, mode 13 involves breathing in the horizontal direction, and mode 11 involves breathing of the two terminal horizontal rings. Mode 41 and mode 39 are out-of-plane waving modes along the long axis. They are similar to the  $b_{3g}$  modes we have observed in the ZEKE spectrum of pentacene.<sup>31</sup> If we define the length of the molecular long axis as  $L$ , the waving cycle of mode 41 is  $L/2$  and that of mode 39 is  $L/4$ , with a wave propagation vector along the long axis. Mode 40 is characteristic of peri-condensed PAHs, and its displacement vectors involve concurrent waving along both axes in the molecular plane. Mode 36 is basically CH out-of-plane waving.

In our previous work on ZEKE spectroscopy of substituted aromatic compounds,<sup>52-55</sup> we have used the degree of conservation of the vibrational excitation of the intermediate state as an indicator of the stability of the molecular frame from  $S_1$  to  $D_0$ . When the substituent is electron-rich, the cation exhibits negligible geometric change upon ionization, resulting in essentially diagonal Franck-Condon factors. The ZEKE spectra are dominated by one vibrational band corresponding to the same vibrational excitation of the intermediate  $S_1$  state. This

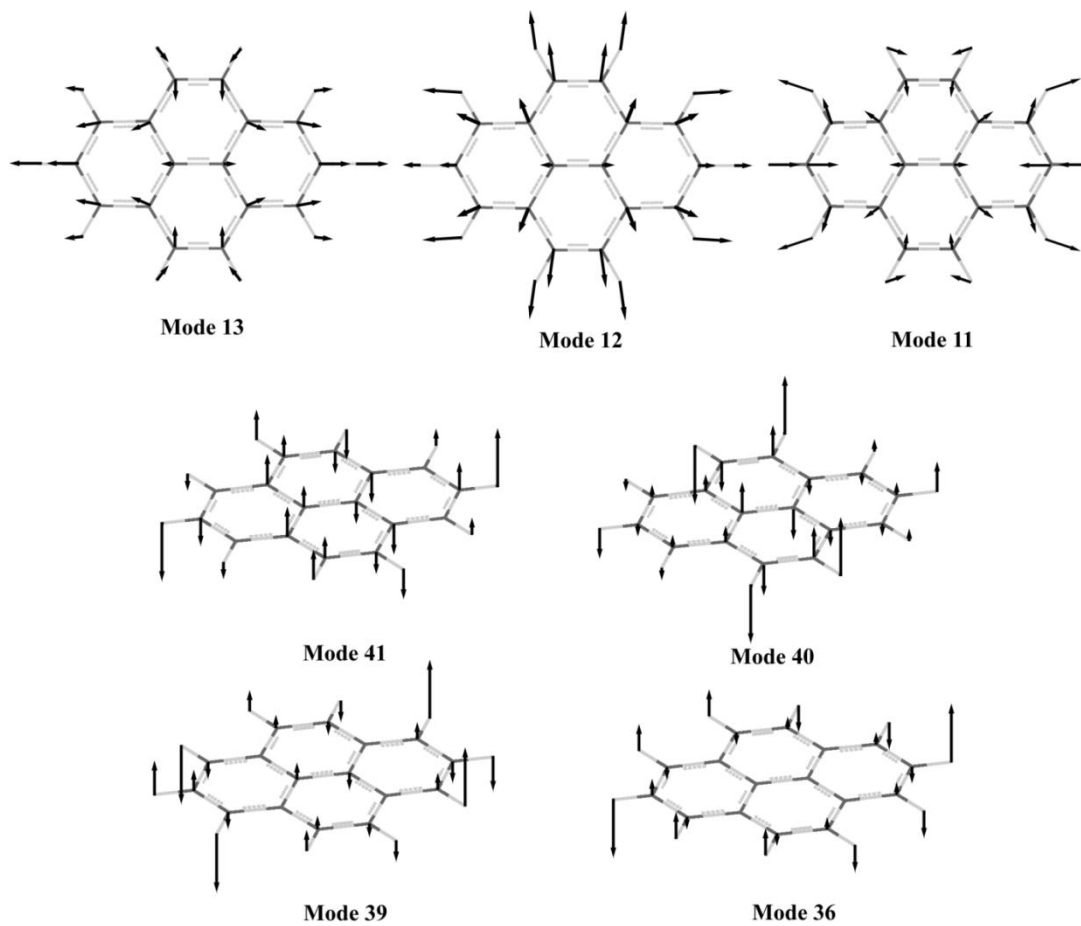


Figure 5.3 Displacement vectors for a few normal modes of pyrene.

propensity breaks down with electron-poor substituents,<sup>56</sup> and the resulting ZEKE spectra contain long progressions of modes related to skeletal rearrangements. The ZEKE spectra of pyrene seem to fall in between these two cases. The multiple fused rings have a substantial ability to absorb the positive charge of the cation, but they are less efficient than an electron rich substituent such as an amino group or a halogen atom.

## 5.5 Discussion

### 5.5.1 The nature of the $S_1$ state

The symmetry of the  $S_1$  state has been discussed most recently by Baba *et al*<sup>47</sup> based on fluorescence excitation and dispersed fluorescence spectra. However, some historical recount and some additional details are necessary for a comprehensive understanding. Our CIS calculation using the 6-311G(d,p) basis set has resulted in two closely spaced electronically excited states  $^1B_{1u}$  and  $^1B_{2u}$ . The energy order of the two states, however, is questionable. In previously reported calculations,<sup>46,49</sup> the  $^1B_{2u}$  state had a fairly weak oscillator strength with a transition dipole along the short axis, while the  $^1B_{1u}$  state had an oscillator strength 2 to 3 orders larger than that of the  $^1B_{2u}$  state, and its transition dipole was along the long axis. In Tanaka's work of electronic absorption of crystalline pyrene,<sup>48</sup> four excited states were reported. Further polarized excitation revealed that the  $S_1$  state had a transition dipole along the short axis, and the second excited state, about  $3000\text{ cm}^{-1}$

higher in energy, had a dipole along the long axis. The oscillator strength of the second state was also determined to be two orders of magnitude greater than that of the first one. These experimental results indicate that the  ${}^1B_{2u}$  state should be the lowest singlet excited state  $S_1$  while the  ${}^1B_{1u}$  state should be the  $S_2$  state. However, this order is opposite to most theoretical results obtained using different computational methods.<sup>46,49</sup> For example, Bito, Shida and Toru used four different methods,<sup>49</sup> and only two resulted in  ${}^1B_{2u}$  for  $S_1$ , and only MRSD-CI (multi-reference singles and doubles – configuration interaction) yielded both the same order and similar excitation energies as those from Tanaka<sup>48</sup> for the two excited states. The TDDFT (time-dependent DFT) method was also evaluated by Dierksen and Grimme,<sup>46</sup> and the resulting order of states was opposite to that of Tanaka. Our calculation at the [CIS/6-311G(d,p)] level resulted in a lower  ${}^1B_{1u}$  state than a  ${}^1B_{2u}$  state, again opposite to the experimental order of Tanaka.<sup>48</sup>

We then further compared the vibrational frequencies of the two electronic states with our experimental results from Table 5.1, taking into consideration that the experimental uncertainty in the transition frequencies is less than  $3\text{ cm}^{-1}$  for the one-photon resonant REMPI experiment. For the  ${}^1B_{2u}$  state, the corresponding  $R^2$  value was 0.9996 with a maximum deviation of  $6\text{ cm}^{-1}$ . On the other hand, for the  ${}^1B_{1u}$  state using the least-squares fitting procedure, a single scaling factor fit resulted in a  $R^2$  value of 0.9889 and a maximum deviation of  $23\text{ cm}^{-1}$ . If we choose to use two different scaling factors for the  $a_g$  and  $b_{3g}$  modes from the  ${}^1B_{1u}$  state, an

equally satisfactory comparison as that of Table 5.1 can also be achieved. In fact, Baba *et al*<sup>47</sup> did adopt two different scaling factors and rationalized their choice by invoking different interactions between the electronic states. However, if one scaling factor from the  ${}^1B_{2u}$  state can achieve the same level of agreement as that with two scaling factors from the  ${}^1B_{1u}$  state, it seems rational to adopt the choice of the former  ${}^1B_{2u}$  symmetry.

The molecular orbitals and energy level distribution from CIS/6-311G(d,p) are very similar to those from simple Hückel calculations, and for clarity, the relevant HOMO (-1) and LUMO (+1) orbitals from simple Hückel calculations are reproduced in Figure 5.4 together with the numbering scheme of the carbon atoms and the definition of molecular axis. Both HOMO and HOMO - 1 have three nodal planes, and both LUMO and LUMO + 1 have four nodal planes. The transition dipoles of LUMO  $\leftarrow$  HOMO and LUMO + 1  $\leftarrow$  HOMO - 1 are  $b_{1g} \times a_u = b_{1u}$  and  $b_{2g} \times b_{3u} = b_{1u}$ , both in the direction of the long axis, while those of the nearly degenerate pair LUMO  $\leftarrow$  HOMO - 1 and LUMO + 1  $\leftarrow$  HOMO are  $b_{2g} \times a_u = b_{2u}$  and  $b_{1g} \times b_{3u} = b_{2u}$ , with transition dipoles in the vertical direction along the short axis. The energies of both the vertical and horizontal transitions are similar, as implied by the distribution of nodal planes in the MOs. Based on the work of Callis,<sup>58</sup> the horizontal transitions are  $L_a$  in nature with  $B_{1u}$  symmetry, and the vertical transitions are  $L_b$  in nature with  $B_{2u}$  symmetry. The reversal in order of excited electronic states from calculation thus implies that the vertical transitions

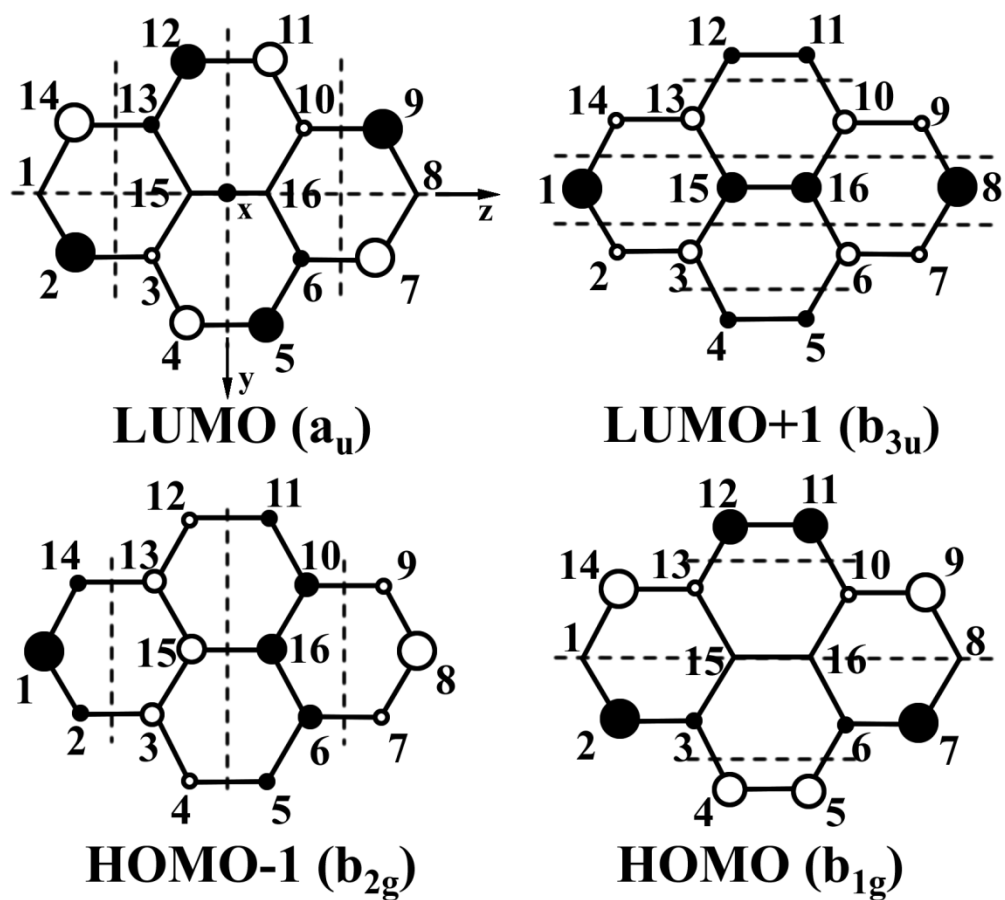


Figure 5.4 The HOMO-1, HOMO, LUMO and LUMO+1 of pyrene. The dashed lines mark the nodal planes based on a simple Hückel calculation.

LUMO  $\leftarrow$  HOMO - 1 and LUMO + 1  $\leftarrow$  HOMO correspond to the observed  $S_1 \leftarrow S_0$  transition. Our CIS calculation further reveals that the oscillator strength contains essentially equal contributions of the two  $L_b$  transitions. This is an extreme case of configuration interactions of nearly degenerate states.

The ambiguity in the order of electronic states is related to the size and class of the PAHs. In our previous studies of tetracene and pentacene,<sup>31,43</sup> the order of the excited states was unambiguous. The first excited state is almost a pure LUMO  $\leftarrow$  HOMO transition ( $L_a$ ) along the short axis, the same as that from our calculation. Typically neutral PAHs have three absorption band systems:  $\alpha$ , p, and  $\beta$ , as defined by Clar.<sup>59</sup> The  $L_a$  transition is the p-band in Clar's classification and the  $L_b$  transition is the  $\alpha$ -band, much weaker than the p band. Empirically, with the growing size of the aromatic molecule, both p- and  $\alpha$ -bands shift to the red, but the two transitions shift at different rates depending on the detailed molecular structure, and the resulting order of states adjusts accordingly.

### 5.5.2 Geometry and vibrational modes of the $S_1$ state

By setting the control key to root = 2 in the CIS/6-311G(d,p) calculation for the  ${}^1B_{2u}$  state, the resulting geometry parameters for the  $S_1$  state are listed in Table 5.3. In addition to our calculation result, the parameters from neutron diffraction of pyrene crystals are also listed in Table 5.3 for the  $S_0$  state.<sup>60</sup> Upon excitation to the  $S_1$  state, the most notable change is the shortened bond of C15-C16. From Figure

Table 5.3 Molecular geometry parameters of pyrene in the  $S_0$ ,  $S_1$ , and  $D_0$  states

	$S_0$		$S_1$	$D_0$
	Calculation	Experiment <sup>62</sup>		
Bond length				
C1-C2	1.39131	1.395	1.39462	1.39018
C2-C3	1.40210	1.406	1.39714	1.42101
C3-C4	1.43629	1.438	1.41948	1.41614
C4-C5	1.35848	1.367	1.36252	1.38221
C15-C16	1.42485	1.425	1.37626	1.41461
C3-C15	1.42633	1.430	1.44541	1.42262
Distance (Å)				
C4-C12	4.92126		4.90918	4.89357
C1-C8	7.03643		7.02547	7.06780

5.4, in the transition of LUMO  $\leftarrow$  HOMO - 1, the antibonding character between C15 and C16 in HOMO - 1 should be attenuated by the additional horizontal nodal plane in the LUMO, while in the transition of LUMO + 1  $\leftarrow$  HOMO, the additional bonding character in the LUMO + 1 between C15 and C16 should shrink the bond length upon excitation. It is interesting to also note that regardless of the changes in nodal planes, the overall size of the molecular frame remains similar upon electronic excitation and even ionization. This fact manifests the ability of the aromatic system in accommodating variations in electron density and charge.

Two other bonds are also affected by the electronic transition, although to a much lesser degree than that of C15 - C16. The bond length of C3 - C4 is shortened, while that of C3 - C15 is lengthened. The latter result is understandable for the LUMO + 1  $\leftarrow$  HOMO transition, with the addition of a nodal plane between C3 and C15. The C3 - C4 bond should be strengthened somewhat in the LUMO  $\leftarrow$  HOMO - 1 transition because of the higher electron density on C4 in the LUMO. In the meantime, its antibonding character should be attenuated in the LUMO + 1 because of the lower electron density on C4.

The changes in bond length are in agreement with the observed vibrational modes in the REMPI spectrum of Figure 5.1. We performed a Franck-Condon calculation<sup>61,62</sup> for the  $S_1 \leftarrow S_0$  transition using the program from Dr. Dongsheng Yang, and the resulting Franck-Condon factors for transitions to modes 13 to 11 are

5:7:1. This ratio underestimates the intensity of mode 11, but for modes 13 and 12, it is qualitatively correct.

### 5.5.3 Geometry and vibrational modes of the $D_0$ state

In the  $D_0 \leftarrow S_1$  transition, an electron is removed from  $S_1$  and the final cation geometry should only be affected by the final electron configuration. Since the HOMO and HOMO - 1 are nearly degenerate, and the final ionic state has an odd number of electrons, a Jahn-Teller-like effect might result in a larger separation in energies between the two orbitals, thereby resulting in a single electron configuration. This speculation agrees with the changes in the calculated bond length from  $S_0$  to  $D_0$  as listed in Table 5.3. The overall molecular length in the vertical direction represented by C4 - C12 is decreased, in agreement with the removal of an electron from an orbital with horizontal nodal planes, i. e. the HOMO. In addition, the bond length of C3 - C4 is shorter in  $D_0$ , in agreement with the fact that a nodal plane passes through the C3 - C4 bond in the HOMO. On the other hand, the overall horizontal dimension of the molecule represented by C1 - C8 is slightly larger in  $D_0$ , a result that could not be explained by the loss of an electron from the HOMO - 1. Elongations of both the C2 - C3 and C4 - C5 bonds are also contradictory to the removal of an electron from HOMO - 1. Thus although the  $S_1 \leftarrow S_0$  transition is essentially a complete mixture of two configurations in both the initial and final MOs, the electron configuration of the cation is almost exclusively (HOMO - 1)<sup>2</sup>(HOMO)<sup>1</sup>.

To understand the observed vibrational modes in ZEKE, however, we need to consider both  $(\text{HOMO} - 1)^2(\text{HOMO})^1 \leftarrow (\text{HOMO} - 1)^1(\text{HOMO})^2(\text{LUMO})^1$  and  $(\text{HOMO} - 1)^2(\text{HOMO})^1 \leftarrow (\text{HOMO} - 1)^2(\text{HOMO})^1(\text{LUMO} + 1)^1$ . The latter case is straightforward, involving only the removal of the LUMO + 1 electron. The decreased antibonding character in the vertical direction agrees with the activation of mode 12, i. e., stretching in the vertical direction. The former case involving a LUMO electron is more complicated, and a two step process is necessary to reach the final electron configuration  $(\text{HOMO} - 1)^2(\text{HOMO})^1$ . The removal of a horizontal nodal plane with the removal of the LUMO electron is also a mechanism of activating mode 12. Further relaxation for an electron from HOMO to HOMO - 1 involves changing all 3 vertical nodal planes into horizontal, a process essentially impossible to achieve due to the orthogonality of the two MOs. We therefore propose that ionization from the electron configuration  $(\text{HOMO} - 1)^1(\text{HOMO})^2(\text{LUMO})^1$  does not lead to the ground cationic state  $D_0$  and hence is not observable from the current ZEKE experiment.

The Mulliken charge distribution for the  $D_0$  state is calculated with the Gaussian 03 suite. We placed the net charges on the peripheral hydrogen atoms to the adjacent ring, and divided the charges on the shared carbon atoms to the conjoint rings. About 60% of the positive charge is located on the rings along the long axis, while 40% is on the rings along the short axis. This charge distribution is complementary to the electron density distribution of the HOMO. The opposite is

true for the HOMO - 1, with a much lower concentration of positive charges (about 30%) located on the longitudinal rings. This result is also supportive of our assessment of the single electron configuration (HOMO - 1)<sup>2</sup>(HOMO)<sup>1</sup> for the  $D_0$  state. The unequal distribution of charges on the two unique types of rings can be largely attributed to the loss of electron density on carbons 2, 7, 9 and 14 upon ionization. This result is not surprising from the point of view of basic organic chemistry: these carbon atoms are known to be the most reactive and most likely sites for substitution reactions.

It is worth noting that no previous experimental information of pyrene cation is available in the frequency region below 500 cm<sup>-1</sup>, largely due to practical difficulties in FIR spectroscopy. Thus even just for calibration and scaling purposes, ZEKE is of considerable value, particularly for predictions of IR active modes in the FIR region. Governed by the selection rule of ZEKE spectroscopy, no IR active mode has been observed in the current work. Consequently, we cannot make any comparisons with previous experimental and theoretical studies even in the region above 500 cm<sup>-1</sup>.<sup>23,37-40</sup> This factor further manifests the complementary nature of ZEKE to other direct single photon processes such as matrix isolation spectroscopy or infrared multiphoton dissociation.

#### 5.5.4 Comparisons with cata-condensed PAHs

Based on our study of cata-condensed PAHs of tetracene and pentacene,<sup>31,43</sup> the frequency of the  $a_g$  longitudinal stretching mode shifts to lower values with the increase of the number of aromatic rings. The longitudinal dimension of the carbon skeleton and the observed frequencies of the longitudinal stretching mode for a few PAHs are plotted in Figure 5.5. The error bars in the figure represent reported experimental uncertainties.<sup>31,41-43,63</sup> All listed PAHs have  $D_{2h}$  symmetry except for benzene which has  $D_{6h}$  symmetry. A least-squares regression of the data points in Figure 5.5 reveals a reciprocal relationship between the frequency and the molecular length, with a  $R^2$  of 0.9918. The trend of red shift is thus not limited to cata-condensed PAHs, and the peri-condensed pyrene is no exception. It would be interesting to expand the current investigation to other peri-condensed PAHs for further in-depth studies.

The observation of the  $b_{2g}$  out-of-plane waving modes 41 and 39 of pyrene implies some degree of corrugation of the molecular plane. In the polyacene series, this type of out-of-plane waving mode was only observed in pentacene.<sup>31</sup> Although the length of pyrene is close to but slightly smaller than that of anthracene, the expansion of the molecular frame in the orthogonal direction seems to offer extra flexibility in the molecular frame, allowing the activation of the  $b_{2g}$  modes along both the long and short axes.

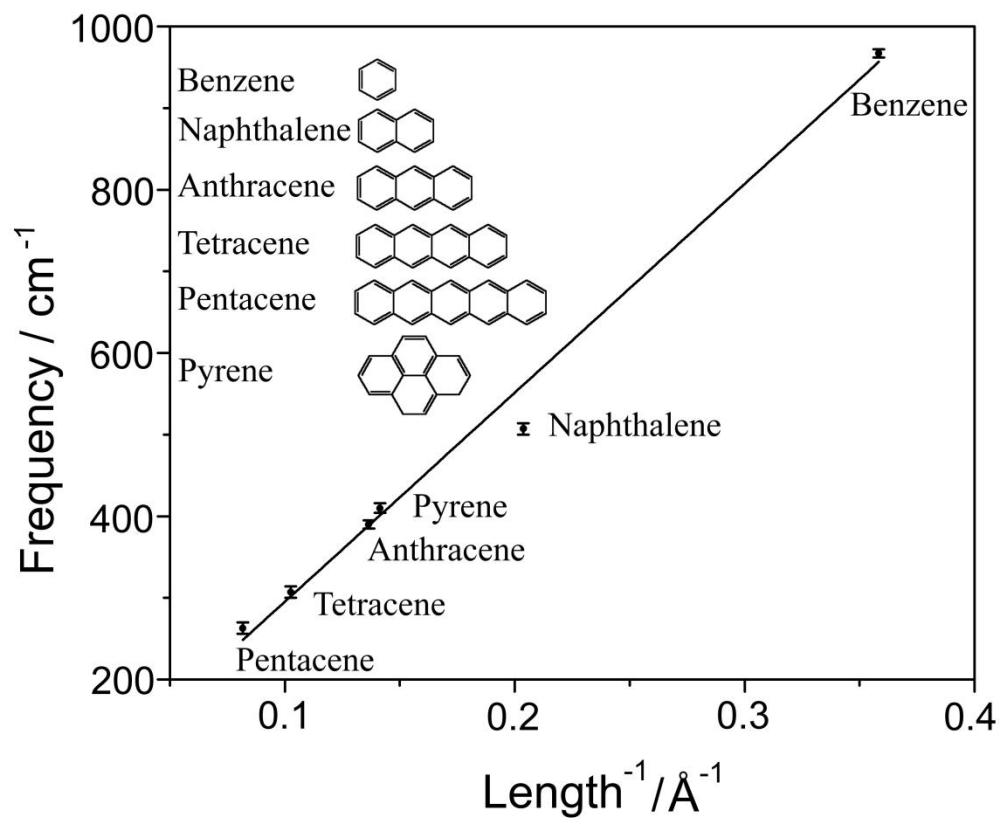


Figure 5.5 Frequencies of the longitudinal stretching mode vs. the inverse of the length of a PAH molecule including benzene, naphthalene, anthracene, tetracene, pentacene and pyrene.<sup>31,37-39,61</sup> The error bars are reported experimental uncertainties.

Typically DFT calculations provide reliable vibrational frequency information for the cation, as demonstrated in our own work on cata-condensed PAHs and a series of small benzene derivatives.<sup>31,43,52,-56</sup> In the case of pyrene, the maximum deviation is  $\sim 21\text{cm}^{-1}$  without any scaling factor. The scaling factor of 0.995 further reduces the deviation to  $17\text{ cm}^{-1}$ . This level of agreement is less than impressive. In addition, as mentioned in our previous publication,<sup>31</sup> the agreement between experiment and theory in ZEKE intensity based on Franck-Condon factors is still qualitatively unsatisfactory. Reliability in theoretical calculations for the ground state of the cation is crucial for astrophysical modeling, since IR active modes not typically observable in ZEKE play important roles for spectroscopic surveys and modeling of energy and chemical balances in the universe. The current results further illustrate the need for experimental data, both in terms of astrophysical modeling and further improvements in DFT calculations.

## 5.6 Conclusion

Spectroscopic properties of the electronically excited and ionic states of pyrene have been studied using 1+1' two-color REMPI and two-color ZEKE. Although the small peri-condensed PAH is not expected to have pronounced non-rigidity, pyrene shows the character of large PAHs in both the nature of the electronic transition and vibronic coupling. The first excited electronic state is  $L_b$  in nature, and vibronic bands due to Herzberg-Teller coupling are only slightly

weaker in intensity than those of Franck-Condon allowed  $a_g$  modes. Unique to the peri-condensed PAHs, some of the observed out-of-plane waving modes have a 2-dimensional evolution pattern, spreading in both directions of the molecular plane. For the Franck-Condon allowed  $a_g$  mode corresponding to longitudinal stretching of the molecular frame, we have established a close correlation between frequency and molecular shape and size, and this information can assist with astrophysical studies of PAH related subjects.

Simple Hückel calculations offer a simplistic view of the related MOs and distribution of nodal planes. This type of qualitative information is helpful in understanding the change in geometry and activation of vibrational modes upon electronic excitation and ionization. However, even with CIS and TDDFT, the order of the excited electronic state from calculation is still questionable, and near degeneracy of MOs and electronic states due to high symmetry should serve as a warning in the interpretation of theoretical results. The extensive configuration interaction in the first two electronically excited states of pyrene is expected to persist for larger PAHs with similar symmetry, and detailed analysis of vibrational and polarization spectroscopy is necessary for the symmetry assignment of the related electronic states.

## **5.7 Acknowledgements**

This work is supported by the National Aeronautics and Space Administration under award No. NNX09AC03G. Acknowledgment is made to the Donors of The Petroleum Research Fund, administered by the American Chemical Society, for partial support of this research.

## 5.8 References

- (1) Parr, R. *The quantum theory of molecular electronic structure*; W. A. Benjamin: New York, 1964.
- (2) Sami, S.; Faisal, M.; Huggett, R. *J. Mar. Biol.* **1992**, *113*, 247-252.
- (3) Smith, L. E.; Denissenko, M. F.; Bennett, W. P.; Li, H.; Amin, S.; Tang, M.-S.; Pfeifer, G. P. *J. Natl. Cancer Inst.* **2000**, *92*, 803-811.
- (4) Kriek, E.; Rojas, M.; Alexandrov, K.; Bartsch, H. *Mutat. Res. Fundam. Mol. Mech. Mugag.* **1998**, *400*, 215-231.
- (5) Harvey, R. G. *Polycyclic aromatic hydrocarbons: chemistry and carcinogenicity*; Cambridge University Press: London, 1991.
- (6) Baude, P. F.; Ender, D. A.; Haase, M. A.; Kelley, T. W.; Muyres, D. V.; Theiss, S. D. *Appl. Phys. Lett.* **2003**, *82*, 3964-3966.
- (7) Knipp, D.; Street, R. A.; Völkel, A.; Ho, J. *J. Appl. Phys.* **2003**, *93*, 347-355.
- (8) Br échignac, P.; Pino, T.; Boudin, N. *Spectrochim. Acta, Part A* **2001**, *57*, 745-756.
- (9) Salama, F.; Galazutdinov, G. A.; Krelowski, J.; Allamandola, L. J.; Musaev, F. A. *Astrophys. J.* **1999**, *526*, 265-273.
- (10) Bernstein, M. P.; Dworkin, J. P.; Sandford, S. A.; Cooper, G. W.; Allamandola, L. J. *Nature* **2002**, *416*, 401-403.
- (11) Wakeham, S. G.; Schaffner, C.; Giger, W. *Geochim. Cosmochim. Acta* **1980**, *44*, 415-429.
- (12) Shock, E. L.; Schulte, M. D. *Nature* **1990**, *343*, 728-731.
- (13) Allamandola, L. J.; Tielens, A. G. G. M.; Barker, J. R. *Astrophys. J.* **1985**, *290*, L25-L28.
- (14) L éger, A.; Puget, J., L. *Astron. Astrophys.* **1984**, *137*, L5-L8.
- (15) Mallocci, G.; Mulas, G.; Benvenuti, P. *Astron. Astrophys.* **2003**, *410*, 623-637.
- (16) Mulas, G.; Mallocci, G.; Benvenuti, P. *Astron. Astrophys.* **2003**, *410*, 639-648.
- (17) Peeters, E.; Allamandola, L. J.; Hudgins, D. M.; Hony, S.; Tielens, A. G. G. M. *Astron. Soc. Pac. Conf. Ser.* **2004**, *309*, 141-162.
- (18) Li, A. PAHs in comets: An overview. In *Deep impact as a world observatory event: Synergies in space, time, and wavelength*; Kaufl, H. U., Siebenmorgen, R., Moorwood, A. F. M., Eds.; Springer: Berlin, 2009; pp 161-175.
- (19) Rhee, Y. M.; Lee, T. J.; Gudipati, M. S.; Allamandola, L. J.; Head-Gordon, M. *Proc. Natl. Acad. Sci. U. S. A.* **2007**, *104*, 5274-5278.
- (20) Langhoff, S. R. *J. Phys. Chem.* **1996**, *100*, 2819-2841.
- (21) Zhang, K.; Guo, B.; Colarusso, P.; Bernath, P. F. *Science* **1996**, *274*, 582-583.
- (22) Joblin, C.; Bern é O.; Simon, A.; Mulas, G. *arXiv:0904.3185* **2009**.
- (23) Hudgins, D. M.; Allamandola, L. J. *J. Phys. Chem.* **1995**, *99*, 3033-3046.
- (24) Hudgins, D. M.; Allamandola, L. J. *J. Phys. Chem.* **1995**, *99*, 8978-8986.
- (25) Hudgins, D. M.; Allamandola, L. J. *J. Phys. Chem. A* **1997**, *101*, 3472-3477.

- (26) Hudgins, D. M.; Sandford, S. A. *J. Phys. Chem. A* **1998**, *102*, 353-360.
- (27) Hudgins, D. M.; Sandford, S. A. *J. Phys. Chem. A* **1998**, *102*, 344-352.
- (28) Hudgins, D. M.; Sandford, S. A. *J. Phys. Chem. A* **1998**, *102*, 329-343.
- (29) Parisel, O.; Berthier, G.; Ellinger, Y. *Astron. Astrophys.* **1992**, *266*, L1-L4.
- (30) Schlag, E. W. *ZEKE spectroscopy*; Cambridge University Press: London, 1998.
- (31) Zhang, J.; Han, F.; Li, A.; Kong, W. *Astrophys. J.* **2010**, *715*, 485-492.
- (32) Draine, B. T.; Li, A. *Astrophys. J.* **2001**, *551*, 807-824.
- (33) Draine, B. T.; Li, A. *Astrophys. J.* **2007**, *657*, 810-837.
- (34) Li, A.; Draine, B. T. *Astrophys. J.* **2001**, *554*, 778-802.
- (35) Li, A.; Draine, B. T. *Astrophys. J.* **2002**, *576*, 762-772.
- (36) Li, A. and Lunine, J. I. *Astrophys. J.* **2003**, *594*, 987-1010.
- (37) Cockett, M. C. R.; Kimura, K. *J. Chem. Phys.* **1994**, *100*, 3429-3441.
- (38) Cockett, M. C. R.; Ozeki, H.; Okuyama, K.; Kimura, K. *J. Chem. Phys.* **1993**, *98*, 7763-7772.
- (39) Zhang, J.; Pei, L.; Kong, W. *J. Chem. Phys.* **2008**, *128*, 104301.
- (40) Baba, M.; Saitoh, M.; Kowaka, Y.; Taguma, K.; Yoshida, K.; Semba, Y.; Kasahara, S.; Yamanaka, T.; Ohshima, Y.; Hsu, Y.-C.; Lin, S. H. *J. Chem. Phys.* **2009**, *131*, 224318.
- (41) Dierksen, M.; Grimme, S. *J. Chem. Phys.* **2004**, *120*, 3544-3554.
- (42) Mangle, E. A.; Topp, M. R. *J. Phys. Chem.* **1986**, *90*, 802-807.
- (43) Tanaka, J. *Bull. Chem. Soc. Jpn.* **1965**, *38*, 86-102.
- (44) Bito, Y.; Shida, N.; Toru, T. *Chem. Phys. Lett.* **2000**, *328*, 310-315.
- (45) Joblin, C.; d'Hendecourt, L.; L' ger, A.; D'fourneau, D. *Astron. Astrophys.* **1994**, *281*, 923-936.
- (46) Oomens, J.; Van Rooij, A. J. A.; Meijer, G.; von Helden, G. *Astrophys. J.* **2000**, *542*, 404-410.
- (47) Szczepanski, J.; Vala, M. *Astrophys. J.* **1993**, *414*, 645-655.
- (48) Kim, H. S.; Wagner, D. R.; Saykally, R. J. *Phys. Rev. Lett.* **2001**, *86*, 5691
- (49) Vala, M.; Szczepanski, J.; Pauzat, F.; Parisel, O.; Talbi, D.; Ellinger, Y. *J. Phys. Chem.* **1994**, *98*, 9187-9196
- (50) Gaussian 03, Revision E.01, Frisch, M. J., *et. al.* Gaussian, Inc., Wallingford CT, 2004.
- (51) Hager, J. W.; Wallace, S. C. *Anal. Chem.* **1988**, *60*, 5-10.
- (52) He, Y.; Wu, C.; Kong, W. *J. Chem. Phys.* **2004**, *121*, 8321-8328.
- (53) He, Y.; Wu, C.; Kong, W. *Chem. Phys. Lett.* **2004**, *391*, 38-43.
- (54) He, Y.; Wu, C.; Kong, W. *J. Chem. Phys.* **2004**, *121*, 3533-3539.
- (55) Wu, C.; He, Y.; Kong, W. *Chem. Phys. Lett.* **2004**, *398*, 351-356.
- (56) He, Y.; Kong, W. *J. Chem. Phys.* **2006**, *124*, 2043061.
- (57) Callis, P. R. *J. Chem. Phys.* **1983**, *78*, 16-22.
- (58) Clar, E. *Polycyclic hydrocarbons*; Academic Press: London, 1964.
- (59) Berces, A.; Zgierski, M. Z.; Yang, D.-S. *Computational molecular spectroscopy*; John Wiley & Sons: New York, 2000.

- (60) Yang, D.-S.; Zgierski, M. Z.; Rayner, D. M.; Hackett, P. A.; Martinez, A.; Salahub, D. R.; Roy, P.-N.; Carrington, T. *J. Chem. Phys.* **1995**, *103*, 5335-5342.
- (61) Kwon, C. H.; Kim, H. L.; Kim, M. S. *J. Chem. Phys.* **2003**, *119*, 215-223.
- (62) Hazell, A. C.; Larsen, F. K.; Lehmann, M. S. *Acta Crystallogr., Sect. B: Struct. Crystallogr. Cryst. Chem.* **1972**, *28*, 2977-2984.

**Zero kinetic energy photoelectron spectroscopy of benzo[*g,h,i*]perylene**

Jie Zhang, Fangyuan Han, and Wei Kong\*

*Department of Chemistry, Oregon State University, Corvallis, Oregon 97331-4003*

In preparation

---

\* To whom correspondence should be addressed.

E-mail: Wei.Kong@oregonstate.edu, Phone: 541-737-6714. Fax: 541-737-2062

## Chapter 6 Zero kinetic energy photoelectron spectroscopy of

### Benzo[*g,h,i*]perylene

#### 6.1 Abstract

We report zero kinetic energy photoelectron (ZEKE) spectroscopy of benzo[*g,h,i*]perylene (BghiP) via resonantly enhanced multiphoton ionization (REMPI). Our analysis concentrates on several vibrational modes of both the first excited state and the ground cationic state. Extensive vibronic coupling due to a nearby second electronically excited state is manifested through strong Franck-Condon forbidden bands in the REMPI spectrum. In addition, all observed bands are IR active, establishing the role of ZEKE spectroscopy in mapping out far infrared bands for astrophysical applications. The intensity distribution of vibronic bands also offers an indirect glimpse of the geometric changes of the molecular frame upon electronic excitation and ionization. The charge distribution of the resulting cation correlates with the reactivity of the different sites known to organic chemistry.

## 6.2 Introduction

Polycyclic aromatic hydrocarbons (PAH) are a group of over 100 different compounds distributed in the environment, in comet tails, and perhaps in the outer space.<sup>1</sup> Environmental PAHs are formed during incomplete combustion of organic substances and are related to environmental toxicity and carcinogenicity.<sup>2,3</sup> In astrophysics, PAHs have been observed in a wide range of Galactic and extragalactic regions.<sup>4</sup> In addition, neutral and ionic PAHs are considered promising candidates for the interstellar absorption and emission bands, including the unidentified infrared (UIB) emission bands.<sup>4-11</sup> The PAHs are further suggested to be related to the origin of life via the formation of primitive organic molecules including amino acids in the pre-DNA world.<sup>12-15</sup>

A variety of techniques have been explored for PAH identification including photoionization spectroscopy<sup>16</sup>, cavity ringdown<sup>17</sup>, and infrared absorption or emission spectroscopy.<sup>18</sup> Unfortunately, astrophysical PAHs has proven difficult to identify despite of extensive efforts in space explorations and laboratory astrophysics. One of the proposals to resolve this issue in recent years is to expand the spectroscopic investigation into the far infrared (FIR) and to include ionic PAH species. The FIR region is related to the skeletal motion of the whole molecular frame, hence it is representative of the size of the molecule.<sup>10,19,20</sup> Given the abundant radiation sources and the low particle density in the outer space, both cations and anions may have significant concentrations in the interstellar medium.

The FIR region was once considered “no man’s land” because of the low sensitivity of most detectors on board of space observatories and in laboratories. Moreover, laboratory experiments in the FIR are further challenged by the lack of adequate light sources and the achievable low ion densities. Fortunately, the technique of zero kinetic energy photoelectron (ZEKE) spectroscopy offers an indirect solution to these challenges in laboratory astrophysics.<sup>21,22</sup> ZEKE is known for its high resolution (on the order of ~100 kHz) of cation rovibrational spectroscopy.<sup>23</sup> The high Rydberg states in ZEKE are longer lived when they are associated with low vibronic states of the cation, which makes it particularly suitable for studies of low frequency vibrational modes. By detecting electrons from pulsed field ionization in ZEKE spectroscopy via multiphoton excitation, both the light source and the detector problems in typical FIR and sub-millimeter wave experiments can be avoided. Controlled by the Franck-Condon principle, the vibrational modes from ZEKE are different from those governed by single photon vibrational transitions, and in some cases the information from ZEKE could not be directly compared with spectra obtained from a space exploration. However, vibronic coupling has proven a possible mechanism to access IR allowed bands, and frequency calibration and hence determination of scaling factors even for the forbidden modes is crucial for theoretical modeling in the FIR. In addition, IR forbidden modes are needed in modeling the energy balance in the interstellar medium and in modeling PAH emissions with high internal temperatures.<sup>4,24-26</sup>

Benzo[*g,h,i*]perylene, also known as 1,12-benzoperylene, is a peri-condensed PAH, as shown in Figure 6.1. Its first two excited states have been widely studied both experimentally and theoretically in the gas phase and in the solution phase,<sup>27-32</sup> and matrix isolation spectroscopy of the cation in argon matrix<sup>33</sup> and in solid H<sub>2</sub>O<sup>34</sup> has been reported in the mid-IR and near-IR region from 600 to 1600 cm<sup>-1</sup>. However, no report of the cation vibrational spectroscopy in the FIR range is available. In this paper, we report two-color two photon REMPI and ZEKE spectroscopy of BghiP. We present detailed spectroscopic analysis for the vibrational levels of the first electronically excited state (*S*<sub>1</sub>) and the ground cationic state (*D*<sub>0</sub>). Additional insights can be obtained from the results of *ab initio* and density functional calculations. Structural changes due to electronic excitation and ionization will be elucidated from the observed active vibrational modes and from comparisons between the REMPI and ZEKE spectra.

### 6.3 Experimental setup

The experimental apparatus is a differentially pumped molecular beam machine, with the detection chamber enclosed inside the source chamber<sup>22,35</sup>. A time-of-flight mass spectrometer in the detection chamber also serves as the pulsed field ionization zero kinetic energy photoelectron spectrometer.<sup>22</sup> The sample benzo[*g,h,i*]perylene (Aldrich) was housed and heated to 250 °C in the pulsed valve located in the source chamber to achieve sufficient vapor pressure. The vapor was

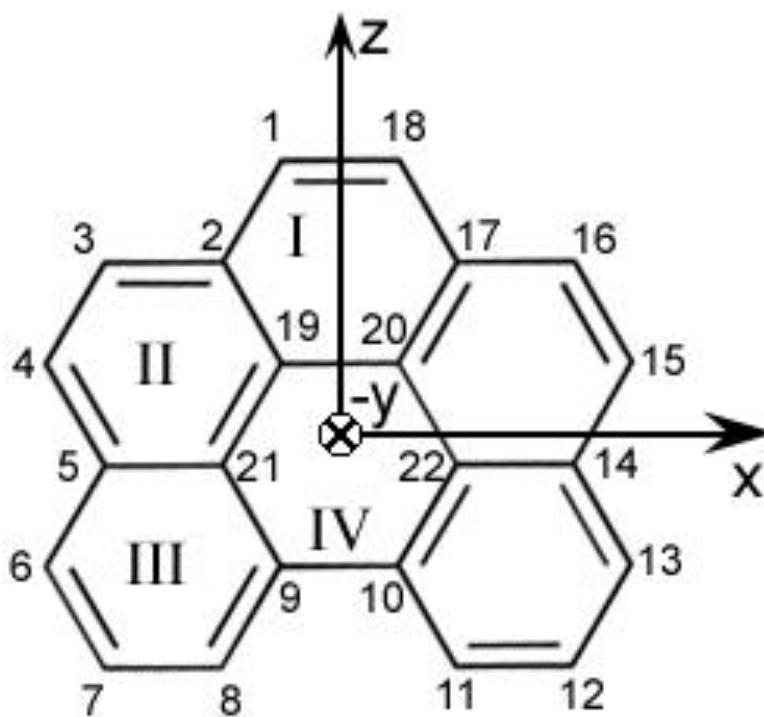


Figure 6.1. Structure of Benzo[*g,h,i*]perylene and orientation of molecular axes.

seeded in 400 torr of argon and co-expanded into vacuum through a pulsed valve with a 1 mm orifice. After passing through a 2 mm skimmer, the cooled sample reached the detection chamber for laser excitation and ionization. The laser systems for the REMPI experiment included two Nd:YAG (Spectra Physics, GCR 190 and Spectra Physics, GCR 230) pumped dye lasers (Laser Analytical System, LDL 20505 and Laser Analytical Systems, LDL 2051). The pump laser in the 394-383 nm range, obtained from the dye laser system (Exalite 389), had a pulsed energy of 1.5 mJ/pulse with a bandwidth of  $0.5 \text{ cm}^{-1}$ . The ionization laser in the 300-309 nm range from the frequency-doubled output of the other dye laser (Rhodamine 610 and sulforhodamine 640) had a pulse energy of 1 mJ/pulse with a band width of  $0.3 \text{ cm}^{-1}$ . The absolute wavelength of each laser was calibrated using an iron hollow-cathode lamp filled with neon. The pump laser and ionization laser were set to counter-propagate, and the light path, the flight tube, and the molecular beam were mutually perpendicular. The relative timing among the three laser pulses was controlled by two delay generators (Stanford Research, DG 535), and the optimal signal was obtained under temporal overlap between the pump and ionization lasers. In the ZEKE experiment, molecules excited to high Rydberg states were allowed to stay for 1 - 2  $\mu\text{s}$  in the presence of a constant DC spoiling field of  $\sim 1 \text{ V/cm}$ , after which ionization and extraction was achieved by a pulsed electric field of  $\sim 5 \text{ V/cm}$ .

Gaussian 03 suite<sup>36</sup> was used to optimize the molecular structure and to obtain vibrational frequencies for assignment of the observed vibronic structures from REMPI and ZEKE. For the ground state of the neutral and the cationic state, density functional theory (DFT) calculations using the B3LYP functional were performed with the 6-311G (d,p) basis set. The excited state  $S_1$  was calculated at the configuration interaction singles (CIS) level using the 6-311G (d,p) basis set. The CIS is adopted because of the size of the molecule and our computational resources. In addition, we have also used the same method for other PAHs and a few benzene derivatives with satisfactory results.<sup>21,22,35,37-41</sup> The resulting vibrational frequencies were scaled by a factor of 0.9191, the choice of which will be discussed in the following section. For the  $D_0$  state, no scaling factor was used.

## 6.4 Results

### 6.4.1 Two-color 1+1' REMPI spectroscopy

The two-color 1+1' REMPI spectrum of BghiP near the origin of the  $S_1 \leftarrow S_0$  electronic transition is displayed in Figure 6.2. The ionization laser was set at 300 nm and was temporally overlapped with the scanning resonant laser. The peak at  $25,207 \pm 3 \text{ cm}^{-1}$  is assigned as the origin band, which agrees with the absorption study of  $25,027.1 \pm 0.2 \text{ cm}^{-1}$  by Rouill *et al.*<sup>31</sup> Other observed vibronic transitions are listed in Table 6.1. The labeling of each vibrational mode is based on

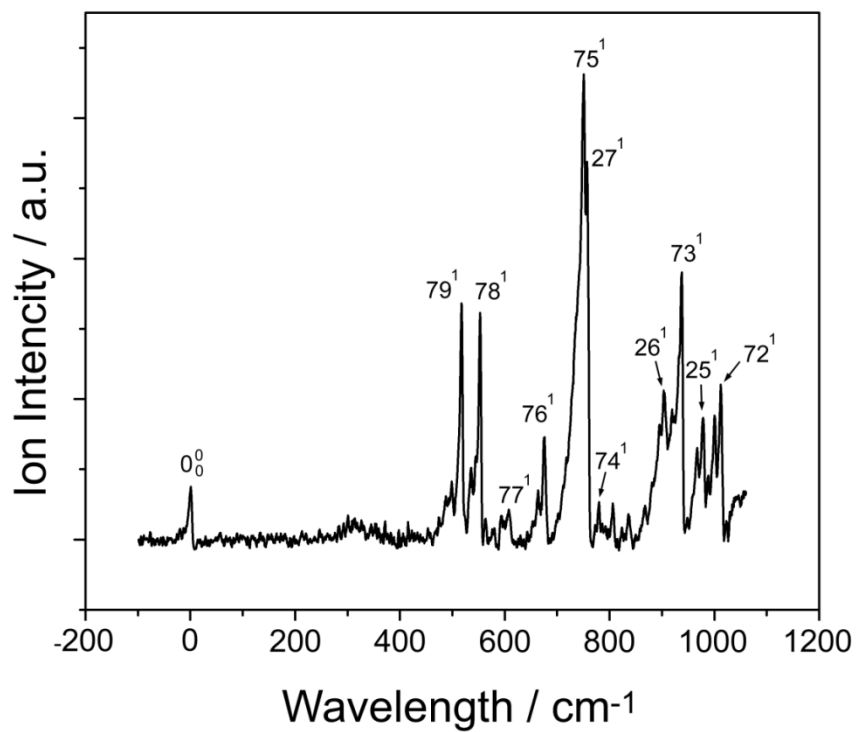


Figure 6.2. (1+1') REMPI spectrum of jet-cooled Benzo[*g,h,i*]perylene. The spectrum is shifted by 25207 cm<sup>-1</sup> (the origin of the  $S_1 \leftarrow S_0$  transition) to emphasize the frequencies of the different vibrational levels of the  $S_1$  state.

Table 6.1. Observed and calculated vibrational frequencies of the  $S_1$  state of benzo[*g,h,i*]perylene

REMPI/ cm <sup>-1</sup>	Cal*	Assignment	In He			absorption spectrum	Assignment	Cal
			droplet/ cm <sup>-1</sup>	assignment	Cal			
519	520	79 <sup>1</sup> (3b <sub>1</sub> )	517.3	3b <sub>1</sub>	504.9	517.5	3b <sub>1</sub>	509.1
552	555	78 <sup>1</sup> (4b <sub>1</sub> )	552.6	4b <sub>1</sub>	533.7	552.7	4b <sub>1</sub>	533.2
610	613	77 <sup>1</sup> (5b <sub>1</sub> )	611.2	5b <sub>1</sub>	603.4			
675	670	76 <sup>1</sup> (6b <sub>1</sub> )	676.1	6b <sub>1</sub>	664.7			
750	756	75 <sup>1</sup> (7b <sub>1</sub> )	752.5	7b <sub>1</sub>	759.5	749.7	7b <sub>1</sub>	749.9
757	754	27 <sup>1</sup> (7a <sub>1</sub> )	760.1			757.1	8b <sub>1</sub>	789.3
780	778	74 <sup>1</sup> (8b <sub>1</sub> )	779.8	3b <sub>1</sub> +1a <sub>1</sub>	777.2			
902	900	26 <sup>1</sup> (8a <sub>1</sub> )	903.6	9b <sub>1</sub>	905.1			
937	936	73 <sup>1</sup> (9b <sub>1</sub> )	936.6	3b <sub>1</sub> +3a <sub>1</sub>	950.1	937.1	9b <sub>1</sub>	908.2
978	973	25 <sup>1</sup> (9a <sub>1</sub> )	978.4	4b <sub>1</sub> +3a <sub>1</sub>	978.9			
1000	1000	78 <sup>1</sup> 31 <sup>1</sup> (4b <sub>1</sub> +3a <sub>1</sub> )	1001.1	4b <sub>1</sub> +4a <sub>1</sub>	995.5			
1012	1009	72 <sup>1</sup> (10b <sub>1</sub> )	1013.1	10b <sub>1</sub>	1025.2	1012.8	10b <sub>1</sub>	1010.6

\* A scaling factor of 0.9191 is included in the calculation result.

spectroscopic conventions, i. e. by using consecutive numbers in reference to the symmetry species and the frequency in decreasing order. It is worth noting that different definitions of the molecular axes result in different symmetry species for both the electronic state and the vibrational modes, and hence different numbering designation of the normal modes. For clarity, the molecular axis of this work is shown in Figure 6.1 and in parentheses, we also list another set of numbering scheme adopted in two previous studies, one in superfluid helium nanodroplet<sup>28</sup> and the other in cavity ring-down laser absorption spectroscopy<sup>31</sup>. Due to the fact that vibrational frequencies generated by *ab initio* calculations are usually too high, we used a least-squares linear regression method to match with the experimental data. The resulting scaling factor is 0.9186 with a coefficient of determination  $R^2 = 0.9996$ . In Table 6.1, experimental data and assignment from helium nanodroplet studies and cavity ring-down laser absorption spectroscopy are also presented.

All the observed vibrational modes can be assigned as either  $a_1$  or  $b_1$  symmetry species. BghiP has 33  $a_1$  modes allowed by the Franck-Condon principle in the  ${}^1A_1(S_1) \leftarrow {}^1A_1(S_0)$  transition, and only three are observed in the current spectrum. Since the energy of the  ${}^1B_1(S_2)$  state is only  $2000\text{ cm}^{-1}$  above that of the  $S_1$  state, Franck-Condon forbidden  $b_1$  modes are activated by Herzberg-Teller vibronic coupling. Interestingly, these Herzberg-Teller transitions are much stronger in intensity than those symmetry allowed  $a_1$  modes in Figure 6.2. In Rouillé *et al*'s cavity ring-down experiment,<sup>31</sup> six major peaks were observed, most of which agree with our assignment. One exception is the peak at  $757\text{ cm}^{-1}$ : our calculation

contains an  $a_1$  mode at  $754\text{ cm}^{-1}$ , but the previous work assigned it to an  $8b_1$  mode which is calculated to be at  $778\text{ cm}^{-1}$ . Moreover, the band located at  $780\text{ cm}^{-1}$  in the REMPI spectrum seems to fit well with the  $8b_1$  mode. The report from the experiment in helium droplets by Birer, Moreschini and Lehmann<sup>28</sup> (BML) contains more spectral features, and all the fundamental transitions agree with our REMPI experiment. However, for the spectral features in the range of  $779\text{ cm}^{-1}$  to  $1000\text{ cm}^{-1}$ , the assignment from Birer, Moreschini and Lehmann has a  $\sim 20\text{ cm}^{-1}$  difference between experiment and calculation. Our revised assignment, on the other hand, has reduced the difference to  $5\text{ cm}^{-1}$ , on par with our uncertainty of  $3\text{ cm}^{-1}$ .

#### 6.4.2 ZEKE spectroscopy

By scanning the ionization laser while setting the resonant laser at one of the intermediate states identified in the above REMPI experiment, we obtained pulsed field ionization ZEKE spectra as shown in Figure 6.3. The assignment of the vibrational levels of the cation is noted by a superscript “+”. The identity of the vibrational level of the intermediate state for each ZEKE spectrum is labeled in the corresponding panel by a black dot. The experimental and theoretical values are shown in Table 6.2. The calculation was performed at the B3LYP/6-311G (d,p) level. Using a least-squares fitting procedure similar to that for the  $S_1$  state, we obtained a scaling factor of 1.000 with a coefficient of determination 0.9993.

Limited by the linewidth of the resonant transitions and the pulsed electric field, the uncertainty of the experimental values of the ZEKE spectra is  $5 \text{ cm}^{-1}$ .

The ZEKE spectra are sparse, which is common among most ZEKE spectra of PAH molecules. The most salient feature of the ZEKE spectra is the dominance of the same vibrational level as that of the  $S_1$  intermediate state. This result is actually different from other PAHs we have studied<sup>21,22</sup>; rather, it is similar to our previous studies of heterocycles and phenyl derivatives.<sup>37-41</sup> In our previous work on ZEKE spectroscopy of substituted aromatic compounds<sup>37-41</sup>, we have used the distribution of vibrational bands in the ZEKE spectrum to gauge the stability of the molecular frame from  $S_1$  to  $D_0$ . When the substituent is electron-rich, the cation exhibits negligible geometric change upon ionization, and the ZEKE spectra are dominated by one vibrational band corresponding to the same vibrational excitation of the intermediate  $S_1$  state. When the substituent is electron-poor, the ZEKE spectra contain long progressions of modes related to skeletal rearrangements. Our studies of pentacene and pyrene have further showed that the stability of PAHs fall in between those of phenyl derivatives containing electron-rich substituents and those containing electron-poor substituents<sup>37-41</sup>. The sparse ZEKE spectra of BghiP and the dominance of each spectrum by a single vibrational band seem to conform to the trend of electron-rich substituents. Perhaps this is due to the capability of distributing the charge among all six conjugate rings in the cation.

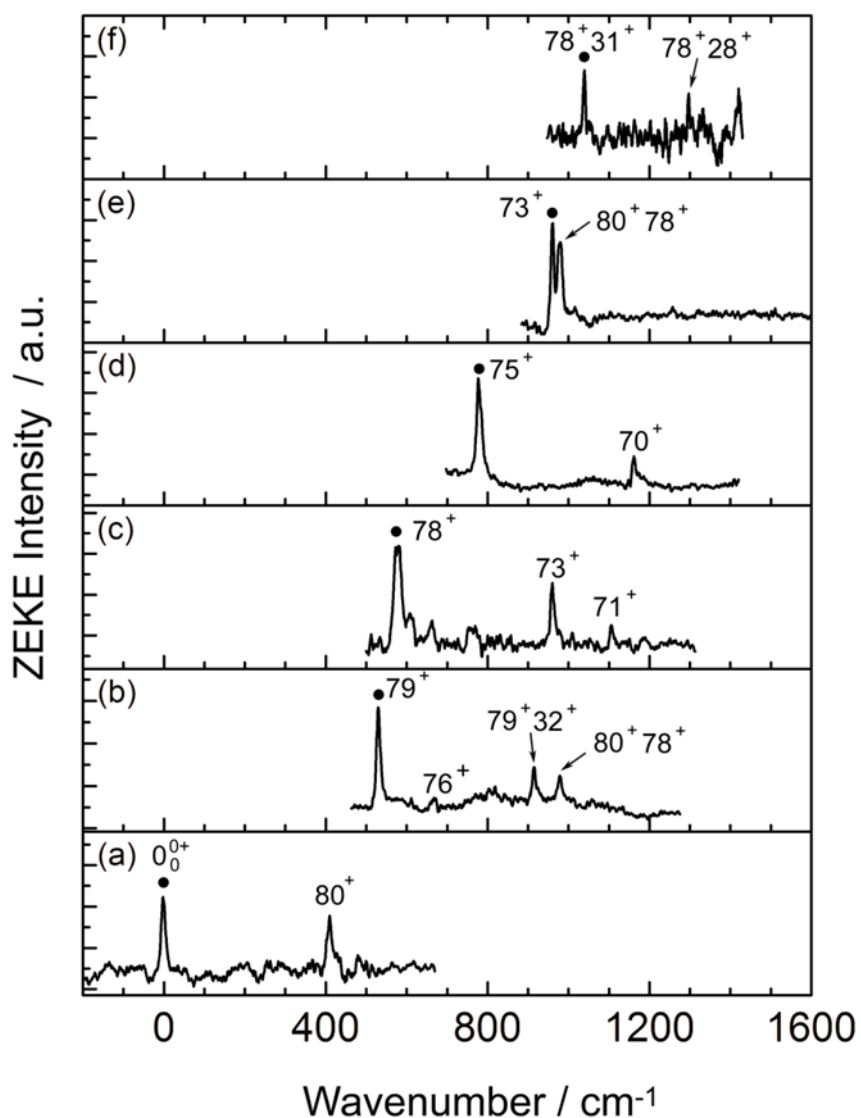


Figure 6.3. Two-color ZEKE spectra of BghiP recorded via seven vibrational levels of the  $S_1$  state as intermediate states: (a)  $0_0^0$ , (b)  $79^1$ , (c)  $78^1$ , (d)  $75^1$ , (e)  $73^1$ , (f)  $78^1 31^1$ . The energy in the  $x$ -axis is relative to the ionization threshold at  $57623 \text{ cm}^{-1}$ . The assignment in the figure refers to the vibrational levels of the cation, and the corresponding vibrational level of the intermediate state is labeled by a black dot in each panel.

Table 6.2. Observed and calculated vibrational frequencies of benzo[*g,h,i*]perylene cation

0	3b <sub>1</sub>	4b <sub>1</sub>	7b <sub>1</sub>	9b <sub>1</sub>	4b <sub>1</sub> +3a <sub>1</sub>	cal	Assignment
0						0	0
410						413	80 <sup>+</sup> (2b <sub>1</sub> <sup>+</sup> )
	531					533	79 <sup>+</sup> (3b <sub>1</sub> <sup>+</sup> )
		574				570	78 <sup>+</sup> (4b <sub>1</sub> <sup>+</sup> )
	673					687	76 <sup>+</sup> (6b <sub>1</sub> <sup>+</sup> )
			781			786	75 <sup>+</sup> (7b <sub>1</sub> <sup>+</sup> )
	919					924	79 <sup>+</sup> 32 <sup>+</sup> (3b <sub>1</sub> <sup>+</sup> +2a <sub>1</sub> <sup>+</sup> )
		961		960		957	73 <sup>+</sup> (9b <sub>1</sub> <sup>+</sup> )
	980			981		983	80 <sup>+</sup> 78 <sup>+</sup> (4b <sub>1</sub> <sup>+</sup> +2b <sub>1</sub> <sup>+</sup> )
					1039	1028	78 <sup>+</sup> 31 <sup>+</sup> (4b <sub>1</sub> <sup>+</sup> +3a <sub>1</sub> <sup>+</sup> )
		1108				1115	71 <sup>+</sup> (11b <sub>1</sub> <sup>+</sup> )
			1165			1169	70 <sup>+</sup> (12b <sub>1</sub> <sup>+</sup> )
					1298	1290	78 <sup>+</sup> 28 <sup>+</sup> (4b <sub>1</sub> <sup>+</sup> +6a <sub>1</sub> <sup>+</sup> )

Trace (a) was recorded via the origin of the  $S_1$  state, and the most intense peak corresponds to the origin of the cation. The adiabatic ionization potential is thus determined to be  $57623 \pm 5 \text{ cm}^{-1}$  ( $7.1443 \pm 0.0006 \text{ eV}$ ). This value is about  $300 \text{ cm}^{-1}$  lower than that of  $7.19 \pm 0.01 \text{ eV}$  from photoelectron spectroscopy (PES) by Boschi, Murrell and Schmidt in 1972<sup>42</sup> and close to the result of  $7.15 \text{ eV}$  from gas phase ion equilibrium measurements by Meot-Ner in 1979<sup>43</sup>.

Although the same selection rule applies to both the REMPI and the ZEKE process, the vibrational distribution of the ZEKE spectrum from the origin of the  $S_1$  state is qualitatively different from that of the REMPI spectrum. The extensive Franck-Condon activity above  $400 \text{ cm}^{-1}$  in the REMPI spectrum is missing in trace (a), while a new mode 80 seems to become active in the ZEKE spectrum. In addition, several vibrational modes observed in REMPI are missing in the ZEKE spectra, and most notably, no ZEKE signal was obtained via the  $a_1$  modes of the  $S_1$  state (modes 25 – 27) because of low signal-to-noise ratios. The ZEKE spectra also contain mostly  $b_1$  modes, while only a few  $a_1$  modes are observable via combination bands with  $b_1$ .

## 6.5 Discussion

The discussion on the symmetry and nature of the first two electronically excited states has had a long history. Based on experiments both in the gas phase and in the solution phase and on advanced theoretical calculations,<sup>27,30,32,44-46</sup> the general consensus is that the  $S_1$  state is  $^1A_1$ , and the  $S_2$  state is  $^1B_1$ . The electronic

transition is a mixture of LUMO  $\leftarrow$  HOMO - 1 and LUMO + 1  $\leftarrow$  HOMO to the S<sub>1</sub> state and mainly LUMO  $\leftarrow$  HOMO to the S<sub>2</sub> state, and extensive vibronic coupling is expected. CIS calculations typically cannot predict the correct energy order in this case of extreme configuration interaction, thus we set the keyword root = 2 for structure optimization and vibrational frequency calculation of the S<sub>1</sub> state. With the scaling factor, the fit in vibrational frequency between experiment and calculation is quite satisfactory.

### 6.5.1 Geometry and vibrational modes of the S<sub>1</sub> state

Based on our results of structural optimization, electronic excitation and further ionization induce negligible changes in the overall size of the molecular frame, including both the horizontal and vertical dimensions. This observation suggests that the aromatic system has a tremendous ability to accommodate changes in the electron density. This result is expected for PAHs containing several fused conjugated aromatic rings. Consequently, we would predict sparse spectral features with only a<sub>1</sub> in-plane stretching modes in the REMPI spectrum. In addition, vibronic coupling with the <sup>1</sup>B<sub>1</sub> state would result in activation of some in plane bending b<sub>1</sub> modes. To observe the out of plane a<sub>2</sub> and b<sub>2</sub> modes, only levels with even quantum numbers are possible.

The assignment in Table 6.1 agrees with the above analysis, but the intensity distribution is opposite to our prediction, with the Franck-Condon allowed

$a_1$  modes much weaker than the vibronic  $b_1$  bands. This situation should be compared with that of pyrene<sup>35</sup>, another peri-condensed PAH, and those of a few cata-condensed PAHs<sup>21,22,47,48</sup>. In the REMPI spectrum of pyrene, in plane stretching modes were relative stronger than out of plane vibronic modes. In both cata- and peri-condensed PAHs previously reported using REMPI, a strong longitudinal stretching mode has been observed, and its frequency demonstrates a reciprocal relationship relative to the length of the molecule. This mode for BghiP calculated at  $377\text{ cm}^{-1}$  should be within the observation window of Figure 6.1, but it is missing or too weak to be recognizable. This situation is probably caused by the extremely strong vibronic coupling with the  $S_2$  state, which could greatly intensify the  $b_1$  modes. It is worth noting that in all of our previous studies of PAHs, there have always been several out of plane modes due to vibronic coupling in the REMPI spectra. In the case of BghiP, however, the symmetry of the  $S_2$  state dictates that only in plane vibronic modes should be observable. Thus the missing out of plane modes in Figure 6.2 is not surprising and does not indicate lack of vibronic coupling.

### 6.5.2 Geometry and vibrational modes of the $D_0$ state

We have calculated the Mulliken charge distribution for the  $D_0$  state by including the charges on the peripheral hydrogen atoms in the adjacent ring, and dividing the charges on the shared carbon among the conjoint rings. Ring III has

about 30% of positive charge ring II and ring I shares 18% and 15% each, and the inner ring IV is slightly negative charged. This result is consistent with basic organic chemistry. Since there is no hydrogen attached to ring IV, this region is inaccessible for any reaction. Substitution and addition reactions are most favored on ring III, which has the most positive charge in the cationic state.

All observed modes including  $b_1$  and  $a_1$  modes in ZEKE are IR active, however, a direct frequency comparison with results from literature reports is still impossible. Hudgins and Allamandola reported the cation IR spectroscopy of *BghiP* in argon matrix from  $600\text{ cm}^{-1}$  to  $1600\text{ cm}^{-1}$ .<sup>49</sup> Bernstein et al studied the cation IR spectroscopy in solid water from  $1120\text{ cm}^{-1}$  to  $1600\text{ cm}^{-1}$ . Within the range of frequency overlap with our current work, unfortunately, these two studies failed to observe any  $b_1$  or  $a_1$  modes due to their low transition intensities. This situation alludes to the value of ZEKE spectroscopy for astrophysical studies: although the vibrational intensities from ZEKE are not representative of single photon absorption, the frequency information is still valuable to astrophysical investigations. Furthermore, for non-central symmetric PAHs such as *BghiP*, vibrational frequencies from ZEKE can even be used for direct line identification.

Based on our previous studies of cata-condensed PAHs and a series of small benzene derivatives,<sup>21,22,35,37-41</sup> DFT calculations typically yield reliable vibrational frequency information for the cation. In the case of *BghiP*, the maximum deviation between theory and experiment is  $\sim 14\text{ cm}^{-1}$  without any scaling factor. This

agreement is inferior to our previous reports on tetracene and pentacene.<sup>21,22</sup> but better than the case of pyrene<sup>35</sup> and better than that of  $\sim 25\text{ cm}^{-1}$  from matrix isolation spectroscopy.<sup>34,49</sup> The somewhat larger than expected deviation might be related to the strong vibronic coupling due to configuration interaction. Based on our limited sampling of peri-condensed PAHs where configuration interaction seems to be prevalent, frequency calculations using DFT even with the largest possible basis set are questionable. To fully utilize the potential of FIR spectroscopy for astrophysical identification of single PAHs, further exploration of other calculation methods and calibration of theoretical values with experimental results are still much needed.

## 6.6 Conclusion

Vibrational properties of the electronically excited and ionic states of benzo[*g,h,i*]perylene have been studied using REMPI and ZEKE. Due to Herzberg-Teller coupling, the vibronic allowed bands of the first excited state are much stronger in intensity than those of Franck-Condon allowed  $a_1$  modes. Unlike previous studies of other PAHs such as pyrene or pentacene, B*ghi*P shows no out-of-plane modes in both REMPI and ZEKE. This result can be understood from the symmetry of the  $S_2$  state, which does not include out of plane modes in vibronic coupling. Based on our calculation, the overall size of the B*ghi*P molecular frame of the  $S_0$ ,  $S_1$  and  $D_0$  states remain largely unchanged upon electronic excitation and ionization. The dominance of each ZEKE spectrum by a single vibrational band

further confirms our calculation result. All observed modes in ZEKE are IR active, and the frequencies can be used directly for line identification in astrophysical investigations.

## **6.7 Acknowledgements**

This work is supported by the National Aeronautics and Space Administration under award No. NNX09AC03G. Acknowledgment is made to the Donors of The Petroleum Research Fund, administered by the American Chemical Society, for partial support of this research.

## 6.8 Reference

- (1) Tielens, A. G. G. M., *Annu. Rev. Astron. Astrophys.*, **2008**, *46*, 289-337.
- (2) Harvey, R. G. *Polycyclic aromatic hydrocarbons: chemistry and carcinogenicity*: Cambridge University Press: London, 1991.
- (3) Smith, L. E.; Denissenko, M. F.; Bennett, W. P.; Li, H.; Amin, S.; Tang, M.-s.; Pfeifer, G. P. *J. Natl. Cancer Inst.* **2000**, *92*, 803-811.
- (4) Li, A. PAHs in Comets: An Overview. In *Deep Impact as a World Observatory Event: Synergies in Space, Time, and Wavelength*; Kaufl, H. U., Siebenmorgen, R., Moorwood, A. F. M., Eds.; Springer: Berlin, 2009; pp 161-175.
- (5) Allamandola, L. J.; Tielens, A. G. G. M.; Barker, J. R. *Astrophys. J.*, **1985**, *290*, L25-L28.
- (6) L'éger, A.; Puget, J., *Astron. Astrophys.*, **1984**, *137*, L5-L8.
- (7) Mallocci, G.; Mulas, G.; Benvenuti, P. *Astron. Astrophys.*, **2003**, *410*, 623-637.
- (8) Mulas, G.; Mallocci, G.; Benvenuti, P. *Astron. Astrophys.*, **2003**, *410*, 639-648.
- (9) Peeters, E.; Allamandola, L. J.; Hudgins, D. M.; Hony, S.; Tielens, A. G. G. M. *Astron. Soc. Pac. Conf. Ser.*, **2004**, *309*, 141-162.
- (10) Langhoff, S. R., *J. Phys. Chem.* **1996**, *100*, 2819-2841.
- (11) Parisel, O.; Berthier, G.; Ellinger, Y., *Astron. Astrophys.*, **1992**, *266*, L1-L4-L1-L4.
- (12) Bernstein, M. P.; Dworkin, J. P.; Sandford, S. A.; Cooper, G. W.; Allamandola, L. J., *Nature* **2002**, *416*, 401-403.
- (13) Mulas, G.; Mallocci, G.; Joblin, C.; Toubanc, D., *Astronomy Astron. Astrophys.*, **2006**, *456*, 161-169.
- (14) Shock, E. L.; Schulte, M. D., *Nature* **1990**, *343*, 728-731.
- (15) Wakeham, S. G.; Schaffner, C.; Giger, W., *Geochim. Cosmochim. Acta*, **1980**, *44*, 415-429.
- (16) Qi, F.; Yang, R.; Yang, B.; Huang, C.; Wei, L.; Wang, J.; Sheng, L.; Zhang, Y. *Rev. Sci. Instrum.*, **2006**, *77*, 084101.
- (17) Biennier, L.; Salama, F.; Gupta, M.; O'keefe, A., *Chem. Phys. Lett.*, **2004**, *387*, 287-294.
- (18) Hudgins, D. M., *Polycyclic Aromat. Compd.*, **2002**, *22*, 469-488.
- (19) Joblin, C.; Berné O.; Simon, A.; Mulas, G. *arXiv:0904.3185* **2009**.
- (20) Zhang, K.; Guo, B.; Colarusso, P.; Bernath, P. F., *Science* **1996**, *274*, 582-583.
- (21) Zhang, J.; Han, F.; Li, A.; Kong, W. *Astrophys. J.*, **2010**, *715*, 485-492.
- (22) Zhang, J.; Pei, L.; Kong, W., *J. Chem. Phys.*, **2008**, *128*, 104301-104307.
- (23) Merkt, F.; Schmutz, H., *J. Chem. Phys.*, **1998**, *108*, 10033-10045.
- (24) Li, A.; Draine, B. T., *Astrophys. J.*, **2001**, *554*, 778-802.

- (25) Li, A.; Draine, B. T., *Astrophys. J.*, **2002**, *576*, 762-772.
- (26) Li, A.; Luning, J. I., *Astrophys. J.*, **2003**, *594*, 987-1010.
- (27) Aihara, J.-i.; Ohno, K.; Inokuchi, H. *Bull. Chem. Soc. Jpn.*, **1970**, *43*, 2435-2439.
- (28) Birer, Ö.; Moreschini, P.; Lehmann, K. K., *Phys. Chem. Chem. Phys.*, **2008**, *10*, 1648-1657.
- (29) Birks, J. B.; Easterly, C. E.; Christophorou, L. G., *J. Chem. Phys.*, **1977**, *66*, 4231.
- (30) Chillier, X.; Boulet, P.; Chermette, H.; Salama, F.; Weber, J., *J. Chem. Phys.*, **2001**, *115*, 1769-1776.
- (31) Rouillé, G.; Arold, M.; Staicu, A.; Krasnokutski, S.; Huisken, F.; Henning, T.; Tan, X.; Salama, F., *J. Chem. Phys.*, **2007**, *126*, 174311.
- (32) Tan, X.; Salama, F., *J. Chem. Phys.*, **2005**, *123*, 014312
- (33) Hudgins, D. M.; Sandford, S., *J. Phys. Chem. A*, **1998**, *102*, 344-352.
- (34) Bernstein, M. P.; Sandford, S. A.; Mattioda, A. L.; Allamandola, L. J., *Astrophys. J.*, **2007**, *664*, 1264-1272.
- (35) Zhang, J.; Han, F.; Kong, W. *J. Phys. Chem. A*, **2010**, submitted.
- (36) *Gaussian 03*, Revision E.01, Frisch, M. J., *et. al.* Gaussian, Inc., Wallingford CT, 2004.
- (37) He, Y.; Kong, W., *J. Chem. Phys.*, **2006**, *124*, 2043061-20430618.
- (38) He, Y.; Wu, C.; Kong, W., *J. Chem. Phys.*, **2004**, *121*, 8321-8328.
- (39) He, Y.; Wu, C.; Kong, W., *Chem. Phys. Lett.*, **2004**, *391*, 38-43.
- (40) He, Y.; Wu, C.; Kong, W., *J. Chem. Phys.*, **2004**, *121*, 3533-3539.
- (41) Wu, C.; He, Y.; Kong, W., *Chem. Phys. Lett.*, **2004**, *398*, 351-356.
- (42) Boschi, R.; Murrell, J. N.; Schmidt, W., *Faraday Discuss. Chem. Soc.*, **1972**, *54*, 116-126
- (43) Meot-Ner, M., *J. Chem. Phys.*, **1980**, *84*, 2716-2723
- (44) Hummel, R. L.; Redenberg, K., *J. Chem. Phys.*, **1962**, *66*, 2334-359.
- (45) Nijegorodov, N.; Mabbs, R.; Downey, W. S., *Spectrochim. Acta, Part A*, **2001**, *57*, 2673-2685
- (46) Palewska, K.; Chojnacki, H., *J. Mol. Struct.*, **2002**, *611*, 23-32
- (47) Syage, J. A.; Wessel, J. E., *J. Chem. Phys.*, **1988**, *89*, 5962-5962.
- (48) Piuze, F.; Dimicoli, I.; Mons, M.; Milli é P.; Brenner, V.; Zhao, Q.; Soep, B.; Tramer, A., *Chem. Phys.*, **2002**, *275*, 123-123.
- (49) Hudgins, D. M.; Allamandola, L. J. *J. Phys. Chem.*, **1995**, *99*, 3033-3046.

**Zero kinetic energy photoelectron spectroscopy of benzo[*a*]pyrene**

Jie Zhang, Fangyuan Han, and Wei Kong\*

*Department of Chemistry, Oregon State University, Corvallis, Oregon 97331-4003*

In preparation

---

\* To whom correspondence should be addressed.

E-mail: [Wei.Kong@oregonstate.edu](mailto:Wei.Kong@oregonstate.edu), Phone: 541-737-6714. Fax: 541-737-2062

## 7.1 Abstract

We report zero kinetic energy photoelectron (ZEKE) spectroscopy of benzo[*a*]pyrene (BaP) via resonantly enhanced multiphoton ionization (REMPI). Our analysis concentrates on the vibrational modes of the first excited state ( $S_1$ ) and those of the ground cationic state ( $D_0$ ). Similar to other peri-condensed PAHs we have investigated, the first two electronically excited states of BaP exhibit extensive configuration interactions. However, the two electronic states are of the same symmetry, hence vibronic coupling does not introduce any out of plane modes in the REMPI spectrum, and Franck-Condon analysis is qualitatively satisfactory. The ZEKE spectra from the in plane modes observed in the REMPI spectrum demonstrate strong propensity in preserving the vibrational excitation of the intermediate state. Although several additional bands in combination with the vibrational level of the intermediate state are identifiable, they are much lower in intensity. The implication of this observation is that the molecular structure of BaP has a tremendous capability to accommodate changes in charge density. All observed bands of the cation are IR active, establishing the role of ZEKE spectroscopy in mapping out far infrared bands for astrophysical applications.

## 7.2 Introduction

Polycyclic aromatic hydrocarbons (PAHs) are a group of hydrocarbon molecules with fused six member aromatic ring frames terminated with peripheral H atoms. They are an important group of molecules for laboratory astrophysical studies because of their possible role in infrared emission in the interstellar medium (ISM) and their potential as an energy and carbon storage reservoir. In the mid 1970s, a series of unidentified infrared (UIR) bands, including features at 3.3, 6.2, 7.7, 8.6, and 12.7  $\mu\text{m}$ , have been discovered in a spectroscopic study of planetary nebulae.<sup>1</sup> Later on, these UIR bands have been shown to be ubiquitous for a variety of astronomical sources. It is well accepted now that these 3.3 – 17.4  $\mu\text{m}$  features can be characterized as C-H, C-C or C-C-C stretching modes.<sup>2-7</sup> Polycyclic aromatic hydrocarbons have since been considered an important subject of astrophysical investigations. Given the abundant radiation sources in the ISM, ionic PAHs have also been considered promising carriers of the UIR bands.<sup>8-10</sup>

For comparisons with astrophysics observations, efforts have been made on the study of laboratory infrared spectrum of PAHs and their cations, including matrix isolation spectroscopy,<sup>11,12</sup> Infrared emission,<sup>13</sup> laser induced fluorescence, photoionization spectroscopy<sup>14</sup>, cavity ringdown<sup>15</sup>. Unfortunately, identification of specific PAHs has been unsuccessful so far. This is largely due to the fact that mid-IR bands only represent the local motion or the functional groups of the molecule. In contrast, far-infrared (FIR) bands are sensitive to the molecular size and

structure, hence FIR spectroscopy is thus considered fingerprints for individual molecules or ions. The *Herschel Space Observatory* launched in May, 2009 is aimed for the FIR and submillimeter (submm) wavelength region of the ISM. One of the goals of *Herschel* is to map out the chemical composition of the ISM and the atmospheres and surfaces of comets, planets and satellites.

Laboratory FIR spectroscopy has always been challenging due to the lack of light sources and detectors. Moreover, spectroscopy of ions is further hindered by the low achievable particle density. The technique of zero kinetic energy photoelectron (ZEKE) spectroscopy serves as an ideal tool, albeit indirect, for the study of low frequency vibrational modes of cations.<sup>16-18</sup> ZEKE is known for its high resolution of cation rovibrational spectroscopy. The high Rydberg states in ZEKE are longer lived when they are associated with lower vibronic states of the cation, which makes it particularly suitable for studies of lower frequency vibrational modes. Thus by detecting electrons from pulsed field ionization in ZEKE spectroscopy via resonantly enhanced multiphoton ionization (REMPI), we can avoid both the light source and the detector problems in typical FIR and submillimeter wave experiments. The vibrational information from ZEKE is largely governed by the Franck-Condon principle, hence the information from ZEKE might not be directly applicable for line identification in astronomy, but the information of IR inactive modes can be used for frequency calibrations of FIR spectroscopy from theoretical calculations and for theoretical modeling of the energy and chemical balance in the ISM.<sup>19,20</sup>

Benzo[*a*]pyrene (BaP) is a five ring PAH as shown in Figure 7.1. It is the most abundant in the earth's atmosphere and it is highly carcinogenic.<sup>21-23</sup> Although it has been more than fifty years since the first study of BaP, spectroscopic information is still limited. Greenblatt *et al* have performed the first fluorescence excitation spectrum in a supersonic jet, assigned the 0-0 transition of the S<sub>1</sub> state at  $25265 \pm 20 \text{ cm}^{-1}$ , and measured the lifetime of the first excited state to be 270 ns.<sup>24</sup> They have also discussed the S<sub>2</sub> state which is about  $1500 \text{ cm}^{-1}$  higher than S<sub>1</sub>, and have attributed the long lifetime of the S<sub>1</sub> state to strong vibronic coupling. In Gittins *et al*'s work, the first excited state has been studied in a supersonic jet using fluorescence excitation and two color REMPI, and 32 modes have been assigned based on their CIS calculation. However, as will be discussed later, the authors did not distinguish the two closely coupled electronic states explicitly, and there might be a problem with the calculation.<sup>25</sup> In addition, we will also refer to a study of the infrared spectroscopy of BaP and its radical ion doped in wax film from  $2000$  to  $400 \text{ cm}^{-1}$  in our discussions of ZEKE spectroscopy.<sup>26</sup>

### 7.3 Experimental setup

The experimental apparatus is a differentially pumped high vacuum molecular beam machine, with the detection chamber enclosed inside the source chamber<sup>16,18</sup>. A time-of-flight mass spectrometer in the detection chamber also serves as the pulsed field ionization zero kinetic energy photoelectron spectrometer.

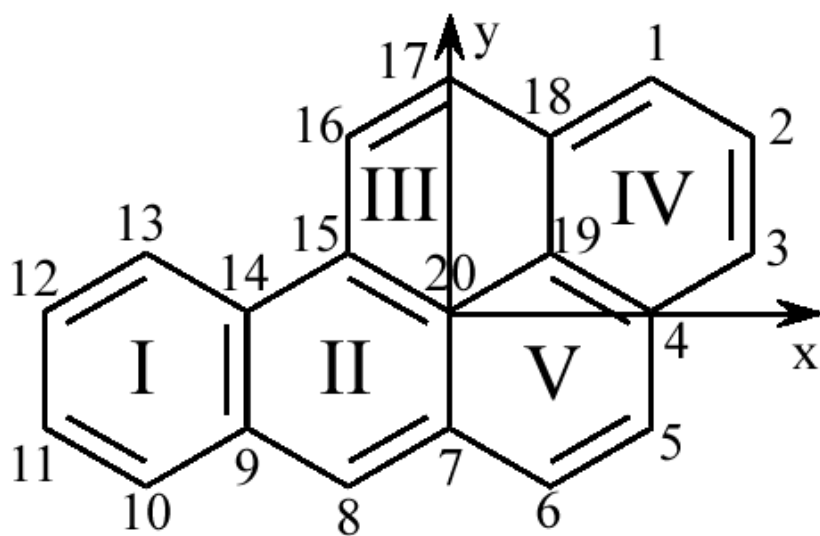


Figure 7.1. Structure of Benzo[a]pyrene and the orientation of the axes.

The sample benzo[*a*]pyrene (Aldrich) was housed and heated to 170 °C in the pulsed valve located in the source chamber to achieve sufficient vapor pressure. The vapor was seeded in 1600 torr of argon and co-expanded into vacuum through a pulsed valve with a 1 mm orifice. After passing through a 2 mm skimmer, the cooled sample reached the detection chamber for laser excitation and ionization. The laser systems for the REMPI experiment included two Nd:YAG (Spectra Physics, GCR 190 and Spectra Physics, GCR 230) pumped dye lasers (Laser Analytical System, LDL 20505 and Laser Analytical Systems, LDL 2051). The pump laser in the 398 - 382 nm range, obtained from the dye laser system (Exalite 389), had a pulsed energy of 1.5 mJ/pulse with a bandwidth of 0.5 cm<sup>-1</sup>. The ionization laser in the 312.3 - 304.6 nm range from the frequency-doubled output of the other dye laser (Rhodamine 610 and sulforhodamine 640) had a pulse energy of 1 mJ/pulse with a band width of 0.3 cm<sup>-1</sup>. The absolute wavelength of each laser was calibrated using an iron hollow-cathode lamp filled with neon. The pump laser and ionization laser were set to counter-propagate, and the light path, the flight tube, and the molecular beam were mutually perpendicular. The relative timing among the three laser pulses was controlled by two delay generators (Stanford Research, DG 535), and the optimal signal was obtained under temporal overlap between the pump and ionization lasers. In the ZEKE experiment, molecules excited to high Rydberg states were allowed to stay for 1 - 2 μs in the presence of a constant DC spoiling field of ~ 0.5 V/cm, after which ionization and extraction was achieved by a pulsed electric field of ~5 V/cm.

Gaussian 03 suite<sup>27</sup> was used to optimize the molecular structure and to obtain vibrational frequencies for assignment of the observed vibronic structures from REMPI and ZEKE. For the ground state of the neutral and the cationic state, density functional theory (DFT) calculations using the B3LYP functional were performed with the 6-31+G (d,p) basis set. The excited state  $S_1$  was calculated at the configuration interaction singles (CIS) level using the 6-31+G (d,p) basis set. The CIS method was chosen because of the size of the molecule and our computational resources. In addition, we have also used the same method for other PAHs and a few benzene derivatives with satisfactory results.<sup>17,18,28-32</sup> The resulting vibrational frequencies were scaled by a factor of 0.9203, the choice of which will be discussed in the following section. For the  $D_0$  state, a scaling factor of 0.9803 was adopted.

## 7.4 Results

### 7.4.1 Two-color 1+1' REMPI spectroscopy

The two-color 1+1' REMPI spectrum of BaP near the origin of the  $S_1 \leftarrow S_0$  electronic transition is displayed in Figure 7.2a. The ionization laser was set at 290 nm and was temporally overlapped with the scanning resonant laser. The most intense peak at  $25,205 \pm 3\text{cm}^{-1}$  is assigned as the origin band, which is  $28\text{ cm}^{-1}$  to the red compared with the report by Gittins *et al*<sup>25</sup>. The experimental uncertainty of  $3\text{ cm}^{-1}$  is mostly due to the linewidth of the vibronic bands, since the linewidth of the excitation laser beam is only  $0.3\text{ cm}^{-1}$ . Other observed vibronic transitions are

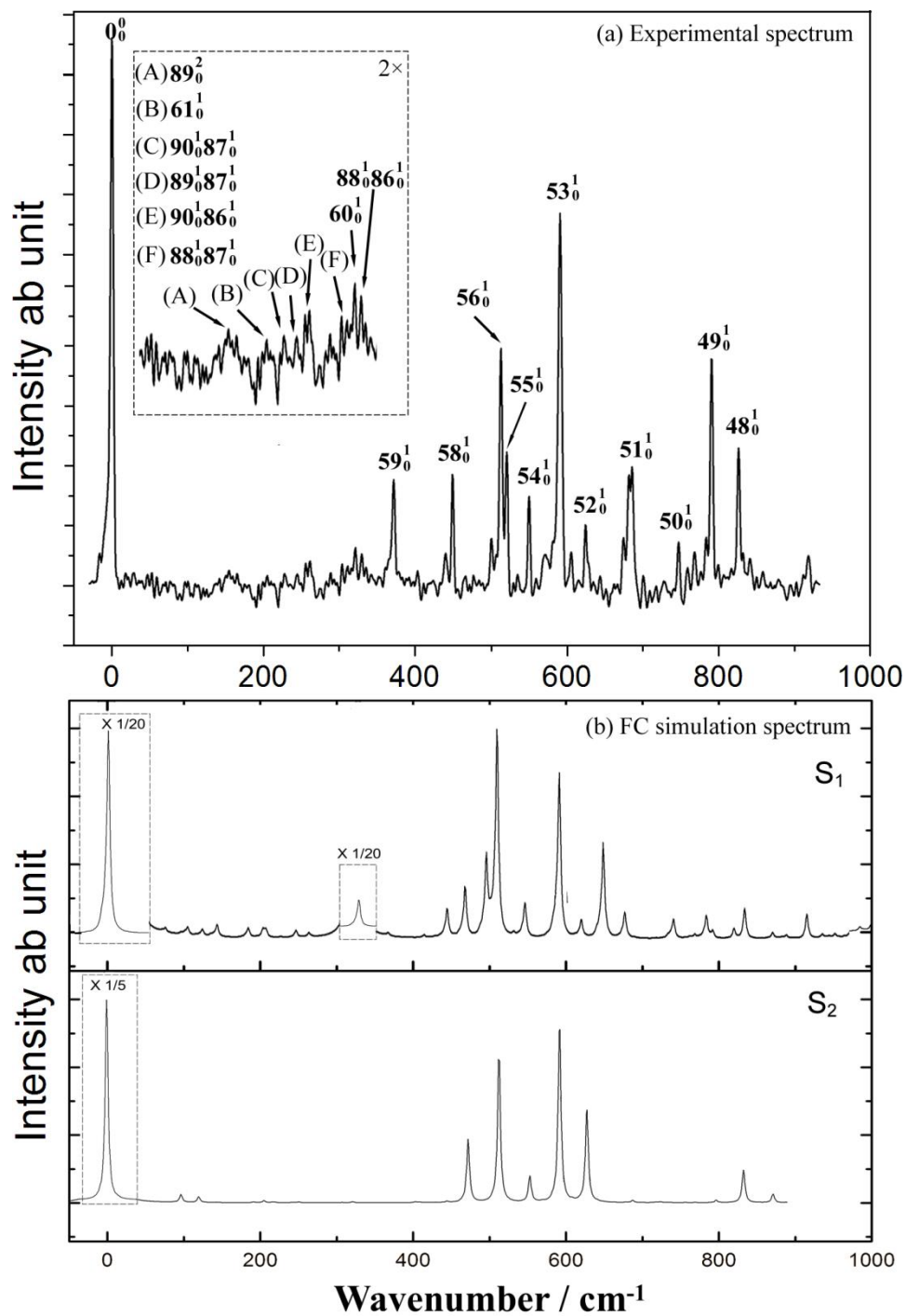


Figure 7.2 REMPI spectrum and Franck-Condon simulation of benzo[*a*]pyrene. (a) Experimental result. (b) Franck-Condon simulation.

Table 7.1 Observed and calculated vibrational frequencies of the  $S_1$  state of benzo[*a*]pyrene

Experiment	Cal	Intensity	Assignment
154	149	vw	89 <sup>2</sup>
206	209	vw	61 <sup>1</sup>
230	229	vw	90 <sup>1</sup> 87 <sup>1</sup>
246	249	vw	89 <sup>1</sup> 87 <sup>1</sup>
253	249	vw	90 <sup>1</sup> 86 <sup>1</sup>
304	309	vw	88 <sup>1</sup> 87 <sup>1</sup>
322	328	vw	60 <sup>1</sup>
331	330	vw	88 <sup>1</sup> 86 <sup>1</sup>
373	372	m	59 <sup>1</sup>
451	450	m	58 <sup>1</sup>
515	502	s	56 <sup>1</sup>
523	516	s	55 <sup>1</sup>
551	553	m	54 <sup>1</sup>
593	599	vs	53 <sup>1</sup>
626	628	s	52 <sup>1</sup>
688	686	s	51 <sup>1</sup>
749	750	w	50 <sup>1</sup>
793	794	s	49 <sup>1</sup>
829	835	m	48 <sup>1</sup>

listed in Table 7.1. The labeling of each vibrational mode is based on spectroscopic conventions, i. e. by using consecutive numbers in reference to the symmetry species and the frequency in decreasing order. Frequencies from CIS calculations are well known for being too high, so we used a scaling factor and adjusted its value to match the experimental results using a least-squares linear regression method. The resulting scaling factor of 0.9203 had a value of 0.9992 for the coefficient of determination ( $R^2$ ).

BaP is a planar molecule with  $C_s$  symmetry. There are altogether 90 vibrational normal modes, with 61  $a'$  modes that are numbered 1 – 61, and 29  $a''$  modes numbered 62 – 90. Within the range of our REMPI spectrum, 13 of the  $a'$  modes should be observable, from mode 61 to mode 48, and these modes constitute the central cluster of vibronic transitions in the spectrum. The intensities of the two lowest  $a'$  modes 60 and 61 are much weaker than those of other  $a'$  modes, and mode 57 at  $473\text{ cm}^{-1}$  seems to be completely missing. With the exception of modes 56 and 55, the agreement between theory and experiment is within  $6\text{ cm}^{-1}$ , larger than the experimental uncertainty of  $3\text{ cm}^{-1}$ . The theoretical frequencies for both mode 55 and 56 are significantly lower than the experimental values. As will be observed in the ZEKE experiment, the same trend of disagreement persists for the same modes in the cation.

The observed Franck-Condon allowed totally symmetric  $a'$  modes can be grouped into three categories. The first type is the modes located mainly on the

pyrene ring structure<sup>16</sup>, including modes 58, 56, 54, 50 and 49. In particular modes 58 and 50 have very similar displacement vectors as those of the second and third  $b_{3g}$  modes of pyrene. Due to the additional ring attached to the pyrene moiety, both modes shift to lower frequencies by about 10%. The second type of observed modes including modes 59 and 52 is related to the motion of the extra phenyl ring. Mode 59 involves swinging and mode 52 involves stretching of the extra phenyl ring. The third type of modes are skeletal modes of the whole molecular frame, including modes 61, 60, 55, 53, 51, and 48. Mode 60 is the in-plane bending mode, mode 55 is the longitudinal stretching modes, and mode 53 is the transverse stretching mode. These two modes are widely reported among many PAHs, and the frequencies of which are observed to be inversely proportional to the dimension of the molecule. Consistent with this trend, the frequencies of both stretching modes in BaP are lower than those in pyrene. The rest of the skeletal modes involve mixed motions of stretching and ring deformation.

We performed a Franck-Condon calculation<sup>33</sup> for the  $S_1 \leftarrow S_0$  transition using the program from Dr. Dongsheng Yang, and the resulting spectrum is shown in the upper half of panel b. The simulation captured the strong origin band and the cluster of low frequency a' bands between 400 and 800  $\text{cm}^{-1}$ , but some deviations are clearly noticeable. The origin band from calculation is about 20 times stronger than from experiment, in reference to the cluster of vibronic bands. Even more

dramatic is the intensity for mode 60: the Franck-Condon calculation seems to be orders of magnitude off in comparison with the experiment.

Below  $350\text{ cm}^{-1}$  in the experimental REMPI spectrum (panel a), there are several weak bands that can be tentatively assigned as overtones or combination bands of out-of-plane  $a''$  modes. These bands are barely above the noise level in the spectrum, hence their assignment is tentative. Interestingly, the existence of these bands is reproduced by the Franck-Condon calculation in the lower half of panel b. If we define the length of the molecule along the x axis as  $L$ , the waving cycle of mode 90 is  $L/2$  and that of mode 88 is  $L/4$ , with a wave propagation vector along the x axis. Mode 86 is a “doming” motion mostly located on the pyrene part of the structure. Modes 89 and 87 are the out-of-plane twisting modes.

In the cluster of vibronic transitions between  $400$  and  $800\text{ cm}^{-1}$ , the Franck-Condon calculation captures the majority of the modes, but the results are not quantitative. The intensity of modes 49 and 48 from calculation are too low, and the seemingly shifts in positions for modes 51 and 53 are actually due to different vibronic transitions (combination bands).

We have also performed the same calculation for the  $S_2$  state displayed in the lower half of Figure 7.2b. Scaling factors of each peak are labeled in the figure. Although both spectra have a strong origin band and a cluster of vibrational bands around  $500\text{ cm}^{-1}$ , the calculation from  $S_1$  seems to be a better fit. The disagreement

in detailed intensity distributions could be a result of intensity borrowing from similar vibrational levels between the two coupled electronic states.

#### 7.4.2 ZEKE spectroscopy

By scanning the ionization laser while setting the resonant laser at one of the intermediate states identified in the above REMPI experiment, we obtained pulsed field ionization ZEKE spectra as shown in Figures 7.3 and 7.4. The assignment of the vibrational levels of the cation is noted by a superscript “+”. The identity of the vibrational level of the intermediate state for each ZEKE spectrum is labeled in the corresponding panel by a black dot. The experimental and theoretical values are shown in Table 7.4. Limited by the linewidth of the resonant transitions and the pulsed electric field, the uncertainty of the experimental values from ZEKE is  $5\text{ cm}^{-1}$ . The calculation was performed at the B3LYP/6-31+G (d,p) level. In our past studies, DFT calculation normally yields great agreement with the experiment results for the cation frequencies.<sup>17,18</sup> In tetracene and pentacene cases, no scaling factor is used and in pyrene case, a factor of 0.995 is adopted to decrease the deviation from experiment result.<sup>16</sup> For BaP cation calculation, without the scaling factor, the difference between experiment result and theoretical one can be as large as  $23\text{ cm}^{-1}$ . Using a least-squares fitting procedure similar to that for the  $S_1$  state, a factor of 0.9803 for the theoretical vibrational frequencies of the cation was obtained with the coefficient of determination of 0.9991. The agreement between theory and experiment (scaled frequencies) is within a few wavenumbers for most

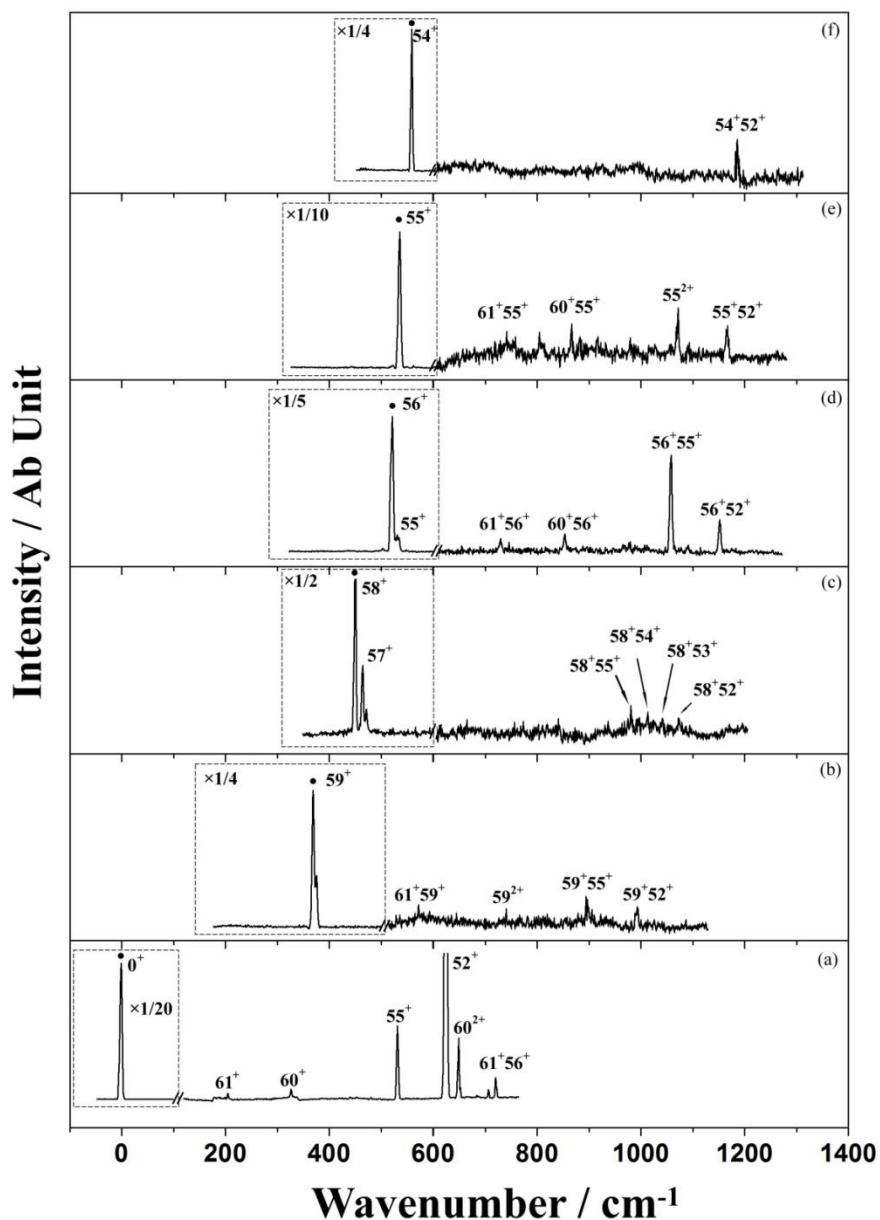


Figure 7.3 Two-color ZEKE spectra of BaP recorded via the following vibrational levels of the  $S_1$  state as intermediate states: (a)  $0^0$ , (b)  $59^1$ , (c)  $58^1$ , (d)  $56^1$ , (e)  $55^1$ , (f)  $54^1$ . The energy in the figure is relative to the ionization threshold at  $57271 \text{ cm}^{-1}$ . The assignment in the figure refers to the vibrational levels of the cation, and the corresponding vibrational level of the intermediate state is labeled by a black dot in each panel.

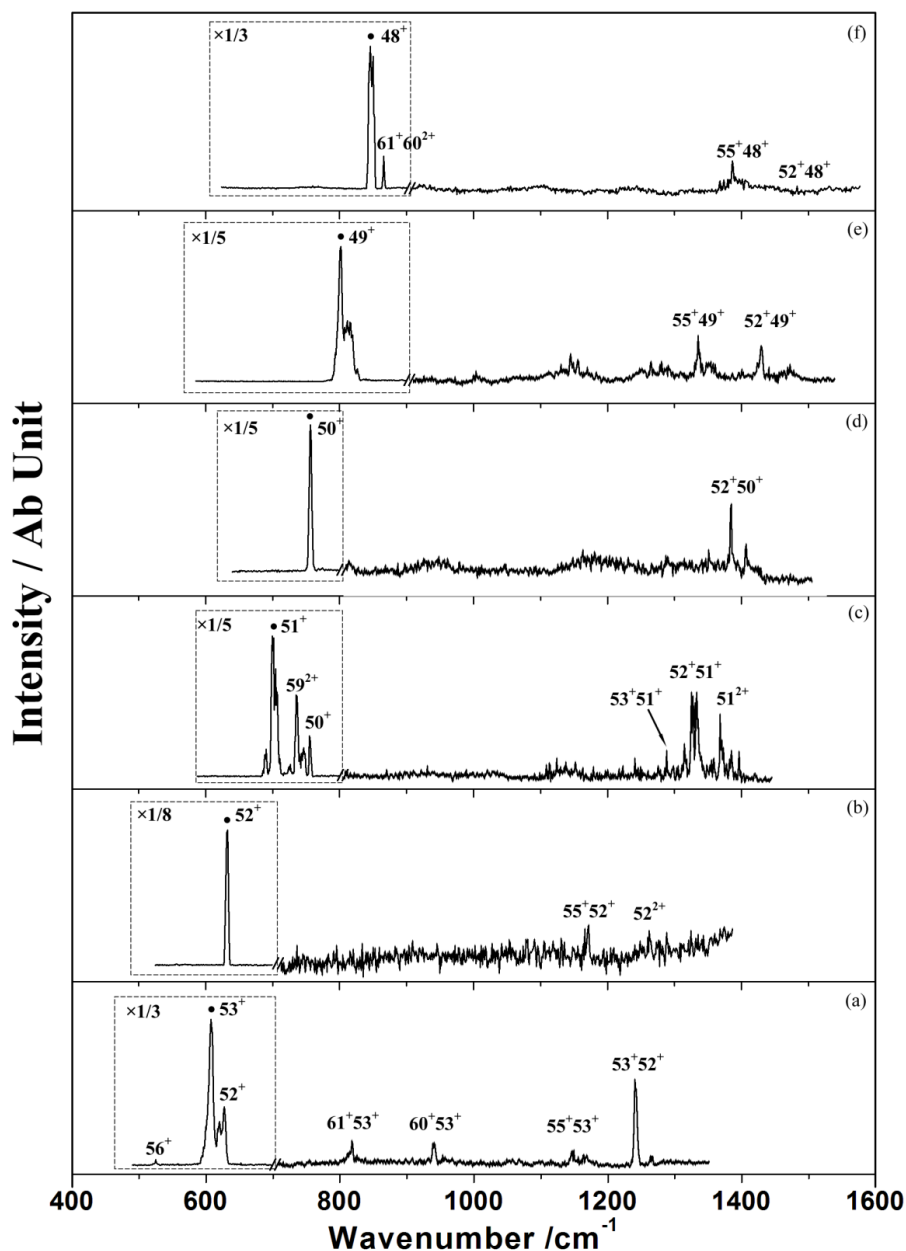


Figure 7.4 Two-color ZEKE spectra of BaP recorded via the following vibrational levels of the  $S_1$  state as intermediate states: (a)  $53^1$ , (b)  $52^1$ , (c)  $51^1$ , (d)  $50^1$ , (e)  $49^1$ , (f)  $48^1$ . The energy in the figure is relative to the ionization threshold at  $57271\text{ cm}^{-1}$ . The assignment in the figure refers to the vibrational levels of the cation, and the corresponding vibrational level of the intermediate state is labeled by a black dot in each panel.

Table II Observed and calculated vibrational frequencies of BaP cation

Intermediate level in the S <sub>1</sub> state												cal	Assignment
0 <sup>0</sup>	59 <sup>1</sup>	58 <sup>1</sup>	56 <sup>1</sup>	55 <sup>1</sup>	54 <sup>1</sup>	53 <sup>1</sup>	52 <sup>1</sup>	51 <sup>1</sup>	50 <sup>1</sup>	49 <sup>1</sup>	48 <sup>1</sup>		
0												0	0 <sup>0+</sup>
204												209	61 <sup>+</sup>
326												327	60 <sup>+</sup>
369												372	59 <sup>+</sup>
		451										449	58 <sup>+</sup>
		472										476	57 <sup>+</sup>
			522	523		524						508	56 <sup>+</sup>
532			532	535								523	55 <sup>+</sup>
				561	554							557	54 <sup>+</sup>
575												581	61 <sup>+</sup> 59 <sup>+</sup>
						607						608	53 <sup>+</sup>
627						628	633					632	52 <sup>+</sup>
650												654	60 <sup>2+</sup>
									699			695	51 <sup>+</sup>
722			729					724				717	61 <sup>+</sup> 56 <sup>+</sup>
				741				737				732	61 <sup>+</sup> 55 <sup>+</sup>
743								745				744	59 <sup>3+</sup>
								755	755			752	50 <sup>+</sup>
				803						803		808	49 <sup>+</sup>
						816						817	61 <sup>+</sup> 53 <sup>+</sup>
											846	852	48 <sup>+</sup>
			852									837	60 <sup>+</sup> 56 <sup>+</sup>
						867						852	60 <sup>+</sup> 55 <sup>+</sup>

		866	863	61 <sup>+</sup> 60 <sup>2+</sup>
897			895	59 <sup>+</sup> 55 <sup>+</sup>
	937		937	60 <sup>+</sup> 53 <sup>+</sup>
984			972	58 <sup>+</sup> 55 <sup>+</sup>
996			1004	59 <sup>+</sup> 52 <sup>+</sup>
1017			1006	58 <sup>+</sup> 54 <sup>+</sup>
1045			1053	58 <sup>+</sup> 53 <sup>+</sup>
1058			1031	56 <sup>+</sup> 55 <sup>+</sup>
	1070		1046	55 <sup>2+</sup>
1077			1081	58 <sup>+</sup> 52 <sup>+</sup>
	1146		1131	55 <sup>+</sup> 53 <sup>+</sup>
1151			1140	56 <sup>+</sup> 52 <sup>+</sup>
	1166	1169	1155	55 <sup>+</sup> 52 <sup>+</sup>
	1181		1189	54 <sup>+</sup> 52 <sup>+</sup>
	1239		1240	53 <sup>+</sup> 52 <sup>+</sup>
	1260		1264	52 <sup>2+</sup>
		1290	1303	53 <sup>+</sup> 51 <sup>+</sup>
		1329	1327	52 <sup>+</sup> 51 <sup>+</sup>
		1335	1331	55 <sup>+</sup> 49 <sup>+</sup>
		1370	1390	51 <sup>2+</sup>
		1383	1386	52 <sup>+</sup> 50 <sup>+</sup>
		1387	1375	55 <sup>+</sup> 48 <sup>+</sup>
		1430	1440	52 <sup>+</sup> 49 <sup>+</sup>
		1484	1484	52 <sup>+</sup> 48 <sup>+</sup>

transitions below  $1000\text{ cm}^{-1}$ , with the exception of a few transitions involving modes  $55^+$  and  $56^+$ . Higher frequency transitions are combination bands and overtones, which would naturally lead to larger deviations, particularly for combination bands with modes  $55^+$  and  $56^+$ . If we reset the frequencies of both modes  $55^+$  and  $56^+$  to be  $10\text{ cm}^{-1}$  higher, the agreement between calculation and experiment in Table 7.2 is within  $10\text{ cm}^{-1}$ . In addition, because of the large number of possibilities of combination at high energies, some of these assignments are tentative. In several cases, the choice was made to preserve the vibrational mode of the intermediate state, and the rationale for this choice is the propensity rule, which will be discussed in the following. Moreover, the resulting assignment has yielded a consistent presence of combination bands with modes  $55^+$  and  $52^+$  regardless of the initial vibrational excitation. This consistency may not be mere coincidence; rather it might hint at common structural adaptation upon electronic excitation. The displacement vectors of the observed modes are the same as those from REMPI, including the localized pyrene modes, the localized phenyl modes (ring I), and the overall skeletal modes.

The most striking feature of all the ZEKE spectra is the dominance of one vibrational band corresponding to the same vibrational excitation of the intermediate state. Unlike all the other PAH molecules we have studied<sup>17,18</sup>, a clear propensity of preserving the vibrational excitation of the intermediate state can be identified, with negligible vibrational relaxation or mode mixing. Based on our

previous study of substituted aromatic compounds,<sup>28-32</sup> this strong correlation between the intermediate level and the final vibrational level of the cation indicates negligible geometric changes upon ionization. This realization is the basis for the above choice in vibrational assignment of the much weaker bands in the high frequency region: when several combination bands are equally possible within the experimental uncertainty, the combination containing the original vibrational mode is chosen in Table 7.2.

Figure 7.3a was recorded via the origin of the  $S_1$  state, and the most intense peak corresponds to the origin of the cation. The adiabatic ionization potential is thus determined to be  $57271 \pm 5 \text{ cm}^{-1}$  ( $7.1006 \pm 0.0006 \text{ eV}$ ), taking into account the shift caused by the pulsed electric field. This value is  $20 \text{ cm}^{-1}$  lower than the ionization threshold extrapolated from the two color REMPI experiment by Gittins *et al.*<sup>25</sup> Other transitions with observable intensities in the ZEKE spectrum of Figure 7.3a correspond to excitations of  $a'$  modes  $61^+$ ,  $60^+$ ,  $58^+$ ,  $57^+$ ,  $55^+$  and  $52^+$ . Both the REMPI in Figure 7.2 and the ZEKE process in Figure 7.3a are governed by the Franck-Condon overlap, so if there are no major changes in the molecular frame upon electronic excitation and further ionization, these spectra should have similar vibronic activities. Although not quantitative, the overall intensity distribution of the two spectra does look similar.

All ZEKE spectra were obtained from in plane stretching modes, since the out of plane bending modes in the REMPI spectrum are too weak for further ZEKE

experiments. None of the in plane vibrational excitation of  $S_1$  has activated any observable out of plane bending modes. Instead, a few limited stretching modes seem to have universal presence in the form of combination bands, such as modes  $55^+$  and  $52^+$ , thus the resulting ZEKE spectra have a similar intensity distribution, with a cluster of transitions between 500 and 700  $\text{cm}^{-1}$  above the most intense transition. It is also interesting to notice that modes  $60^+$  and  $61^+$  are barely observable in the REMPI spectrum, but they can be clearly identified in the ZEKE spectra of Figure 7.3d and 7.4a. In addition, the missing mode  $57^+$  in the REMPI spectrum is activated by mode  $58^+$  in Figure 7.3c. Altogether, from modes  $61^+$  to  $48^+$ , the frequencies of the in plane stretching modes of the cation are spaced by 30 – 70  $\text{cm}^{-1}$ , a situation prone to mode coupling and to complications in frequency assignment.

## 7.5 Discussion

Similar to other peri-condensed PAHs we have studied<sup>16</sup>, BaP exhibits extensive configuration interactions, and in this situation, ab initio and DFT calculations typically fail to predict the correct order of the two excited states.<sup>34,35</sup> The gap between the two lowest excited states of BaP is less than 2000  $\text{cm}^{-1}$  and both states have the same symmetry  $^1A'$ . The first excited electronic state  $S_1$  with a relative small oscillator strength has a mixed electron transition of LUMO+1  $\leftarrow$

HOMO and LUMO ← HOMO-1, and the second excited state  $S_2$  with a larger oscillator strength is a LUMO ← HOMO transition.<sup>36</sup> This type of energy level inversion is also observed in pyrene and benzo[*g,h,i*]perylene.<sup>37-43</sup> Consequently, to obtain the correct geometry and vibrational frequencies from CIS calculation, we need to set the keyword “root = 2” in the input file. However, in comparing our results with those of Gittins *et al*, we discovered that there were substantial differences in both geometry and frequency. We then calculated the  $S_2$  state by setting root = 1 using the same CIS method, and reproduced the result of Gittins *et al* (all bond lengths in our results are shorter by about 0.003 Å - 0.004 Å due to the higher basis set used in our calculation). The authors also discussed that the Franck-Condon calculation based on their geometry was in poor agreement with the experiment. We therefore suspect that the assignment of Gittins *et al* for the vibronic transitions in the REMPI spectrum was probably affected by the wrong keyword.

Although BaP has one additional ring compared with pyrene, and the two systems have different symmetry, it is still insightful to compare the vibrational modes of the two systems. The extra ring on one side of pyrene degrades the  $D_{2h}$  symmetry of pyrene to  $C_s$  for BaP. At the first glance, one would expect that BaP should have more flexibility and less rigidity than pyrene, and hence it should have more activities involving the out-of-plane modes. In the REMPI spectrum of BaP, however, the out-of-plane butterfly waving motions are overshadowed by the a'

modes by orders of magnitude. This result is surprising since similar out of plane modes in pyrene are on par with the Franck-Condon allowed bands. In addition, only even quanta levels of the out-of-plane  $a''$  modes are observable in BaP, strictly obeying the FC principle, while the FC principle is not quite followed in pyrene. In fact, a similar FC calculation for pyrene is qualitatively different from the experimental spectrum, with deviations of orders of magnitude for the FC allowed and forbidden bands.

In some sense, the weak out of plane modes in BaP might be related to the symmetry of the nearby  $S_2$  state. Vibronic coupling with the  $A'$  state does not expand the selection rule to out of plane modes. In contrast, the  $S_2$  state of pyrene is  ${}^1B_{1u}$ , and vibronic coupling expands the selection rule to  $b_{3g}$  modes in addition to in plane modes. The presence of out of plane modes is thus caused by the symmetry of the electronic states, but the degree of vibronic coupling may not be reflected by the intensity of the out of plane modes or the degree of violation of the Franck-Condon principle. The latter statement is based on the fact that when the symmetry of the  $S_2$  state is identical to that of the  $S_1$  state, a similar Franck-Condon distribution is expected from both states, and mixing of the vibronic bands might not dramatically affect the intensity distribution.

We performed the Franck-Condon calculation to simulate the  $D_0 \leftarrow S_1$  transition from the origin of the  $S_1$  state, and the results are shown in Figure 7.5. We have purposely left out the origin band because of its dominating effect on

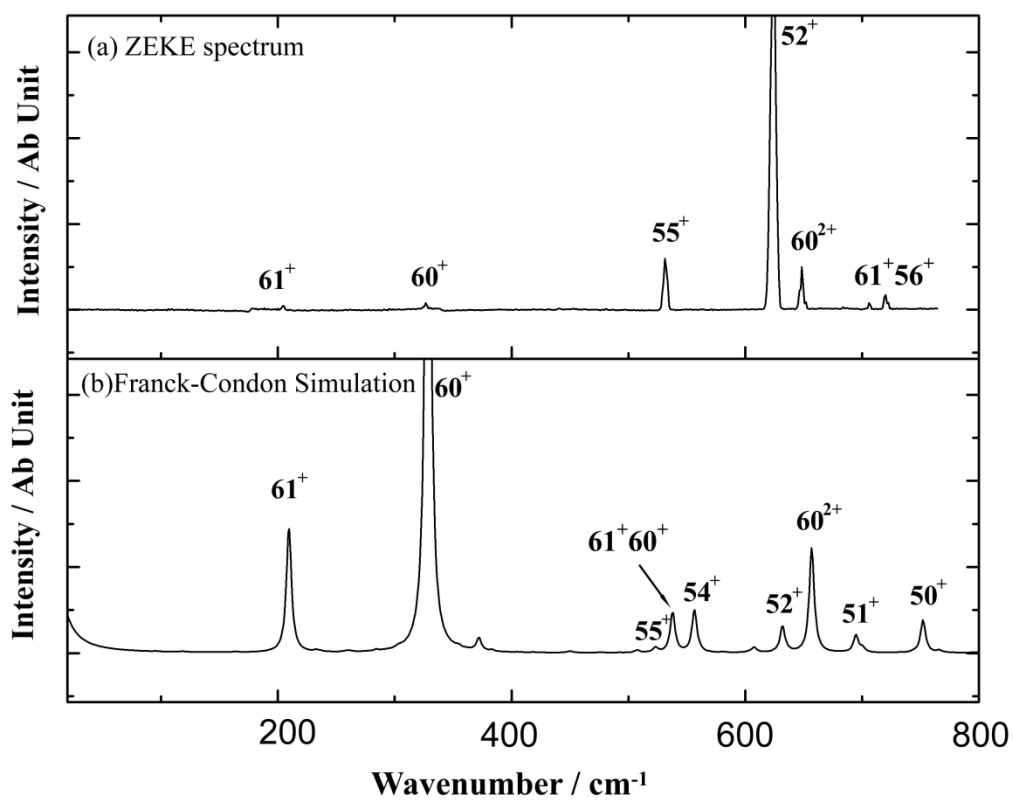


Figure 7.5 Comparison between the experiment ZEKE spectra with Franck-Condon simulation. (a) Experimental result. (b) Franck-Condon simulation.

other vibrational transition, and the wavenumber of x axis is shifted  $20\text{ cm}^{-1}$  to the blue side of the origin to emphasize the weaker transitions. Although the same modes are present in both panels, the agreement is not quite qualitative. Similar to the situation of REMPI, the intensity of mode  $60^+$  is greatly overestimated in the calculation, causing all transitions involving the overtone of or combination with mode  $60^+$  too intense in the simulation.

As we have discussed in the previous section, the strong propensity in ZEKE is an indicator of the similarity in geometry between the intermediate state and the cation ground state. With the aid from Gaussian, the geometries of the neutral ground state  $S_0$ , the first excited state  $S_1$  and cation ground state  $D_0$  can be calculated. In agreement with the experimental observations, the overall change in size is within 0.5% of the linear dimensions of the molecular frame upon excitation or ionization (8.6 Å between C3 and C12, and 4.3 Å between C6 and C12). This negligible geometry change of BaP is similar to that of benzo[*g,h,i*]perylene. However, for tetracene and pentacene, the width of the molecular frame increases by 1% upon electronic excitation and shrinks back to nearly the same size as that of the original neutral ground state upon ionization.<sup>17,18</sup> Although we have only a small set of samples, our studies of five PAHs seem to suggest that highly symmetric species are easily deformed upon excitation or ionization, while low symmetry species have more ability to absorb the positive charge upon ionization.

We have also calculated the Mulliken charge distribution for the  $S_0$  and  $D_0$  states, by including the charges on the peripheral hydrogen atoms in the adjacent rings and dividing the charges on the shared carbon atoms among conjoint rings. The results are listed in Table 7.3. In the ground neutral state, ring II donates almost half of an electron to ring I, while the rest of the three rings remain nearly neutral. After ionization, 2/3 of the extra charge on ring I is removed, while ring II is the most electron deficient, losing 56% of its charge. Based on our calculation, C8 is the most positively charged among all the carbon atoms connected with a hydrogen atom, and this is the most favorable position for substitution reactions, in agreement with observations in organic chemistry.

All  $a'$  modes are IR active, hence our results can directly assist with line identification in astrophysical surveys. Khan and Dwayyan studied the infrared spectrum of BaP cation doped in a wax film as well as in an argon matrix from 400  $\text{cm}^{-1}$  to 2000  $\text{cm}^{-1}$ .<sup>26</sup> Within our scanning range, the authors observed four  $a'$  modes: mode  $59^+$ ,  $55^+$ ,  $54^+$  and mode  $50^+$ . The frequencies in wax films are 5  $\text{cm}^{-1}$  higher than our values, but are still within our experimental uncertainty. Our work has further extended the experimental observation below 400  $\text{cm}^{-1}$ , mapped out fundamental transitions of more than ten IR allowed modes of the cation and some of their overtones. In addition, some of the observed modes are discovered to deviate from DFT calculations by over 10  $\text{cm}^{-1}$ , a situation that calls for precaution in relying exclusively on theoretical predictions.

Table 7.3 Charge distribution of BaP of  $S_0$  and  $D_0$  states.

Ring	I	II	III	IV	V
$S_0$	-0.425	0.458	-0.057	-0.046	0.068
$D_0$	-0.160	+0.559	+0.117	+0.207	+0.278

## 7.6 Conclusion

Spectroscopic properties of the electronically excited and ionic states of BaP have been studied using 1+1' two-color REMPI and two-color ZEKE. The observed vibronic transitions qualitatively agree with the Franck-Condon principle, dominated by in plane stretching and bending modes. This result is different from that of pyrene, a PAH with one fewer ring but a much higher symmetry point group. The lack of or weak out-of-plane waving modes in BaP is dictated by the symmetry of the interfering  $S_2$  state, which does not expand the vibrational selection rule to other modes. It is therefore difficult to gauge the rigidity of the molecular plane using the intensity of the out of plane modes. All the observed vibrational modes of the cation are IR active, and with the exception of two modes, the DFT calculation, after scaling by a factor of 0.9803, are in agreement with the experimental data. However, the necessity of the scaling factor and the inability to predict all modes with the same accuracy raise the issue of reliability of DFT calculations. In addition, the CIS calculation is incapable of predicting the energy order of the two interfering electronic states, and the need to include vibronic coupling explicitly in the frequency calculation is also exemplified in this study. The limit of our calculation methods further calls for laboratory experimental efforts, particularly in the context of astrophysical studies. In some favorable cases such as BaP, ZEKE offers direct information for astrophysical line identifications. In other cases

particularly with highly symmetry species, ZEKE spectroscopy offers frequency calibrations in the spectral region where other techniques are challenged.

### **7.7 Acknowledgement**

This work is supported by the National Aeronautics and Space Administration under award No. NNX09AC03G. Acknowledgment is made to the Donors of The Petroleum Research Fund, administered by the American Chemical Society, for partial support of this research.

## 7.8 Reference

- (1) Gillett, F. C.; Forrest, W. J.; Merrill, K. M. *Astrophys. J.*, **1973**, *183*, 87.
- (2) Allamandola, L. J.; Tielens, A. G. G. M.; Barker, J. R. *Astrophys. J.*, **1985**, *290*, L25.
- (3) Beintema, D. A.; van den Ancker, M. E.; Molster, F. J.; Waters, L. B. F. M.; Tielens, A. G. G. M.; Waelkens, C.; de Jong, T.; de Graauw, T.; Justtanont, K.; Yamamura, I.; Heras, A.; Lahuis, F.; Salama, A. *Astron. Astrophys.*, **1996**, *315*, L369.
- (4) L ger, A.; Puget, J., L. *Astron. Astrophys.*, **1984**, *137*, L5.
- (5) Moutou, C.; Leger, A.; D'Hendecourt, L. *Astron. Astrophys.*, **1996**, *310*, 297.
- (6) Smith, J. D. T.; Dale, D. A.; Armus, L.; Draine, B. T.; Hollenbach, D. J.; Roussel, H.; Helou, G.; Kennicutt, R. C.; Li, A.; Bendo, G. J.; Calzetti, D.; Engelbracht, C. W.; Gordon, K. D.; Jarrett, T. H.; Kewley, L.; Leitherer, C.; Malhotra, S.; Meyer, M. J.; Murphy, E. J.; Regan, M. W.; Rieke, G. H.; Rieke, M. J.; Thornley, M. D.; Walter, F.; Wolfire, M. G. *Astrophys. J. Supp. Ser.*, **2004**, *154*, 199.
- (7) Smith, J. D. T.; Draine, B. T.; Dale, D. A.; Moustakas, J.; Kennicutt, J. R. C.; Helou, G.; Armus, L.; Roussel, H.; Sheth, K.; Bendo, G. J.; Buckalew, B. A.; Calzetti, D.; Engelbracht, C. W.; Gordon, K. D.; Hollenbach, D. J.; Li, A.; Malhotra, S.; Murphy, E. J.; Walter, F. *Astrophys. J.*, **2007**, *656*, 770.
- (8) Tielens, A. G. G. M. *Annu. Rev. Astron. Astrophys.*, **2008**, *46*, 289.
- (9) Langhoff, S. R. *J. Chem. Phys.*, **1996**, *100*, 2819.
- (10) Sloan, G. C.; Hayward, T. L.; Allamandola, L. J.; Bregman, J. D.; DeVito, B.; Hudgins, D. M. *Astrophys. J.*, **1999**, *513*, L65.
- (11) Hudgins, D. M.; Bauschlicher, C. W.; Allamandola, L. J.; Fetzer, J. C. *J. Phys. Chem. A* **2000**, *104*, 3655.
- (12) Vala, M.; Szczepanski, J.; Pauzat, F.; Parisel, O.; Talbi, D.; Ellinger, Y. *J. Chem. Phys.*, **1994**, *98*, 9187.
- (13) Kim, H. S.; Wagner, D. R.; Saykally, R. J. *Phys. Rev. Lett.*, **2001**, *86*, 5691
- (14) Qi, F.; Yang, R.; Yang, B.; Huang, C.; Wei, L.; Wang, J.; Sheng, L.; Zhang, Y. *Rev. Sci. Instrum.*, **2006**, *77*, 084101.
- (15) Biennier, L.; Salama, F.; Gupta, M.; O'keefe, A. *Chem. Phys. Lett.*, **2004**, *387*, 287.
- (16) Zhang, J.; Han, F.; Kong, W. *J. phys. Chem. A*, **2010**. *submitted*
- (17) Zhang, J.; Han, F.; Li, A.; Kong, W. *Astrophys. J.*, **2010**, *715*, 485.
- (18) Zhang, J.; Pei, L.; Kong, W. *J. Chem. Phys.*, **2008**, *128*, 104301.
- (19) Li, A. PAHs in Comets: An Overview. In *Deep Impact as a World Observatory Event: Synergies in Space, Time, and Wavelength*; Kaufl, H.

- U., Siebenmorgen, R., Moorwood, A. F. M., Eds.; Springer: Berlin, 2009; pp 161.
- (20) Li, A.; Luning, J. I. *Astrophys. J.*, **2003**, *594*, 987.
- (21) Denissenko, M. F.; Pao, A.; Tang, M.-s.; Pfeifer, G. P. *Science*, **1996**, *274*, 430.
- (22) Kriek, E.; Rojas, M.; Alexandrov, K.; Bartsch, H. *Mutat. Res. Fundam. Mol. Mech. Mugag.*, **1998**, *400*, 215.
- (23) Smith, L. E.; Denissenko, M. F.; Bennett, W. P.; Li, H.; Amin, S.; Tang, M.-s.; Pfeifer, G. P. *J. Natl. Cancer Inst.*, **2000**, *92*, 803.
- (24) Greenblatt, G. D.; Nissani, E.; Zaroura, E.; Haas, Y. *J. Phys. Chem.*, **1987**, *91*, 570.
- (25) Gittins, C. M.; Rohlfing, E. A.; Rohlfing, C. M. *J. Chem. Phys.*, **1996**, *105*, 7323.
- (26) Khan, M. N.; Dwayyan, A. A. *Can. J. Pure Appl. Sci.*, **2009**, *3*, 833.
- (27) Gaussian 03, Revision E.01, Frisch, M. J., *et. al.* Gaussian, Inc., Wallingford CT, 2004.
- (28) He, Y.; Kong, W. *J. Chem. Phys.*, **2006**, *124*, 2043061.
- (29) He, Y.; Wu, C.; Kong, W. *J. Chem. Phys.*, **2004**, *121*, 8321.
- (30) He, Y.; Wu, C.; Kong, W. *Chem. Phys. Lett.*, **2004**, *391*, 38.
- (31) He, Y.; Wu, C.; Kong, W. *J. Chem. Phys.*, **2004**, *121*, 3533.
- (32) Wu, C.; He, Y.; Kong, W. *Chem. Phys. Lett.*, **2004**, *398*, 351.
- (33) Yang, D.-S.; Zgierski, M. Z.; Rayner, D. M.; Hackett, P. A.; Martinez, A.; Salahub, D. R.; Roy, P.-N.; Carrington, T. *J. Chem. Phys.*, **1995**, *103*, 5335
- (34) Goodpaster, J. V.; Harrison, J. F.; McGuffin, V. L. *J. Phys. Chem. A*, **1998**, *102*, 3372.
- (35) Parac, M.; Grimme, S. *Chem. Phys.*, **2003**, *292*, 11.
- (36) Birks, J. B. *Photophysics of Aromatic Molecules*; Wiley: New York, 1970.
- (37) Dierksen, M.; Grimme, S. *J. Chem. Phys.*, **2004**, *120*, 3544.
- (38) Grimme, S. *Chem. Phys. Lett.*, **1996**, *259*, 128.
- (39) Bito, Y.; Shida, N.; Toru, T. *Chem. Phys. Lett.*, **2000**, *328*, 310.
- (40) Tanaka, J. *Bull. Chem. Soc. Jpn.* **1965**, *38*, 86-102.
- (41) Borisevich, N. A.; Vodovatov, L. B.; D'yachenko, G. G.; Petukhov, V. A.; Semyonov, M. A. *J. Appl. Spec.*, **1995**, *62*, 482.
- (42) Aihara, J.-i.; Ohno, K.; Inokuchi, H. *Bull. Chem. Soc. Jpn.*, **1970**, *43*, 2435.
- (43) Tan, X.; Salama, F. *J. Chem. Phys.*, **2005**, *123*, 014312

## Chapter 8 Concluding Remarks and Future Work

### 8.1 Summary

This thesis presents our investigation on cation vibrational spectroscopy of a few selected PAHs using the REMPI and ZEKE techniques. The work of tetracene and pentacene further demonstrate that a laser desorption source can be combined with ZEKE spectroscopy for studies of thermally labile species. ZEKE spectroscopy provides information on the vibrational modes of the cation, and both the intensity distribution and frequency information are valuable for revealing the effect of charge on the molecular structure and for astrophysical modeling. Though governed by the Franck-Condon overlap and resulted in mainly to IR inactive modes in highly symmetric systems, ZEKE spectroscopy is also enriched by vibronic coupling between closely spaced excited electronic states. This mechanism further allows observation of some IR active modes, and for peri-condensed systems, the vibronic modes can even be stronger than the Franck-Condon allowed modes in the resulting ZEKE spectrum. While the frequencies of IR active modes particularly in the FIR are crucial to solving the mysterious carriers of the UIBs, both IR active and inactive modes are necessary for astrophysical modeling. With the frequencies from ZEKE, calibration of theoretical calculations with experiment becomes a reality, particularly for the FIR region of cations where typical experiments suffer from light source, detector, and particle concentrations.

Tetracene and pentacene are two largest members of the cata-condensed PAHs. Upon electronic excitation and ionization, both molecules maintain a nearly constant longitudinal dimension, but the width of the “ribbon” exhibit an increase of ~1%. Although they only differ by one phenyl ring, their ZEKE spectra demonstrate very different compositions. While tetracene shows rigidity with most of the active modes in both REMPI and ZEKE corresponding to in-plane stretching, pentacene has mostly out-of-plane waving modes. Vibronic coupling is considered an origin of these out of plane modes. The positive charge located on the center rings are higher than in the outer rings in tetracene and pentacene based on the DFT calculation result. This agrees with the Clar’s rule<sup>1</sup>, stating that the aromaticity of the polyacenes decrease from outer rings to inner rings and make the inner rings more reactive than the outer ones.

In the peri-condensed group, pyrene is the smallest among all three PAHs we have studied. Surprisingly, it is also the one that shows the largest number of out of plane modes in the REMPI and ZEKE spectra. In this sense, it seems to be the least rigid. In contrast, upon electronic excitation and further ionization, only in plane stretching or ring deformation modes are observed in the ZEKE spectra of benzo[g,h,i]perylene and benzo[a]pyrene. This contradiction between the size and rigidity is probably due to the symmetry of a nearby electronic state of the PAH molecule. The overall sizes of the peri-condensed PAHs remain constant during the transition of  $S_1 \leftarrow S_0$  and  $D_0 \leftarrow S_1$ . The molecular frame of peri-condensed PAHs

seems to have quite a capability to accommodate changes in electronic density, as demonstrated from the propensity in preserving the vibrational excitation of the intermediate state in ZEKE.

## 8.2 Future work

Systems listed in Figure 1.2 are considered astrophysical PAHs relevant to both modeling and detection of chemical compositions of the interstellar medium. In the meantime, these systems also represent expansions in both the isomeric forms and sizes of PAHs from the work reported in this thesis. For example, chrysene is an isomer of tetracene, with the same number of rings but cata-condensed diagonally. The kink in the molecular structure shortens the longitudinal dimension of the molecule and increases the transverse dimension. These changes should affect the rigidity and hence observed vibrational modes in REMPI and ZEKE spectroscopy. Furthermore, the symmetry of the system is lowered, and the selection rule in vibronic coupling should include more vibrational modes. Another candidate of interest is benzo[e]pyrene (BeP), an isomer of BaP. Instead of adding an extra ring along the long axis of pyrene, BeP has the ring along the short axis of pyrene. Therefore, BeP has  $C_{2v}$  symmetry higher than that of BaP ( $C_s$ ). By comparing different isomers with different symmetry point groups, insights on the molecular orbitals and vibrational normal modes can be obtained.

In addition, the spectral range of observation in REMPI can be extended to the  $S_2$  and higher states, further expanding the accessible modes in the ZEKE

experiment. This effort should be particularly rewarding for peri-condensed systems where two closely spaced electronically excited states are known to be extensively coupled.

In Herschel's First Results Symposium held in May, 2010, in addition to neutral water molecule, cationic water, in a new born star region, is reported as a first discovery in space: Herschel reveals that UV radiation from young stars ionizes the molecules of water to give  $\text{H}_2\text{O}^+$ . PAH cations are also considered possible intermediates in reaction(s) that form oxidized PAHs.<sup>2,3</sup> A potential next step is thus to study PAH-water complexes and find out possible effects of the attachment of water molecules on the photophysics and photochemistry of PAHs.

### 8.3 Reference

- (1) Clar, E. *Polycyclic hydrocarbons*; Academic Press: New York, 1964.
- (2) Bernstein, M. P.; Sandford, S. A.; Allamandola, L. J.; Gillette, J. S.; Clemett, S. J.; Zare, R. N. *Science*, **1999**, 283, 1135.
- (3) Bernstein, M. P.; Sandford, S. A.; Mattioda, A. L.; Allamandola, L. J. *Astrophys. J.*, **2007**, 664, 1264.